

CHARACTERIZATION AND OPTIMIZATION OF RADIATION AT NANO SCALE:
APPLICATIONS IN SOLAR CELL DESIGN

A Dissertation

by

MINE KAYA

Submitted to the Office of Graduate and Professional Studies of
Texas A&M University
in partial fulfillment of the requirements for the degree of

DOCTOR OF PHILOSOPHY

Chair of Committee,	Shima Hajimirza
Committee Members,	Michael Pate
	Douglas Allaire
	Hamid A. Toliyat
Head of Department,	Andreas A. Polycarpou

December 2020

Major Subject: Mechanical Engineering

Copyright 2020 Mine Kaya

ABSTRACT

High energy needs and environmental concerns associated with fossil fuels have raised the demand for efficient and clean alternatives of power generation. Solar cell technology is one of the most promising options of reliable renewable power sources despite high costs. Thin film solar cells offer the potential for reduction in the cost per kilowatt-hour due to the lower material usage. Nevertheless, most thin film solar cells suffer from low efficiency, though advancements in the science of near field radiation have led to substantial improvements in their optical efficiency. Many design challenges remain to be overcome for the wide-scale commercialization of thin film solar cells. In this dissertation, a numerical study is conducted for optical, optoelectrical and scattering performance enhancement of subwavelength optical devices (i.e., thin film solar cells and light trapping nanoparticles). The proposed design framework of thin film solar cells is based on learning based optimization and characterization methods, which utilize approximations of time consuming simulations. Additionally, a free form nanoparticle design procedure using evolutionary shape optimization is detailed.

The background of thin film solar cells and a comprehensive literature review of the thin film solar cell design approaches are provided in Chapters 2 and 3, respectively. The optical enhancement of thin film solar cells using nanoparticles with different shapes is studied in Chapter 4. In Chapter 5, an approximate formulation for optoelectrical efficiency of thin film solar cells is developed to accelerate the design optimization. The learning based design methodology that is introduced in Chapter 5 is further improved in

Chapter 6 using a knowledge transfer concept (also known as transfer learning). In this chapter, multiple sets of material combinations are optimized and compared with each other in terms of their optoelectrical efficiencies. In Chapter 7, nanoparticles are designed for maximum scattering, which is desired for enhanced optical performance, using a nonparametric evolutionary design method. In Chapter 8, a predictive model for scattering of arbitrarily shaped nanoparticles using descriptive geometric features is proposed.

Overall, this dissertation has led to significant contributions in the field of thin film solar cell design. The results show that the computational burden of the thin film solar cell design can be overcome significantly without sacrificing accuracy. Furthermore, the design methods developed for this dissertation can easily be transferred to other engineering areas involving repetitive, time consuming simulations for design optimization, such as other photonic design problems and integrated circuit design.

DEDICATION

To my parents, Hülya and Veli.

ACKNOWLEDGEMENTS

I would like to thank my research advisor, Dr. Shima Hajimirza for her advising and financial support during my PhD. I would also like to express my gratitude to Dr. Michael Pate, Dr. Douglas Allaire and Dr. Hamid A. Toliyat, for serving on my committee. I would also like to acknowledge Texas A&M High Performance Research Computing Center, where portions of the computational simulations were conducted.

I would like to thank all my past labmates, for their help and friendship. I also want to extend my thanks to all my friends in College Station, for making the last four years enjoyable. Special thanks to my friends, all in different parts of the world (Ankara, Los Angeles, Austin, to name a few), for being there for me whenever I need.

Last, but most importantly, I am genuinely grateful to my mom Hülya, my dad Veli, my sister Duygu, my brothers Ata and Mustafa, my uncle Fuat, and especially my nieces and nephews, Ege, Bade and Deniz, for their love, understanding and never-ending support. And I cannot thank Onur enough for *always* being by my side. It has been his patience and emotional support, which motivated me to break all the hardships.

CONTRIBUTORS AND FUNDING SOURCES

Contributors

This work was supervised by a dissertation committee consisting of Dr. Shima Hajimirza, Dr. Michael Pate and Dr. Douglas Allaire of the Department of Mechanical Engineering and Dr. Hamid A. Toliyat of the Department of Electrical and Computer Engineering. All work conducted for the dissertation was completed by the student, under the advisement of Dr. Shima Hajimirza.

Funding Sources

Graduate student was supported by the Graduate Research Assistantship from Dr. Shima Hajimirza and the Graduate Teaching Assistantship from the Department of Mechanical Engineering. This work was also supported in part by US National Science Foundation under grant CBET-1931966.

NOMENCLATURE

A	Area
c	speed of the light, convexity of a polygon
c_d	Directional convexity in the vicinity of d direction
C	Cost function, normalization constant
$C_{e,s,a}$	Extinction, scattering and absorption cross section
d	Diameter, size of the design domain
\mathcal{D}	Domain
$D_{n,p}$	Diffusivity of electron and hole
\mathbf{E}	Electric field
E_e	Sum of squared error
E_v	Sum of squared weights
E_g	Band gap energy
$F(x)$	Output of a surrogate model
$f_{NN}(x)$	Output of a neural network model
\mathbf{g}	Generation rate, gradient
G	The coordinates of polygon centroid
h	Planck's constant
\mathbf{H}	Magnetic field
H	Hessian
$I_{1.5AM}$	Standard terrestrial solar spectrum

J	Current density
J_{sc}	Short circuit current density
k	Imaginary part of the refractive index, wave vector
K	Number of transfer cases
k_B	Boltzmann constant
L	Number of NN layers
l_y	The ratio of the perimeter of the bounding rectangle located along x axis to the actual shape perimeter
L_D	Diffusion length
L_δ	Side length of a bounding box tilted with an angle δ
m_{pq}	(p, q) th central moment
n	Number of folds, sample size
N_{iter}	Number of iterations
N_k	Neighborhood of kth cell
N_p	Number of absorbed photons
n_d	Number of boundary points of a polygon
n_p	Spatial and spectral generation rate
N_v	Length of \mathbf{v} , number of vertices of a polygon
N_i	Number of incident photons
\mathbf{P}	Dipole moment
P	Poynting vector, periodicity, cartesian coordinates of a boundary point, perimeter

p	Normalized real part of Poynting vector
\mathbb{P}_c	Collection probability
$P_{e,s,a}$	Power extincted, scattered and absorbed
P_{in}	Power of incoming photons
P_{max}	Maximum power point of PV
p_n	Normalized perimeter
q	Elementary charge
$Q_{e,s,a}$	Extinction, scattering and absorption efficiency
\mathbf{r}	Recombination rate
r	Radius, Pearson correlation coefficient
R	Neighborhood size
R_i	Number of neurons in the i th layer of neural networks
R_i^k	Number of neurons in the i th layer of neural networks of the k th transfer case
s	Spacing
s_d	Directional sharpness in the vicinity of d direction
T	Absolute temperature
t	Thickness, computation time
V	Volume, the cartesian coordinates of a polygon vertex
\mathbf{v}	Vectorized form of Weight matrices
V_{oc}	Open circuit voltage
W_i	Weight matrix of the i th layer of a NN

w_k	Weight of the kth transfer case
\mathbf{x}	Solar cell geometry, optimization solution
x, y, z	Spatial location
\mathbf{x}^L	Lower bound of optimization
\mathbf{x}^U	Upper bound of optimization
\mathbf{x}_*	New data point for prediction
\mathbf{x}_b	Bare geometry
\mathbf{x}_p	Plasmonic geometry
\mathbf{x}_r	Random geometry
X_T	Inputs of training set for Gaussian process
\mathbf{x}_{TL}	Solution of transfer case
\mathbf{y}_*	Predicted output by GP
\mathbf{y}_0	The input vector of NN
\mathbf{y}_i	Output of ith layer of NN
y_T	Output of training set of GP
y_t	Target output

Greek Letters

α	Absorptivity, polarizability, line step, Bayesian regularization parameter
β	Bayesian regularization parameter
γ	The effective number of parameters, orientation angle
ε	Relative dielectric constant, error

ε_0	Permittivity of vacuum
ε_{im}	Imaginary part of the dielectric constant
ε_m	Dielectric function of host medium
η_A	Absorption efficiency
η_e	External quantum efficiency
η_I	Internal quantum efficiency
η_{pq}	(p, q) th scaled moment
κ	Exploration-exploitation tradeoff parameter
λ	Wavelength, eigenvalues of the Hessian matrix
μ	Mobility, mean
μ_0	Permeability of vacuum
$\mu_{n,p}$	Mobility of electron and holes
μ_r	Mean radius of a polygon
ν	Photon frequency
φ	Similarity function
ϕ_k	k^{th} moment invariant
$\phi_{e,1}, \phi_{e,4}$	1 st and 4 th order elongation
Ψ	Radial coordinates of a polygon vertex
ρ	Spearman correlation coefficient, density function
ρ_d	Directional perimeter in the vicinity of d direction
σ	Standard deviation
σ_x, σ_y	Symmetry around x and y axes

τ	Carrier lifetime
$\tau_{x,max}$	The ratio of the shape extends on the y axis to the maximum shape extend along any direction
θ	Incident angle
ξ	Shape factor
ξ_{α}	Coverage angle from an observer far from the shape
ξ_c	Compactness
ξ_e	Eccentricity
ξ_r	Rectangularity
ξ_v	The ratio of the visible vertices of a polygon from an observer to the total number of vertices

Abbreviations

ANN	Artificial neural networks
DSSC	Dye synthesized solar cells
EF	Optical enhancement factor
EIA	U.S. Energy Information Administration
EQE	External quantum efficiency
FDTD	Finite difference time domain
FF	Fill factor
GA	Genetic algorithm
GPBO	Gaussian Process Bayesian Optimization
IQE	Internal quantum efficiency

LCOE	Levelized cost of electricity
MSE	Mean squared error
NREL	National Renewable Energy Laboratory
OSC	Organic solar cell
PCE	Power conversion efficiency
PSC	Perovskite solar cells
PSO	Particle swarm optimization
QN	Quasi Newton algorithm
SA	Simulated annealing
SSE	Sum of squared error
TCO	Transparent conducting oxide
TL	Transfer learning
UCB	Upper confidence bound

TABLE OF CONTENTS

	Page
ABSTRACT	ii
DEDICATION	iv
ACKNOWLEDGEMENTS	v
CONTRIBUTORS AND FUNDING SOURCES.....	vi
NOMENCLATURE.....	vii
TABLE OF CONTENTS	xiv
LIST OF FIGURES.....	xviii
LIST OF TABLES	xxiii
1. INTRODUCTION.....	1
1.1. Current Status of Electricity Production	3
1.2. Thin Film Solar Cells	4
1.3. Motivation of the Dissertation.....	6
1.4. Objective of the Dissertation.....	7
1.5. Organization of the Dissertation	8
2. THIN FILM SOLAR CELLS	10
2.1. Classification of Solar Cells.....	10
2.2. Basics of Solar Cells and Performance Metrics	14
2.2.1. Absorption Efficiency	17
2.2.2. Recombination in Thin Film Solar Cells.....	19
2.2.3. External Quantum Efficiency	21
2.2.4. Power Conversion Efficiency.....	23
2.2.5. Other Performance Metrics	24
2.3. Light Trapping Techniques in Thin Film Solar Cells	25
2.4. Light Scattering by Nanoparticles.....	27
2.4.1. Effect of Particle Shape on Light Scattering	28
2.4.2. Theory of Light Scattering	30
2.4.3. Quasi Static Approximation	31

2.4.4. Mie Theory	32
2.5. Computational Methods for Optical Modeling of Thin Film Solar Cells	32
2.5.1. Finite Difference Time Domain Method	33
2.6. Conclusion.....	34
3. DESIGN OPTIMIZATION OF THIN FILM SOLAR CELLS USING NUMERICAL OPTIMIZATION	36
3.1. Optimization Problem	36
3.2. Exhaustive Search	38
3.2.1. Exhaustive Search Theory	38
3.2.2. Exhaustive Search in TFSC Design	38
3.3. Direct Search	40
3.3.1. Direct Search Theory.....	40
3.3.2. Direct Search in TFSC Design	40
3.4. Gradient Based Algorithms.....	41
3.4.1. Gradient Based Algorithms Theory	41
3.4.2. Gradient Based Algorithms in TFSC Design	42
3.5. Heuristic Algorithms	43
3.5.1. Heuristic Algorithms Theory.....	43
3.5.2. Heuristic Algorithms in TFSC Design	45
3.6. Learning Based Optimization Algorithms	48
3.6.1. Learning Based Optimization Theory	48
3.6.2. Learning Based algorithms in TFSC Design.....	55
3.7. Transfer Learning.....	57
3.8. Conclusion.....	58
4. OPTICAL ENHANCEMENT OF THIN FILM SOLAR CELLS	59
4.1. Thin Film Organic Solar Cells with Spherical Nanoparticles.....	61
4.1.1. Surrogate Model	62
4.1.2. Optimization Problem	63
4.1.3. Results and Discussion.....	64
4.1.4. Computational Cost.....	65
4.2. Thin Film Organic Solar Cells with Elliptical Nanoparticles and Interlayers	67
4.2.1. Surrogate Model	68
4.2.2. Optimization Problem	69
4.2.3. Results and Discussion.....	70
4.2.4. Computational Cost.....	75
4.3. Conclusion.....	76
5. DESIGN OPTIMIZATION OF THIN FILM SOLAR CELLS FOR MAXIMUM OPTOELECTRICAL EFFICIENCY	78
5.1. External Quantum Efficiency Formulation for Planar Thin Film Solar Cells	78

5.2. Schematic of the Planar Solar Cell.....	83
5.3. Optimization Problem	84
5.4. Surrogate Model.....	85
5.5. Results and Discussion.....	86
5.6. Computational Cost.....	89
5.7. Conclusion.....	89
6. TRANSFER OPTIMIZATION OF THIN FILM SOLAR CELLS FOR MAXIMUM OPTOLECTRIC EFFICIENCY	90
6.1. Multilayer Thin Film Solar Cell Optimization.....	91
6.2. Transfer Learning.....	93
6.3. Transfer Optimization of Thin Film Solar Cells Using Neural Networks	94
6.3.1. Methodology	94
6.3.2. Results and Discussion.....	97
6.4. Transfer Optimization of Thin Film Solar Cells Using Gaussian Process and Bayesian Optimization	104
6.4.1. Similarity Metric	104
6.4.2. Gaussian Quadrature Integration.....	105
6.4.3. Optimization Procedure.....	106
6.4.4. Results and Discussion.....	108
6.5. Conclusion.....	112
7. SHAPE OPTIMIZATION OF NANOPARTICLES FOR MAXIMUM SCATTERING	113
7.1. Physical Model Description	114
7.2. Optimization.....	117
7.3. Filtering	118
7.4. Results and Discussion.....	120
7.5. Conclusion.....	132
8. SHAPE DESCRIPTORS TO PREDICT SCATTERING BY NANOPARTICLES .	134
8.1. Methodology	135
8.2. Construction of Random Shapes	136
8.3. Predictive Geometric Features	137
8.3.1. Simple Features	139
8.3.2. Moment Based Features	142
8.3.3. Elongation Related Features.....	143
8.3.4. Orientation Related Features	145
8.3.5. Sharpness Related features	146
8.3.6. Convexity Related Features.....	146
8.3.7. Symmetry Related Features.....	148
8.4. Dataset.....	150

8.5. Results and Discussion.....	156
8.5.1. Training Results	156
8.5.2. Test Results	158
8.6. Conclusion.....	159
9. SUMMARY AND CONCLUSIONS.....	161
9.1. Summary of the Dissertations	161
9.2. Suggestions for Future Work	164
9.2.1. Experimental Verification of the Numerical Results	164
9.2.2. Optoelectrical Modeling and Optimization of Plasmonic Solar Cells	164
9.2.3. Scattering Prediction Using Geometric Features Based on Adaptive Sampling.....	165
REFERENCES	167
APPENDIX A SENSITIVITY ANALYSIS USING NEURAL NETWORKS	186
APPENDIX B OPTICAL PROPERTIES OF THE MATERIALS	191

LIST OF FIGURES

	Page
Figure 1.1. Historical and projected electricity generation by fuel. Left: all methods. Right: renewable methods. Taken from EIA [8].	4
Figure 2.1. Classification of solar cells based on technology and primary material. Inspired by [12].	11
Figure 2.2. Record solar cell efficiencies chart. Taken from NREL [10].	14
Figure 2.3. Fundamental physical events in a solar cell. (a) carrier generation upon photon absorption, (b) transfer of the carriers for the current generation.	15
Figure 2.4. Main loss mechanisms in a solar cell. (a) optical losses: reflection and transmission, (b) electrical losses: recombination of the carriers.	17
Figure 2.5. J-V (Current-voltage) characteristics of a solar cell.	23
Figure 2.6. Light trapping mechanisms in conventional (thick) cells by increasing the optical path length [50].	25
Figure 2.7. Light trapping mechanisms by plasmonics due to (a) multiple scattering, (b) localized surface plasmon resonances and (c) coupling of light to surface plasmon polaritons [53]. Adapted from [169].	26
Figure 2.8. Comparison of scattering cross sections obtained from FDTD simulations and Mie theory for a 50 nm silver sphere.	34
Figure 2.9. Yee cell and placement of electric and magnetic field vectors.	34
Figure 3.1. Classification of numerical optimization techniques.	37
Figure 3.2. Flowchart of genetic algorithm.	44
Figure 3.3. Flowchart of simulated annealing.	45
Figure 3.4. A two-layer NN architecture with multiple inputs and a single output. Adapted from [169].	51
Figure 3.5. Decision tree representation.	54
Figure 4.1. Comparison of the results of Finite Element Method (FEM) [99] and FDTD for a plasmonic OSC of $t_1 = 33$ nm, $t_2 = 20$ nm, $r = 5$ nm, $s =$ 11.5 nm with respect to periodicity P . Adapted from [169].	60

Figure 4.2. (a) 3D view of the OSC, (b) 2D Schematic of OSC with finite difference time domain (FDTD) solution domain. Adapted from [169].	62
Figure 4.3. Normalized mean sum of squared error (SSE) with respect to the number of neurons in the hidden layer (R_1). Adapted from [168].	63
Figure 4.4. Spectral absorptivity of plasmonic, bare and randomly designed solar cells with $\mathbf{x}_p = 24, 9, 6, 51, 89 T$, $\mathbf{x}_b = 24, 0, 0, 1, 89 T$ and $\mathbf{x}_r = 40, 11, 15, 80, 20T$.	66
Figure 4.5. Evolution of EF during iterations of SA, QN and hybrid SA–QN for the initial guess (a) $50, 20, 5, 100, 50T$; (b) $40, 11, 15, 80, 20T$. Adapted from [168].	66
Figure 4.6. OSC device with design parameters specified. Adapted from [170].	67
Figure 4.7. Mean sum of squared error (SSE) of training (top) and validation (bottom) sets with respect to the number of neurons in the hidden layer (R_1). Adapted from [170].	69
Figure 4.8. Maximized absorption Enhancement Factor as a result of NN based optimization. Adapted from [170].	71
Figure 4.9. Optimal values of design variables. Each point represents the result of a single optimization. Adapted from [170].	72
Figure 4.10. Evolution of enhancement factor during iterations of direct optimization. Adapted from [170].	74
Figure 4.11. Spectral absorptivity of plasmonic, bare and randomly designed solar cells with ($\mathbf{x}_p = 87, 37, 20, 28, 107, 15, 10, 25T$).	75
Figure 5.1. Variation of the collection probability in the absorber layer.	80
Figure 5.2. The variation of ηA and ηI with respect to the absorber layer thickness. The absorber is a-Si. Adapted from [171].	82
Figure 5.3. Comparison of measured and calculated EQE and simulated absorptivity profile for Ag/ZnO:Al/a-Si/ITO solar cell [60]. Adapted from [171].	83
Figure 5.4. Thin film multilayer solar cell structure. Adapted from [171].	84
Figure 5.5. Neural network training. (a) Normalized mean sum of squared error (SSE) with respect to number of neurons in hidden layer (R_1), (b) Evolution of SSE cost function during final NN training. Adapted from [171].	86

Figure 5.6. Evolution of surrogate EQE during optimizations with initial guesses (a) $\mathbf{x1}$, (b) $\mathbf{x2}$. Adapted from [171].	87
Figure 5.7. Absorptivity and EQE of initial $\mathbf{x1}$, $\mathbf{1}$ and optimized geometries in Table 5.2. Adapted from [171].	88
Figure 5.8. Absorptivity of optimized geometry obtained by NN and FDTD. Adapted from [171].	88
Figure 6.1. Multilayer solar cell.	92
Figure 6.2. Schematic of neural network with transfer learning for a single output. Adapted from [203].	95
Figure 6.3. (a) Variation of mean squared error for training and validation data sets with respect to the number of neurons in the hidden layer of NN for base case, (b) Evolution of EQE during optimization for the base case. Adapted from [203].	98
Figure 6.4. Results for (a) TL-1 (ITO-SiO ₂ -aSi-Al ₂ O ₃ -Al) and (b) TL-2 (Si ₃ N ₄ -PEDOT:PSS-PCPDTBT:PCBM-Al ₂ O ₃ -Al) without transfer layer (no TL, dashed lines) using 1000 data and with transfer layer (w/TL, solid lines) using 500 data. Adapted from [203].	100
Figure 6.5. Negative Transfer: Comparison of MSE of no TL Base case (dashed) and w/ TL from TL-1 (solid). Adapted from [203].	102
Figure 6.6. Evolution of EQE during optimization for (a) TL-1, w/out TL, (b) TL-1 w/ TL. Adapted from [203].	103
Figure 6.7. Evolution of EQE during optimization for (a) TL-2, w/out TL, (b) TL-2 w/ TL. Adapted from [203].	103
Figure 6.8. Comparison of the responses of the tasks given the same input set with the similarity metric (ϕ), pearson (r) and spearman (ρ) correlation coefficients. Adapted from [204].	109
Figure 6.9. Top: Absorptivity profiles of the 0th task (base) for optimized geometries using direct optimization and GPBO. Middle and Bottom: Absorptivity profiles of the 1st task (Middle), 2 nd task (Bottom) for optimized geometries using direct optimization and GPBO without (no TL) and with transfer learning (w/ TL). Adapted from [204].	110

Figure 6.10. Evolution of the EQE during optimization of (a) Task 0 without TL. (b) Task 1 without and with TL. (c) Task 2 without and with TL. Adapted from [204].	111
Figure 7.1. (a) Problem illustration and physical mechanisms involved, (b) schematic of a hypothetical geometry, monitor locations and the light source. $\rho_{\mathbf{x}}$ is the density function and Δd is the size of the discrete element, (c) three dimensional representation of the arbitrary geometry with computational mesh used in the study, (d) known shapes: sphere, cube, and prisms of hexagon and hexagram. The cubic domain with black edges is $d \times d \times d$, $d = 100\text{nm}$ in the present study.	115
Figure 7.2. The variation in the C_s values of the optimized shapes from P1 and P2 at $\lambda = 300\text{ nm}$ with respect to the (a) x and y meshes, (b) z mesh.	116
Figure 7.3. Optimized particle shape results from (a) P1, (b) P2. (black: solid, white: void).	121
Figure 7.4. Comparison of the objective function values of filtered optimum (method: open w/CB), unfiltered optimum and benchmark shapes. (a) P1, (b) P2.	124
Figure 7.5. C_s and C_a from the optimized geometries P1 compared with the profiles of benchmark shapes obtained from FDTD simulations.	126
Figure 7.6. C_s and C_a from the optimized geometries P2, compared with the profiles of benchmark shapes obtained from FDTD simulations.	126
Figure 7.7. (a) Filtered optimized geometry from P1. (b-d) Magnitudes of the electric field near the particle in part (a) at wavelengths (b) 500 nm, (c) 600 nm, (d) 700 nm.	128
Figure 7.8. (a) Filtered optimized geometry from P2. (b-d) Magnitudes of the electric field near the particle in part (a) at wavelengths (a) 500 nm, (b) 600 nm, (c) 700 nm.	128
Figure 7.9. Forward and backward C_s of the optimized (filtered) geometries (a) P1, (b) P2.	129
Figure 7.10. Locations of the circular monitors.	130
Figure 7.11. Angular variation of the real part of pointing vector on different principle axes with the wavelength.	132
Figure 8.1. Flowchart describing the proposed predictive modeling design pipeline.	135

Figure 8.2. Schematic of a polygon. Left: three dimensional polygon-prism with FDTD solution setup, right: definition of vertices, boundary points, and the centroid.	137
Figure 8.3. Bounding box representation.	141
Figure 8.4. Coverage angle from an observer far from the shape and the ratio of the visible vertices from an observer to the total number of vertices.	142
Figure 8.5. Histograms of different options for the target.	150
Figure 8.6. Scatter plots of target with each feature.	151
Figure 8.7. Analysis of the dataset using hierarchical clustering and absolute correlation matrix.	154
Figure 8.8. Comparison of the target and predicted outputs by (a) Regression Trees, (b) XGBoost Regression, (c) Neural Networks, (d) Linear Regression. Left: Training set, Right: Validation set.	157
Figure 8.9. Comparison of target and predicted data for the test set. (a) XGBoost, (b) neural networks regression.	158
Figure A.1. Variation of NN Output with respect to inputs using Profile Method	190

LIST OF TABLES

	Page
Table 1.1. Different methods used in TFSC design and examples from literature referred to in this dissertation.	7
Table 4.1. Optimized geometry of plasmonic OSC and corresponding enhancement factor (EF) values. Adapted from [168].	65
Table 4.2. Updated optimization bounds and optimization results. Adapted from [170].	74
Table 4.3. Computation times of corresponding operations. Adapted from [170].	76
Table 5.1. Upper (UB) and lower (LB) bounds for the multilayer solar cell. Adapted from [171].	85
Table 5.2. Results of optimization. Adapted from [171].	87
Table 6.1. Optimization results for Base, TL-1 and TL-2 cases. Adapted from [203]. .	102
Table 6.2. GP based numerical integration. Adapted from [204].	106
Table 6.3. Results of optimizations. Adapted from [204].	109
Table 7.1. Filtering methods used in the present study.	119
Table 7.2. Optimized objective functions in nm ² (equations (7.3) and (7.4)) compared to cube, sphere, hexagon, and hexagram prisms.	121
Table 7.3. Objective function values (equations (7.3) and (7.4)) of the original shape and the filtered shapes in nm ² using different methods. d: dilate, e: erode, c: close, o: open, df: density filtering with and without checkerboard control.	123
Table 7.4. Polar plots of the normalized real part of Poynting vectors from filtered optimized P1 and P2, sphere, and cube. Blue, red, and green lines show x-y, x-z, and y-z planes, respectively.	131
Table 8.1. Summary of the features with their description.	149
Table 8.2. Summary of the dataset. Mean, standard deviation, minimum and maximum values of the features and the target.	153
Table 8.3. Summary of the performances of fitting methods.	156

Table A.1. Percentage relative contribution of inputs using PaD and Garson's	
Methods	189

1. INTRODUCTION

The Sun is the source of all life on Earth. Every single mechanism on this planet owes its existence to the light emitted by the Sun. All the energy from the Sun reaches the Earth in the form of electromagnetic waves [1]. This is known as electromagnetic radiation, which is the most common long distance energy transport mechanism. In fact, the Sun is not the only source of electromagnetic radiation. Every object with a positive temperature (Kelvin) emits electromagnetic radiation. Humans may sense this radiation as heat or light, depending on its wavelength and intensity. Although radiation is negligible in some systems from an engineering perspective, its measurement and control are crucial for many other applications. For example, the only possible energy transport mode is radiation in space applications since a medium is not required for the propagation of electromagnetic waves. That is why satellites are designed to utilize thermal radiation for temperature regulation, which is powered by an array of solar panels. Industrial furnaces and internal combustion engines are other examples in which radiation should be accurately modeled. Furthermore, radiation is also crucial in several natural and human-made events, such as fires, material processing, laser-tissue interaction, biomedical devices, remote sensing, and so on.

One of the most important factors in electromagnetic radiation modeling is the size of the object interacting with the light. When the object is large compared to the wavelength of the light, the radiation problem can be solved through (semi)-analytical approximations, such as geometric optics and ray tracing [1]. When the dimensions of the

interacting object is comparable to or smaller than the wavelength of the light, these approximations fail to express the interaction mechanisms, and a more in-depth electromagnetics theory must be used. At atomic scales, there are also quantum physics effects that must be invoked and studied to render an accurate picture.

Radiation at small length scale objects falls in a category called *near field radiation* problems. Even though this phenomenon has been known for more than a century, the engineered realization of near field radiation in practical applications depends on recent progress in nanotechnology. Several applications of the near field radiation are listed below:

- Radiative cooling,
- Thin film solar cells,
- Near field thermophotovoltaics,
- Cancer therapy,
- Thermal control,
- Thermal imaging.

Despite the increase in the studies conducted on these subjects in recent years, there are still many challenges to be addressed. For instance, the overly complex relationship between the radiative properties and the physical properties, such as size, geometry and material, requires detailed modeling to understand near field radiation. Additionally, realizing small scale devices necessitates precise and inexpensive fabrication techniques. Addressing these challenges will make the widespread commercialization of the devices utilizing near field radiation more feasible.

Solar cell technology is a prominent application of electromagnetic radiation due to the ever-increasing sustainable energy demand and efforts to decrease carbon emissions. The status quo in global electricity production and thin film solar cells is discussed in the next two sections of this chapter. Afterwards, the motivation, objective and the organization of the dissertation are laid out in Sections 1.3, 1.4, and 1.5, respectively.

1.1. Current Status of Electricity Production

The energy demand per capita and the world population have both been increasing at an unprecedented rate due to industrialization since the 1800s. Among different sources, fossil fuels (e.g., coal, oil and natural gas) are the primary means of energy production despite their environmental harms. Fossil fuels are non-renewable energy sources and the largest source of greenhouse gas emission [2,3]. Nevertheless, their maturity and low cost make them popular in electricity production [4]. The use of fossil fuels in electricity production can be decreased if efficient and cheap renewable technologies are developed. Energy research has focused on developing new systems and improving the existing alternative technologies in terms of cost, efficiency, and lifetime. Wind, solar (photovoltaics and solar thermal), geothermal and hydropower are examples of renewable energy sources that can be used as alternatives to fossil fuels for a carbon-free economy in the future.

The fraction of electricity produced by photovoltaics (PV) in total electricity production has been increasing since the advent of the first commercial silicon based solar cells. It is predicted that PV will be the leading renewable energy source due to the

availability of its power source (Sun), decrease in price and improvement in efficiency [5–7]. The chart of electricity generation in the United States by fuel type is presented in Figure 1.1, which is taken from the U.S. Energy Information Administration (EIA) [8]. As of 2019, the share of all renewables in the electricity generation is less than 20% and 3% of all electricity is generated by solar systems. Solar power is expected to be the leading renewable energy source by 2050, with a 17% share in all electricity generation. These expectations unequivocally rely on the efforts of solar researchers around the world. Thanks to the continued research on solar power, the anticipated market increase can even exceed the expectations.

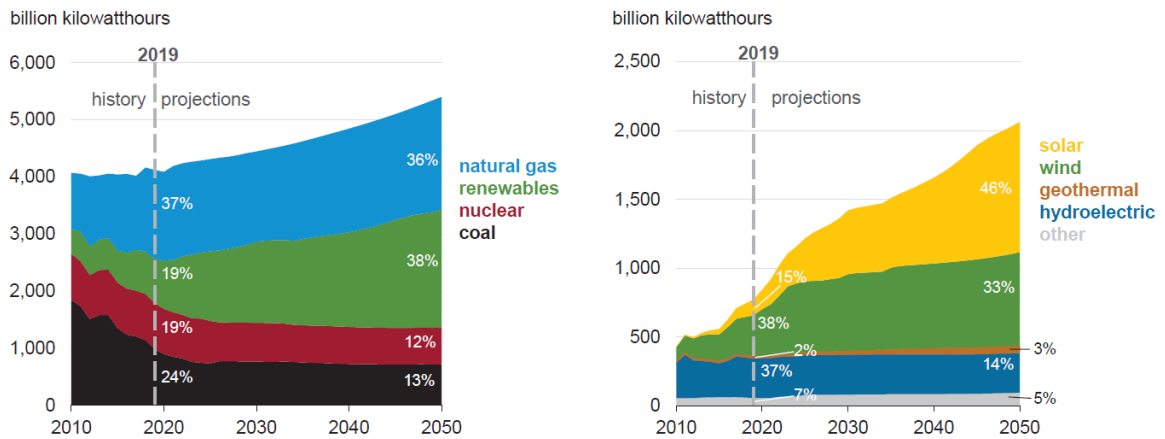


Figure 1.1. Historical and projected electricity generation by fuel. Left: all methods. Right: renewable methods. Adapted from [8].

1.2. Thin Film Solar Cells

The history of solar cells begins with the discovery of the photovoltaic effect in the early 1900s. The first reported silicon solar cell did not emerge until 1941 and had an

efficiency of less than 1% [9]. The efficiency increased rapidly and reached 15% with phosphorus and boron doping in the 1970s. As of 2018, the efficiency of crystalline silicon solar cells exceeded 25% [10]. Along with the development of silicon solar cells, crystalline gallium arsenide has also been demonstrated as an efficient type of solar cell with a record efficiency of 27.8%. Despite the excellent efficiencies of crystalline solar cells, they suffer from high fabrication costs. On the other hand, thin film solar cells (TFSCs) are strong rivals to conventional solar cells due to their lower material and fabrication costs and light-weight [11]. TFSCs can provide unique optical properties because the photon absorption at near field strongly depends on the thin film geometry.

A thin film is a material layer smaller than or comparable to the observable light wavelength, which is created by random growth and nucleation processes of molecular species on a substrate. The physical and chemical properties of such materials depend on the deposition parameters and the film thickness [7]. Together, these parameters provide tunable properties for various applications. For solar cell applications, thin film solar cells are attractive because low material costs per-watt of energy conversion can be achieved. Other attractive features of TFSCs are the tailorable radiative properties for unique applications (e.g., flexible or colored solar cells for windows, curved surfaces) due to the diversity in the choice of shapes, sizes and substrates [7,12]. However, TFSCs suffer from low average efficiencies compared to conventional solar cells, and this issue needs to be addressed for wide-scale commercialization.

TFSCs require a rigorous design procedure in order to reach high efficiencies with low cost and high stability. The strong yet complicated dependence of TFSCs'

performance on the structural and material design necessitates careful optimization routines to reach the desired objectives. However, the design process of TFSC is not straightforward due to the lack of proper and comprehensive modeling tools. The existing tools are also generally computationally intense. More details on the physical background and design approaches to TFSC and supplementary structures will be given in the remainder of this thesis in Chapters 2 and 3.

1.3. Motivation of the Dissertation

The design of TFSCs and light trapping structures has been a subject of research since the invention of solar cells. The early design of these structures mostly relied on purely experimental approaches. The improvements in the computational resources have made computational modeling techniques feasible to be used in TFSC design and optimization. The most common approaches to the TFSC design, as well as examples from the literature, are summarized in Table 1.1. The details of these methods and the discussion of examples can be found in Chapter 3.

Learning based methods have also been used in TFSC design, but they are not as common as the methods summarized in Table 1.1. Recent studies have applied learning based techniques in material design [165], [166]. The use of machine learning methods in TFSC design problems is a relatively new concept where most of the examples have been proposed in the last few years [166], [172], [173]. Nevertheless, these methods have been demonstrated to be useful by the researchers in the field of optical devices [174]–[182]. Although these studies do not directly target photovoltaic devices, they provide evidence for the potential of learning based methods in TFSC design problems.

Table 1.1. Different methods used in TFSC design and examples from literature referred to in this dissertation.

Method	References
Exhaustive search	[73], [89] – [101]
Direct search	[64], [103] – [105]
Gradient methods	[108] – [113]
Heuristic methods	[119] – [143]

Overall, an improved design optimization framework can accelerate the commercialization of inexpensive and high efficiency thin film solar cells. Despite the substantial literature on the numerical optimization of solar cells, the potential of learning based and evolutionary methods have not been thoroughly assessed. This dissertation investigates the usage of learning based techniques and evolutionary methods to achieve a time-efficient and highly accurate design. This dissertation also studies the effects of structural and geometric properties of thin film solar cells and light trapping particles on their radiative responses.

1.4. Objective of the Dissertation

The main objective of this dissertation is to propose time efficient and accurate approaches for modeling, design and optimization of thin film solar cells and subwavelength structures for higher light-to-electricity conversion efficiencies. In this dissertation, the following technical questions are addressed:

- 1) How to reduce the computational cost of the conventional optimization methods used in TFSC design?
- 2) What is the effect of nanoparticle shape on the optical efficiency of TFSC?

- 3) How to approximate the optoelectrical efficiency of TFSC so optimization can be done faster?
- 4) How to incorporate the knowledge from previous design problems into the current design?
- 5) How to design free form (nonparametric) shapes?
- 6) How to characterize the radiative properties of nanoparticles based on their shapes?

1.5. Organization of the Dissertation

The rest of the dissertation is organized as follows: In Chapter 2, the background of solar energy harvesting, specifically thin film solar cells and light trapping mechanisms, are explained. Chapter 3 provides a detailed review of design and optimization approaches in TFSC design with the mathematical background of related algorithms. Chapter 4 details a data driven optimization procedure for two case studies of absorption enhancement in thin film organic solar cells. In the first case (Section 4.1), the geometrical features of a three-layer cell with spherical nanoparticles are optimized. In the second case (Section 4.2), a five-layer cell with elliptical nanoparticles is optimized for maximum absorption enhancement. In Chapter 5, an approximate optoelectrical efficiency metric is proposed and validated with the experiments in the literature. This metric is used as the objective function in the geometrical optimization of a five-layer planar cell. Chapter 6 is devoted to improving the design procedure in Chapter 5 by introducing the knowledge transfer concept. In Chapter 7, a nonparametric light trapping design approach based on topology optimization is used for the maximum light scattering, which is the underlying mechanism

of light trapping. Chapter 8 details a data driven characterization methodology for the radiative properties of nanoparticles based on their geometric features. Conclusions and suggestions for future work are outlined in Chapter 9.

The question 1 in Section 1.4 is addressed in Chapters 4, 5 and 6. Chapter 4 also aims to answer the question 2. In Chapter 5, the question 3 is addressed. Chapter 6 aims to answer question 4. Chapter 7 addresses the question 5. Finally, Chapter 8 addresses the question 6.

2. THIN FILM SOLAR CELLS

This chapter is devoted to the theory, applications, and modeling guidelines of the thin film solar cells. First, the different categories of solar cells from conventional to emerging types are reviewed. And a brief overview of the current state of the solar cell research is presented. In Section 2.2, the performance metrics of solar cells are presented. Next, the subwavelength light trapping methods for absorption enhancement are reviewed and underlying physical mechanisms are discussed. In Section 2.5, the optical modeling of TFSC is explained with an emphasis on computational methods. Finally, the chapter is summarized and the relevance of solar cell metrics to the present study is discussed in the last section.

2.1. Classification of Solar Cells

The solar cells are mainly categorized according to the device structure and absorber material. Device structure refers to wafer based and thin film technologies where the same material can be used in a different solar cell type, such as silicon. Although thin film solar cells have been studied along with conventional solar cells, novel and somewhat unusual materials have also been utilized as the absorber layer in TFSCs, particularly in emerging types. This trend has accelerated smart material composition techniques, e.g. based on machine learning. This classification is presented in Figure 2.1.

		MATERIAL		
		Silicon	Semiconductor compounds	Novel materials
TECHNOLOGY	Wafer-based	<ul style="list-style-type: none"> • Single crystal • Multi crystal 	<ul style="list-style-type: none"> • Gallium Indium Phosphorus • Gallium Arsenide 	
	Thin film	<ul style="list-style-type: none"> • Crystal • Hydrogenerated amorphous silicon (a-Si:H) 	<ul style="list-style-type: none"> • Cadmium Telluride (CdTe) • Copper Zinc Tin Sulphide (CZTS) • Copper Indium Gallium Selenide (CIGS) 	<ul style="list-style-type: none"> • Dye Sensitized • Perovskite • Organic • Quantum Dot

Figure 2.1. Classification of solar cells based on technology and primary material [12].

The earliest examples of thin film solar cells were proposed as early as the 1950s and became a potential alternative to conventional silicon solar cells over the years. Amorphous silicon (a-Si) solar cells provide low manufacturing costs compared to silicon but suffer from low efficiency. CdTe, CIGS and CZTS offer relatively high efficiencies (~23%), while there are several drawbacks to be addressed before commercializing, such as toxicity of cadmium and rarity of telluride (i.e., high material cost).

The novel, or emerging, materials have been a subject of semiconductor research in the last decades in order to find a reliable and efficient alternative to silicon. One of the most attractive features of these novel materials is that they provide tunable physical properties because of nanostructured characteristics. The solar cells with novel materials (i.e. dye sensitized, perovskite, organic, quantum dot) have only been suggested in thin

film format due to the advantages of thin film technology. The main disadvantage of these materials is the immaturity of their technology and the low efficiency compared to conventional solar cells. On the other hand, given the research and development efforts, their efficiency is expected to increase rapidly in the next decades.

One of the earliest examples of the emerging solar cells is the dye-sensitized solar cell (DSSC) [13,14]. In general, DSSC comprises a semiconductor film, a sensitizer adsorbed onto the semiconductor surface, an electrode stacked between a transparent conductive oxide (TCO) and a cathode [14]. DSSC is fundamentally different from the solid state solar cell devices in terms of carrier transfer because of using liquid electrodes [12]. DSSC provides the advantage of low cost, compatibility with printing methods and flexibility, whereas their long-term stability, low absorptivity, high recombination rates are the challenges to be addressed.

Perovskite solar cells (PSC) were first considered to be a capable sensitizer of a DSSC [15,16] until it was realized that perovskite is sufficient itself to absorb light and generate carriers [17]. Perovskite is a material with a general formula of ABX_3 where A is the organic or inorganic monovalent cation, B is the bivalent cation and X is the halide atom. The most common molecule used in photovoltaic applications is organic metal halides methylammonium lead iodide ($CH_3NH_3PbI_3$) [18]. There are also attempts to develop lead-free perovskite solar cells, using tin (Sn) and bismuth (Bi) based molecules to eliminate potential harm due to lead. The power conversion efficiency of PSC has increased from ~15% in 2013 to ~25% in 2020 [10] and is expected to reach theoretical limits with further optical and electrical enhancements [19–21]. Furthermore, PSCs offer

more straightforward processing than silicon solar cells, and have lower cost than quantum dot solar cells. Nevertheless, long-term stability and toxicity due to lead are the issues to be solved before commercialization.

Another class of emerging solar cells is organic solar cells (OSC). Research on organic solar cells (OSC) has a three decade history, with the first mature examples studied and presented in the 1990s [22,23]. Interest in these devices has led to a record energy conversion efficiency of 17% as of 2020 [10], exceeding that of DSSC (12%). Although the power conversion efficiency of OSCs is lower than their inorganic counterparts, they provide low cost, ease of manufacturing, mechanical flexibility and environmental friendliness [24,25]. Organic molecules are known to have high spectral (radiative) absorptivity; however, their narrow absorption band results in poor carrier generation rate. The formal definition of generation rate is provided in Chapter 5. Bulk heterojunction (BHJ) OSC devices, which consist of a blend of the donor and acceptor components, provide improved optical-electrical conversion efficiency compared to the bilayer devices consisting of a stack of p- and n-type semiconductors by providing a large interfacial area between donor and acceptor [26]. The blend mostly consists of a conjugated polymer donor and a fullerene derivative acceptor. P3HT:PCBM is one of the most commonly used blends in the active layer of the solar cell due to commercial availability and guaranteed stability [27].

The widely accepted chart for record efficiencies by National Renewable Energy Laboratory (NREL) is presented in Figure 2.2.

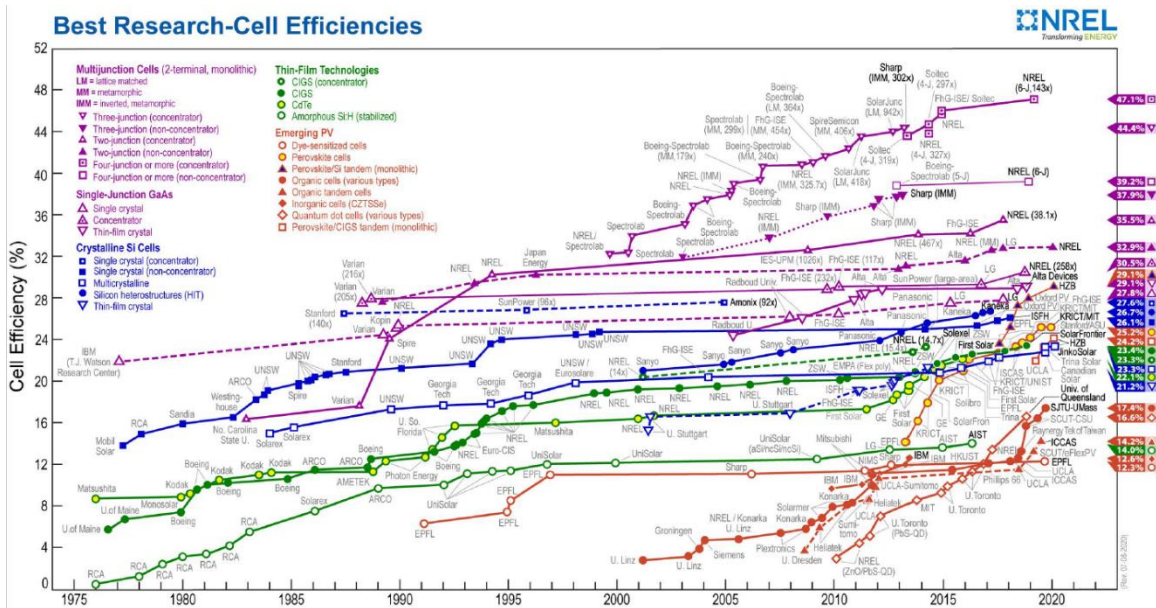


Figure 2.2. Record solar cell efficiencies chart. Adapted from [10].

2.2. Basics of Solar Cells and Performance Metrics

A solar cell is a device that converts the energy of photons to the electricity by the photovoltaic effect. The following steps must occur sequentially for a solar cell to work:

1. Absorption of photons in a suitable material,
2. Creation of charge carriers by breaking bonds between atoms,
3. Separation of oppositely charged free carriers (electron-hole pair),
4. Collection of photo-generated charge carriers through electrical contacts and their passage through an external circuit to create an electric current.

A photon with energy higher than the bandgap (E_g) of the semiconductor can be absorbed.

Once absorbed, the photon can excite an electron and creates a positive charge, i.e., hole.

Then the electron and hole start moving to the opposite directions based on drift and

diffusion mechanisms. The electrons move toward the n-type semiconductor, and the holes move toward the p-type semiconductor. These movements create an electrical potential difference, so they make charge unneutrally. However, if the electron does not travel fast enough, the recombination of electron and hole can occur. If the electrodes of the cells are connected to an external circuit, electricity will be generated. The fundamental mechanisms in this process are illustrated in Figure 2.3.

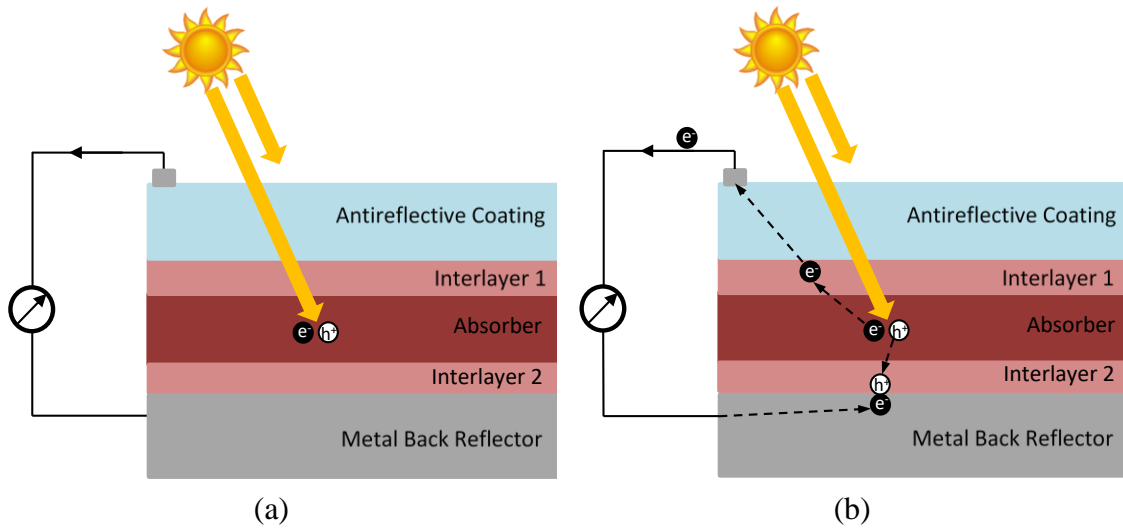


Figure 2.3. Fundamental physical events in a solar cell. (a) carrier generation upon photon absorption, (b) transfer of the carriers for the current generation.

In general, a solar cell consists of a semiconductor absorber, an antireflective coating and a back-metal contact. It is also quite common to use electron and hole transport layers (ETL and HTL) as interlayers for better carrier transport as well as refractive index smoothing [28,29]. Common materials for the antireflective coating are indium tin oxide

(ITO), silicon nitride (Si_3N_4), fluorine doped tin oxide (FTO), silicon carbide (SiC) and silicon dioxide (SiO_2). Metals, such as silver (Ag), gold (Au) and aluminum (Al), are used as the back contact due to their high conductivity and reflectivity. The most common choices for ETL and HTL layers are metal oxides, such as titanium dioxide (TiO_2), zinc oxide (ZnO), molybdenum trioxide (MoO_3), organic compounds, such as Spiro-OMeTAD, PEDOT:PSS.

The absorber is the main component of a solar cell where the photovoltaic effect occurs. Ideally, the absorber material of an efficient solar cell should be a *direct bandgap semiconductor* with a bandgap of ($\sim 1.5\text{eV}$) with a high solar optical absorption ($\sim 10^5/\text{cm}$), high quantum efficiency of excited carriers, long diffusion length, low recombination velocity, and should be able to form an excellent electronic junction with suitably compatible materials [7]. The solar cell classification in Figure 2.1 is proposed based on the absorber materials.

Solar cell performance is highly related to the material properties, environment conditions (temperature, incoming light) and loss mechanisms in the solar cell. Losses take place at various steps during electricity generation. For example, the incoming photons might be reflected or transmitted through the solar cell, which are the optical losses associated with the solar cells. Furthermore, the absorbed photon may not create an electron hole pair, or the created electron hole pairs can recombine before the electron reaches the electric circuit. These loss mechanisms are summarized in Figure 2.4. The solar cell performance related to these losses is explained in the next sections.

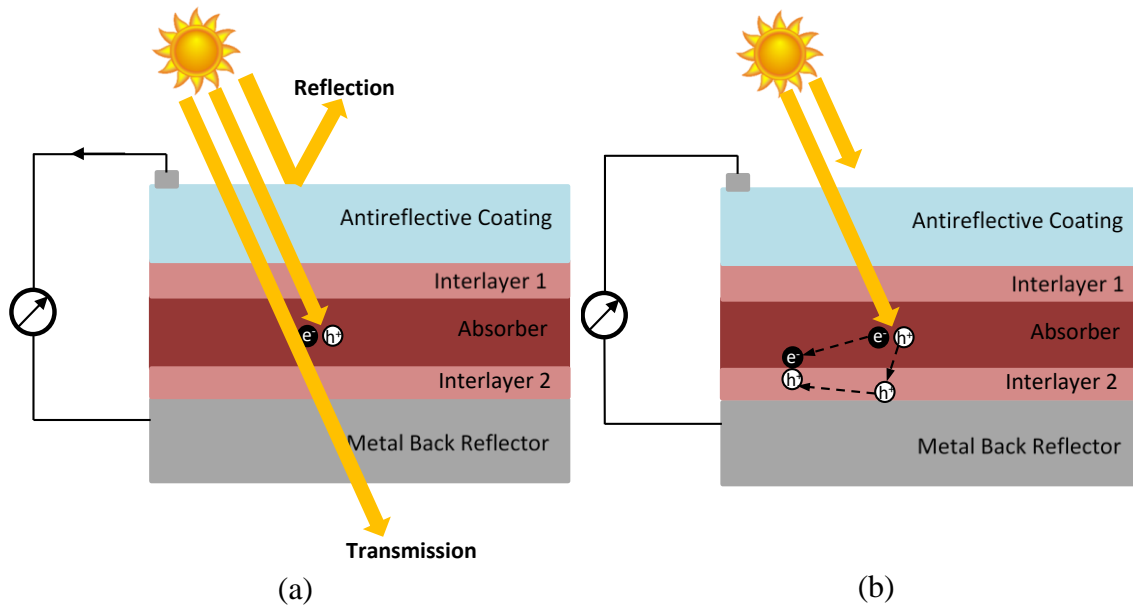


Figure 2.4. Main loss mechanisms in a solar cell. (a) optical losses: reflection and transmission, (b) electrical losses: recombination of the carriers.

2.2.1. Absorption Efficiency

Light travels as an electromagnetic wave in the vacuum, with a phase velocity, known as the speed of light ($c_0 = 299,792,458$ m/s). The quantum of an electromagnetic wave is called a photon, which can be described as an *energy packet*. A photon has no rest mass yet has photon energy of $h\nu$, where h is Planck's constant and ν is photon frequency. The interaction of a photon with the matter has been one of the most widely studied research areas in the last century due to many different applications, such as solar cells, light emitting diodes and optical communication.

Light absorption is modeled by the electromagnetic theory. However, the modeling can be simplified under some circumstances. For example, when the dimensions of the structure are significantly larger than the operating wavelength, geometric optics

assumptions hold, and *ray tracing* formulations can be utilized. However, when the dimensions of the structures are comparable to or smaller than the wavelength, Maxwell's electromagnetic equations explain the dynamics more accurately. Maxwell's electromagnetic equations are a set of partial differential equations which comprise four individual laws of Gauss, Gauss magnetism, Faraday and Ampere [30]. Together, they explain the dynamics of electromagnetic wave propagation. These equations govern the behavior of electric and magnetic fields under various effects, such as electrical current or external electric field. In the case of solar cells, they explain the radiative (optical) behavior. Specifically, Faraday's and Ampere's laws are solved for nonmagnetic materials:

$$\begin{aligned}\frac{\partial \mathbf{E}}{\partial t} &= \frac{1}{\varepsilon_0 \varepsilon} \nabla \times \mathbf{H}, \\ \frac{\partial \mathbf{H}}{\partial t} &= -\frac{1}{\mu_0} \nabla \times \mathbf{E},\end{aligned}\tag{2.1}$$

where \mathbf{H} and \mathbf{E} are the magnetic and electric fields, respectively, ε is the relative dielectric constant, ε_0 is the permittivity of vacuum and μ_0 is the permeability of vacuum.

The spectral absorptivity of a solar cell, which is the amount of power absorbed under unit illumination, is calculated from the electric field within the solution domain:

$$\alpha(\mathbf{x}) = \int_V -\frac{\pi}{\lambda} |\mathbf{E}|^2 \varepsilon_{im}(\lambda) dV,\tag{2.2}$$

where ε_{im} is the imaginary part of the dielectric constant, λ is wavelength and V is the volume of the absorber. The number of photons absorbed in a solar cell is an essential optical performance metric which is calculated as a function of the absorptivity as follows:

$$N_p(\mathbf{x}) = hc \int_{-\infty}^{\infty} \lambda \alpha(\mathbf{x}, \lambda) I(\lambda) d\lambda, \quad (2.3)$$

where h is the Planck's constant, c is the speed of light, $\alpha(\mathbf{x}, \lambda)$ is the spectral absorptivity and $I(\lambda)$ is the standard *terrestrial irradiance spectrum*. \mathbf{x} is the solar cell geometry. The above integration is done over wavelengths shorter than bandgap wavelength, $\lambda < hc/E_G$. Then the absorption efficiency can be defined as the ratio of the number of absorbed photons to the number of photons incident on the solar cell:

$$\eta_A = \frac{N_p}{N_i} = \frac{\frac{1}{hc} \int \lambda \alpha(x, \lambda) I(\lambda) d\lambda}{\frac{1}{hc} \int \lambda I(\lambda) d\lambda}. \quad (2.4)$$

2.2.2. Recombination in Thin Film Solar Cells

When an absorbed photon creates an electron-hole pair inside a semiconductor, a non-equilibrium state is obtained. Recombination occurs when the electron excited to the conduction band relaxes back to its thermal equilibrium to the valence band without completing the external circuit for electricity generation. Recombination is one of the main loss mechanisms in solar cells [31]. Recombination can occur inside the semiconductor, which is called bulk recombination, or at the surface or interfaces of the semiconductor, which is called surface recombination. There are three different types of bulk recombination: *radiative*, *non-radiative* and *trap-assisted* recombination. In radiative (or band-to-band) recombination, an electron from the conduction band combines with a hole in the valence band and emits a photon at band-gap energy. This is the primary recombination mechanism in the direct band-gap semiconductors, such as GaAs, but often negligible in the indirect semiconductors. Non-radiative recombination, a.k.a Auger

recombination, is very similar to radiative recombination, but instead of emitting the energy, an electron in the conduction band receives the energy. Auger recombination is significant in doped regions. Trap-assisted recombination, which is also called Shockley-Read-Hall (SRH) recombination, is the dominant recombination mechanism in the indirect band-gap semiconductors. SRH recombination occurs mostly due to defect levels in a semiconductor. High recombination rates are observed at the surface and interfaces of solar cells since defects are mainly found at the interfaces (surface recombination). Special techniques, such as passivation, can eliminate surface recombination.

Transport of charges from the absorber to the junctions is governed by drift diffusion equations [32–34]:

$$\begin{aligned}\mathbf{J}_n &= q\mu_n n\mathbf{E} + qD_n \nabla n, \\ \mathbf{J}_p &= q\mu_p p\mathbf{E} + qD_p \nabla p,\end{aligned}\tag{2.5}$$

where n and p are densities of electron and hole, respectively. $\mathbf{J}_{n,p}$ is the current density in A/m², $\mu_{n,p}$ is the mobility and $D_{n,p}$ is the individual diffusivities of n and p , respectively. q is the elementary charge. Solving drift-diffusion equations requires Poisson's equation (electrostatic potential) and current continuity equations:

$$\begin{aligned}-\nabla \cdot (-\varepsilon\mathbf{E}) &= q(p - n), \\ \nabla \cdot \mathbf{J}_n &= q(\mathbf{g} - \mathbf{r}), \\ \nabla \cdot \mathbf{J}_p &= -q(\mathbf{g} - \mathbf{r}),\end{aligned}\tag{2.6}$$

where \mathbf{g} and \mathbf{r} are the carrier generation and recombination rates, respectively. The recombination rate is estimated using different recombination mechanisms, mentioned previously. Drift diffusion equations are generally solved using computational methods. The generated carrier due to absorption in the absorber layer can only travel a distance, i.e., diffusion length, which depends on the diffusion coefficient and carrier lifetime:

$$L_D = \sqrt{D\tau}, \quad (2.7)$$

where D ($\mu k_B T/q$) is the diffusivity, μ is the mobility, k_B is the Boltzmann constant, T is the absolute temperature and τ is the carrier lifetime, which is defined as the average time a carrier travels before recombination. L_D is the length that a carrier can travel before recombination. Thus, the design of a solar cell should consider L_D as a design parameter. Although absorption increases with the thickness of the solar cell, charge collection no longer increases due to recombination. Therefore, recombination limits photocurrent and *short circuit current*, even if the absorption efficiency is high. Although electrical modeling through drift diffusion modeling provides exact performance information, approximate electrical modeling affixed to the optical modeling can advise overall performance.

2.2.3. External Quantum Efficiency

An efficient solar cell must provide desirable optical and electrical properties for overall performance. One of the performance metrics quantifying joint optical and electrical efficiency is the *external quantum efficiency* (EQE). EQE is defined as the ratio

of the number of generated electrons (N_e) to the number of incident photons on the solar cell (N_i):

$$\eta_e = \frac{N_e}{N_i} = \frac{N_p}{N_i} \frac{N_e}{N_p} = \eta_A \eta_I, \quad (2.8)$$

where η_A is the absorption efficiency from equation (2.4). η_I is called the *internal quantum efficiency* (IQE), which measures the electron generation from the absorbed photons. IQE and EQE are mostly measured experimentally in order to calculate short circuit current density [35]. There are numerous examples of experimental measurements of IQE and EQE for solar cells. For example, Thouti et al.[36] measured IQE of a textured silicon solar cell to estimate the effective diffusion length due to the resonance effect of silver nanoparticles. There have also been attempts at obtaining analytical expressions for the quantity. Ferrero et al. [37] proposed a method to calculate EQE of photodiodes based on Beer's law for absorption and Shockley–Read–Hall recombination. The structure is divided into front, space-charge (depletion), and rear regions and treated differently regarding recombination. Dibb et al. [38] approximated the collection model as a step function, which is unity in the depletion region and zero elsewhere. In these two theoretical models, the exact knowledge of the dimensions of the depletion zone and p and n layers are required. In [39,40], Xue et al. developed a probabilistic EQE model preserving the dependence of charge collection probability to the absorber thickness and diffusion length, but without knowledge of the depletion zone.

2.2.4. Power Conversion Efficiency

The ultimate solar cell efficiency is calculated by the power conversion efficiency (PCE). The historical efficiency development presented in Figure 2.2 is given in terms of PCE, defined as follows:

$$PCE = \frac{P_{max}}{P_{in}} = \frac{FF \times J_{sc} \times V_{oc}}{P_{in}}, \quad (2.9)$$

where P_{max} is the maximum power point which corresponds to the maximum (Current \times Voltage) value (indicated with mp in Figure 2.5) and P_{in} is the power of incoming photons. J_{sc} is the short circuit current density, V_{oc} is the open-circuit voltage. Fill factor, FF , is the ratio of the maximum power to the theoretical maximum ($P_{max}/J_{sc}V_{oc}$). FF can be visualized as the ratio of areas of the inner rectangle to the outer rectangle in Figure 2.5.

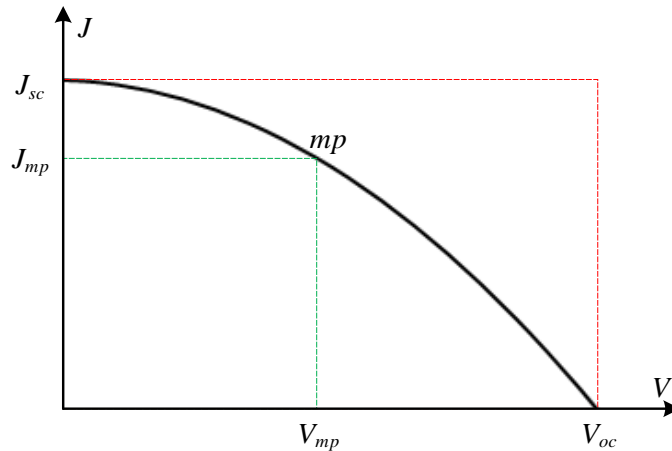


Figure 2.5. J-V (Current-voltage) characteristics of a solar cell.

The optical and electrical losses explained in the previous sections play an essential role in these parameters. Optical performance directly affects J_{sc} . Furthermore, recombination has been shown to affect V_{oc} [41–43] and FF [44–46] in equation, thus it limits the overall solar cell efficiency.

2.2.5. Other Performance Metrics

In addition to the mentioned metrics in this section, other parameters can be used to quantify solar cell performance. Some of these metrics are listed below with a brief explanation:

- *Levelized cost of electricity* (LCOE) quantifies the effects of the investment expenditures, annual total cost, operating costs, operational lifetime compared to the electricity production in its lifetime.
- *Energy yield* compares the solar cell performance in its actual location compared to the standard test conditions, i.e., at an irradiance of $1,000 \text{ W/m}^2$ and a module temperature of 25°C .
- *Reliability and stability* of a solar cell are related to the degradation containing corrosion, delamination, breakage, cracking cells, and so on. These phenomena are caused by environmental factors such as temperature, humidity, irradiation, mechanical shock. Possible figures of merit under this category are T_{80} (20% PCE decay from initial PCE) and η_{1000} (PCE after 1000 h) [47]

2.3. Light Trapping Techniques in Thin Film Solar Cells

Light trapping is the general term used to describe mechanisms that manipulate the light to focus at a particular location. In solar cells, this mechanism is used to enhance the optical thickness of the absorber while keeping physical thickness unchanged. Despite the differences in the carrier generation and transfer in TFSC, they all require light trapping structures due to their poor absorption coefficients, especially near the band edge [48]. The earliest methods for light trapping aimed to increase the optical path length of the light by a flat or textured back reflector, periodic [49], and random surface gratings (Figure 2.6).

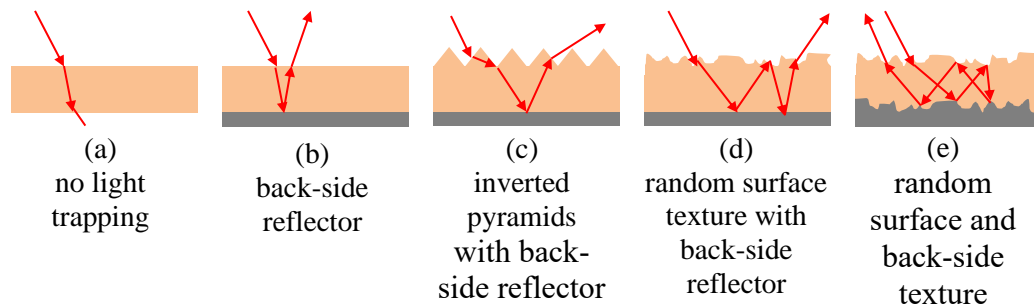


Figure 2.6. Light trapping mechanisms in conventional (thick) cells by increasing the optical path length [50].

In addition to the conventional methods such as using a back reflector and antireflecting coating, light trapping in TFSCs can be achieved by tailoring the optical properties of the materials utilizing light-material interaction. For example, textured back reflectors can be used, thus converting them into a diffraction grating (see Figure 2.7c). The diffraction gratings couple reflected light in the absorber [51,52], thus significantly increase the absorption of long wavelength photons.

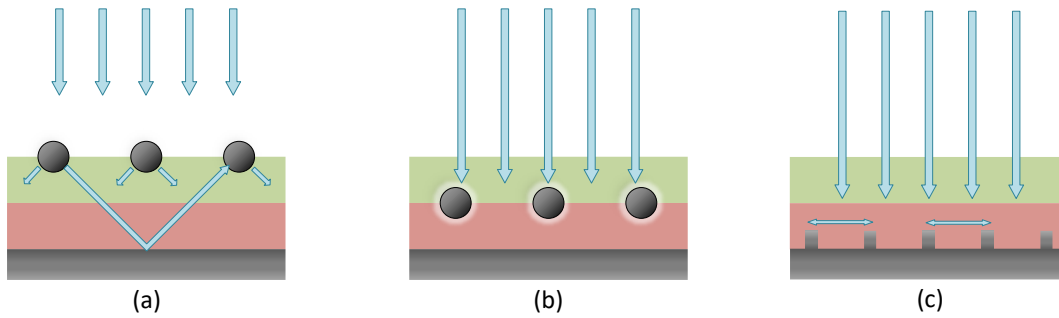


Figure 2.7. Light trapping mechanisms by plasmonics due to (a) multiple scattering, (b) localized surface plasmon resonances and (c) coupling of light to surface plasmon polaritons [53]. Adapted from [169].

Another technique for light trapping is the utilization of plasmonic effects in the solar cell. Plasmonics is an emerging area in material research which deals with the interaction of free electrons of metal with the electromagnetic waves. Plasmonic structures offer a unique physical mechanism to increase the optical thickness of the light absorbing media. For example, surface plasmons can be used for forward scattering, as shown in Figure 2.7a. When a small metal particle is placed close to the interface of two dielectrics, the light will more likely scatter into the material with larger permittivity. This phenomenon enables light to pass through the semiconductor several times if there is also a metal back reflector, thus enhances the optical thickness of the solar cell. Another mechanism to utilize plasmonic effects is that metallic nanoparticles embedded in semiconductors behave like an antenna where near field effects enhance the light absorption (Figure 2.7b). However, generated carriers can be accumulated near metallic particles; therefore, these particles are mostly coated with dielectric layers for avoiding recombination.

The interaction of light with metal surface results in a phenomenon called *local surface plasmon resonance*, which is the source of the optical enhancement. The metal nanoparticles create a strong near field enhancement mediated with the resonance scattering. When designed carefully, this scattering can be much larger than the absorption inside the nanoparticles, which contribute significantly to the solar cell performance. Furthermore, as the dielectric coating of the nanoparticles prevents the contact of metal and semiconductor, we can safely assume that metal nanoparticles do not cause additional recombination.

2.4. Light Scattering by Nanoparticles

The unique optical properties of small particles have been a subject of extensive research since the late 19th century. If utilized and engineered properly, these properties can lead to the design of materials with desirable optical wideband or narrowband responses. In 1871, a study by Lord Rayleigh established a relationship between the scattering cross section of particles with size much smaller than the wavelength and light frequency and particle polarization [54]. Later, Gustav Mie provided a rigorous solution for optical scattering by spherical homogeneous particles of arbitrary size and material properties in a homogeneous medium on the basis of Maxwell's electromagnetic theory [1,55,56]. Following those preliminary studies, the continuing interest in light scattering in the last century has provided guidelines for many engineering design applications based on theoretical studies and appropriate numerical and computational methods. These applications include cellular imaging [57], cancer therapy [58], optical antennas [54], light emitting diodes [59] in addition to the TFSCs [60].

Proper light scattering can lead to an important phenomenon called light trapping [61], which is absorption enhancement in a medium without increasing the physical thickness of the absorber. Recently, surface texturing [62], diffraction grating [63], and random nanoparticles [64] have been demonstrated to facilitate light trapping in thin absorbers. Light scattering using nano scale designs has especially gained attention vis-à-vis plasmonic effects. The science of plasmonics deals with the interaction of free electrons of metal with the electromagnetic waves yielding charge oscillations [65]. The local electric field is strengthened due to the oscillations known as localized surface plasmons when excited by the incident light at a particular resonance frequency [66]. The plasmonic enhancement also translates to higher scattering, which is a function of the electric field.

2.4.1. Effect of Particle Shape on Light Scattering

The optical response of isolated nanoparticles to radiation is a highly complex function of the physical properties such as particle size, shape and material, as well as the characteristics of incident light (e.g., wavelength, polarization, angle, etc.). The radiative response profile can be characterized by multiple metrics, including the response strength, bandgap, stop band, bandwidth, resonance/peak frequency, number, location and range of peaks, etc. These characteristics are intertwined and adjustable via the choice of geometry and material. The tunability of the radiative spectrum makes the geometry design an attractive method for unique devices that utilize nanoparticles [67–69]. In some simplified cases, e.g., when the particle size is significantly smaller than the wavelength, the *quasi static* assumption holds, and the impact of the particle shape can be approximated via various shape factors [54,70,71]. For larger sized particles, Mie theory provides an

analytical solution to Maxwell's equations. However, the solution obtained thereby is limited to spherical shapes [56], with a few limited extensions for nonspherical shapes [72,73].

Nonspherical shapes are more polarizable along specific directions compared to a sphere, and light coupling strength and resonance frequencies vary for different particle shapes [70,74]. In the literature, there are various studies concerning the dependence of the radiative spectrum of common nonspherical shapes, such as triangles, cylinders, spheroids, and cuboids [75–80] as well as more exotic forms such as bipyramids [81], star and flower shapes [82], bowl and dumbbell shapes [83]. In [80], the optical spectra of different geometries, such as spheres, cubes, tetrahedra, and pyramids, were studied and distinct characteristics in the scattering and absorption responses due to the shape and size effects were characterized. In [79], it was shown that scattering spectra of cuboid shapes with rounded corners depend on the amount of rounding and can be manipulated by geometric changes. In [74], the peak absorption of a nanoparticle was found to be increasing with a higher number of sharp edges of the particle. Yet, one should note that a desired optical performance is not guaranteed with this indicator since the peak wavelength and the bandwidth are also important contributing factors. In another study focusing on the shape related variations in the optical spectra, Lombardi *et al.* [81] demonstrated that the electric field is localized around the sharp edges of the elongated nanostructures. In all these studies, the effect of the geometry on the optical properties was emphasized through known shapes, such as spheroids and polyhedrons. Nevertheless, the

possibilities are not limited to the basic shapes, and further improvements in the optical properties can be realizable by undiscovered geometries through rigorous design.

2.4.2. Theory of Light Scattering

The energy loss during the light-material interaction is called extinction and occurs due to absorption and scattering:

$$P_e = P_s + P_a, \quad (2.10)$$

where P_e , P_s and P_a are the power extincted, scattered and absorbed, respectively. Dividing P_e , P_s and P_a by the irradiance, I_o , extinction (C_e), scattering (C_s) and absorption (C_a) cross sections are obtained:

$$C_e = C_s + C_a. \quad (2.11)$$

These cross sections are not necessarily the physical cross sections, but rather wavelength dependent metrics that can be much larger than the physical values. This enhancement is sometimes quantified by the efficiency term defined as the ratio of the optical cross sections in equation (2.11) to the physical cross section:

$$Q_j = \frac{C_j}{A_p}, \quad (2.12)$$

where j is the index for extinction, scattering or absorption. Light material interaction is explained by the electromagnetic theory and Maxwell's equations. Under certain circumstances, the solution can be greatly simplified and explicit, e.g., when the particle size is significantly smaller than the light wavelength, thus electrostatic approximations hold. Further assumptions for an explicit solution usually involve symmetry in particle shapes, e.g., Mie's theory provides analytical solutions for sphere-like particles. The

optical cross sections can be calculated by solving Maxwell's equations using different methods. These methods are explained next, along with the underlying physical assumptions.

2.4.3. Quasi Static Approximation

When the particle size is much smaller than the wavelength of the light, electrostatic approximations hold. This phenomenon is also known as Rayleigh scattering. In such cases, the induced dipole moment is expressed as the particle polarizability times the imposed electric field, $\mathbf{P} = \alpha\mathbf{E}$ where particle polarizability is expressed as follows:

$$\alpha = (1 + \xi)\varepsilon_0 V \frac{\varepsilon - \varepsilon_m}{\varepsilon + \xi\varepsilon_m}, \quad (2.13)$$

where V is the particle volume and $\varepsilon_0, \varepsilon_m$ and ε are dielectric functions of vacuum, host medium and particle, respectively. ξ is the shape factor which represents the dependence of the polarizability to the particle shape. For sphere, $\xi = 2$ and equation (2.13) reduces to the Clausius-Mossotti relation [42]. The extinction and scattering cross sections are calculated from:

$$C_e = k \operatorname{Im}(\alpha), \quad (2.14)$$

$$C_s = \frac{k^4}{6\pi} |\alpha|^2, \quad (2.15)$$

where $k = 2\pi\sqrt{\varepsilon_0}/\lambda$ is the wave vector and $\operatorname{Im}(\cdot)$ and $|\cdot|$ give the imaginary part and norm of a complex number, respectively.

Despite the infinitesimal particle assumption, there are several approaches to correct the quasi-static approximation for particles of larger size, such as Modified Long

Wavelength Approximation, where the contributions of radiative damping and depolarization are also considered [84]. Although the quasi-static approximation does not hold as the scattering regime moves out of Rayleigh and particle shape deviates from a sphere, it provides insight on the effects of the particle shape, volume and surrounding medium on optical properties of particles.

2.4.4. Mie Theory

Gustav Mie obtained the analytical solution for optical scattering by spherical homogeneous particles with arbitrary size and material properties in a homogeneous medium based on Maxwell's equations [1,55,56]. Specifically, the cross sections can be estimated as a series form:

$$C_e = \frac{2\pi}{k^2} \sum_{n=1}^{\infty} (2n + 1) \text{Re}(a_n + b_n), \quad (2.16)$$

$$C_s = \frac{2\pi}{k^2} \sum_{n=1}^{\infty} (2n + 1) (|a_n|^2 + |b_n|^2), \quad (2.17)$$

where a_n and b_n are Mie coefficients [1,55,56]. Mie theorem was originally established for spheres. However, the solution was later adapted to nonspherical shapes such as ellipsoids and a few corner case generalizations. More complex shapes can be analyzed using computational methods such as the finite difference time domain (FDTD) algorithm.

2.5. Computational Methods for Optical Modeling of Thin Film Solar Cells

Except for a few simple cases mentioned previously, Maxwell's equations are solved using computational tools, such as Finite Difference Time Domain (FDTD), Finite

Element Method (FEM) and Fourier Modal Method (FMM). FDTD is one of the most widely used Maxwell's equation solvers due to its accuracy and simplicity.

As a comparison of FDTD method with an analytical problem, the well known Mie scattering problem is simulated with FDTD and compared with the theoretical values. In Figure 2.8, the scattering and absorption cross sections for a sphere of 50 nm radius are presented, and the results from FDTD and Mie theory are compared.

2.5.1. Finite Difference Time Domain Method

FDTD is one of the widely used methods to model electromagnetic field components in a solar cell due to its simplicity and accuracy [30,85–88]. FDTD solves Maxwell's equations on a discrete spatial and temporal grid, which is called Yee's cell (Figure 2.9), named after Kane Yee, who developed the FDTD method. Yee's cell involves electric and magnetic field vectors along edges and perpendicular to the faces, respectively. The solution for electromagnetic equations is then obtained iteratively. The electric and magnetic fields on the solution domain are calculated by solving electromagnetic equations iteratively. The power crossing a plane, \vec{S} is then calculated by:

$$P = \frac{1}{2} \int_{\vec{S}} \text{Re}(\mathbf{E} \times \mathbf{H}) \cdot d\vec{S} \quad (2.18)$$

where \mathbf{E} and \mathbf{H} are electric and magnetic fields computed from FDTD simulations.

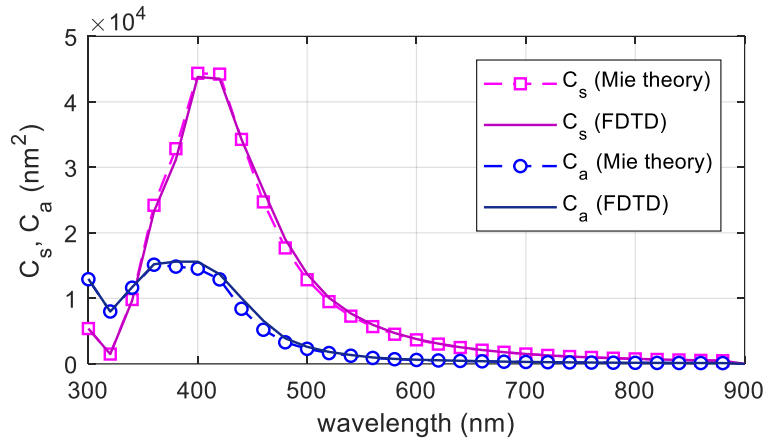


Figure 2.8. Comparison of scattering cross sections obtained from FDTD simulations and Mie theory for a 50 nm silver sphere.

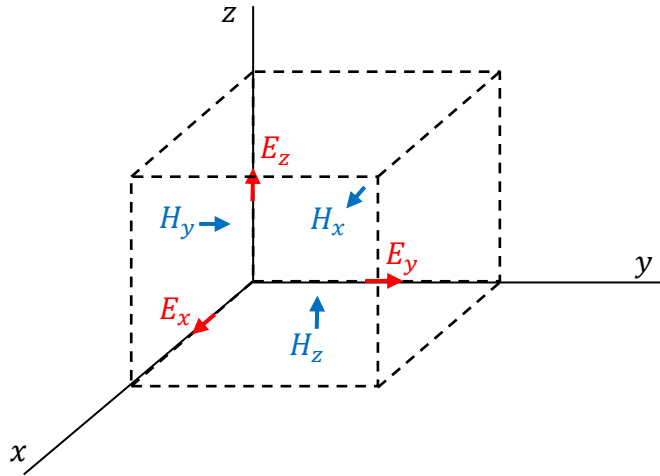


Figure 2.9. Yee cell and placement of electric and magnetic field vectors.

2.6. Conclusion

In this chapter, the background of solar cells is provided, and commonly used performance criteria and performance enhancement techniques are discussed. The

guidelines of TFSC design rely on these factors. For comprehensive performance analysis, optical and electrical modeling of TFSC is required. However, optical modeling alone, together with approximations, can provide valuable information on the solar cell operation without adding the computational cost of electrical simulations. Additionally, the environmental aspects of solar cell operation (e.g., reliability and stability) and higher level performance metrics (e.g., LCOE and energy yield) are not in the scope of the present study.

3. DESIGN OPTIMIZATION OF THIN FILM SOLAR CELLS USING NUMERICAL OPTIMIZATION

In this chapter, optimization methods with different complexity and computational cost are explained, and examples in TFSC design are discussed. First, the general optimization problem is formulated and explained. In Figure 3.1, a classification of numerical optimization methods is presented, and specific techniques are listed under the corresponding class. The ones used in TFSC design problems are detailed in Sections 3.2-3.7 with a review of the examples from literature. In Section 3.8, the TFSC design approaches are summarized and discussed.

3.1. Optimization Problem

Optimization is a branch of mathematics aiming to find the best value that an *objective function* $f(\mathbf{x})$ can take among the feasible values. Generally, an optimization problem is expressed as a *minimization* problem, and the algorithms are developed for minimization. Maximization can be considered as the minimization of $-f(\mathbf{x})$. The objective of minimization problems is also referred to as the *cost function* $C(\mathbf{x})$.

$$\begin{aligned} \min_{\mathbf{x}} f(\mathbf{x}), \\ g(\mathbf{x}) \leq 0, \\ h(\mathbf{x}) = 0, \\ x_i^L \leq x_i \leq x_i^U, \end{aligned} \tag{3.1}$$

where $g(\mathbf{x})$ and $h(\mathbf{x})$ are the inequality and equality constraints. x^L and x^U are the lower and upper bounds, which are generally imposed by the problem. The feasible set of solutions is the set of all possible values satisfying the problem constraints and bounds.

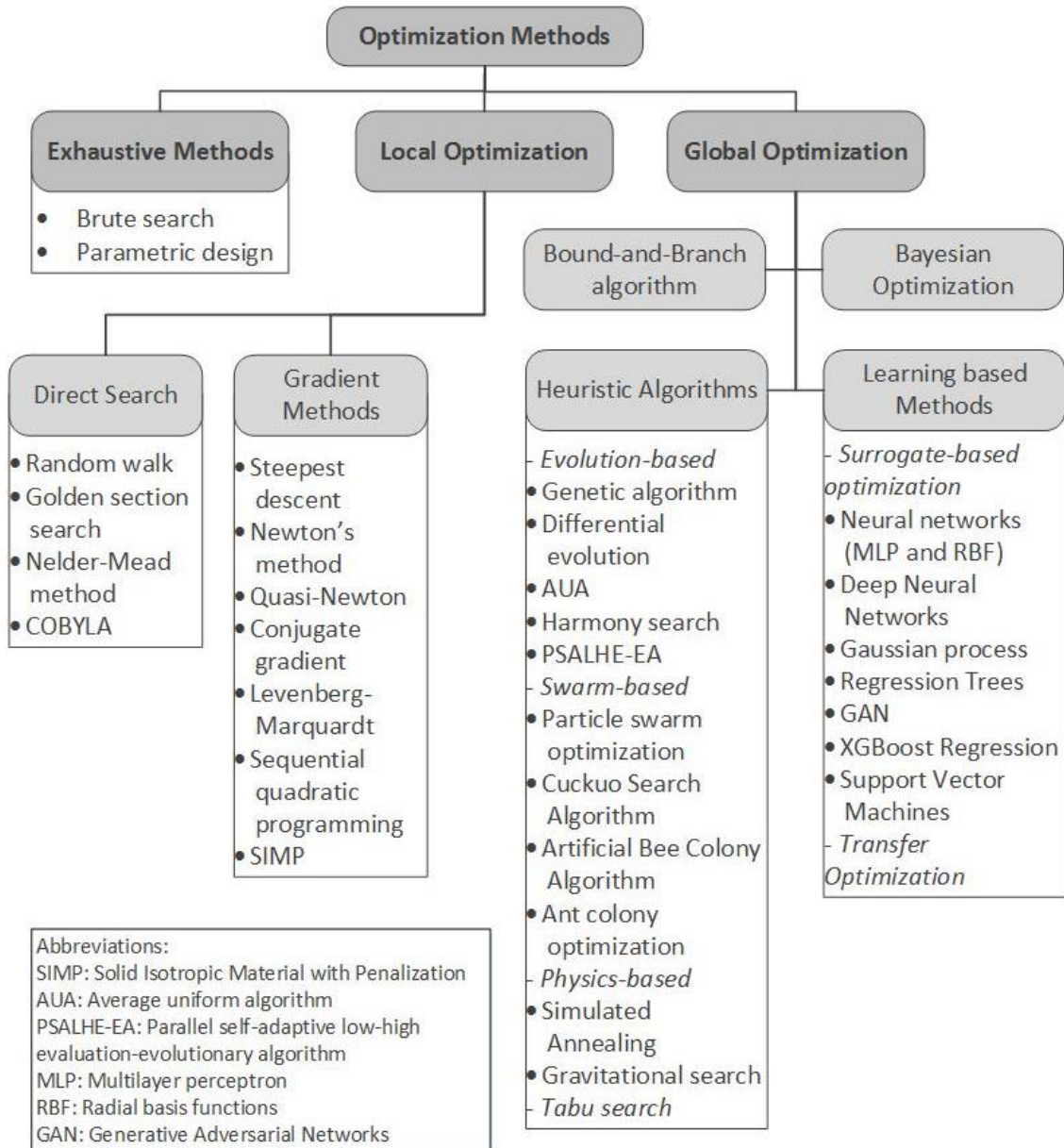


Figure 3.1. Classification of numerical optimization techniques.

3.2. Exhaustive Search

3.2.1. Exhaustive Search Theory

Exhaustive, or Brute force, search refers to enumerating all possible permutations of the design variables and evaluating outputs. Continuous variables can also be discretized to several intervals depending on the computational cost and desired accuracy. The advantage of the exhaustive search is that it is guaranteed to find the global optimum. However, the computational cost of calculating every possible input vector can be quite cumbersome. Although the design of several variables can be viable, the size of the input space exponentially grows as the number of variables increases. For example, if we discretize the input space by 5, 3 variables result in 125 different cases where 10 variables result in 9,765,625 different configurations.

3.2.2. Exhaustive Search in TFSC Design

Even though the exhaustive search has certain disadvantages, it has been widely used by researchers due to its ease of implementation and guarantee of finding optima. Jovanov et al. [73] designed periodically textured interfaces for amorphous silicon solar cells. The authors obtained the maps of short circuit current and optical losses with respect to the height and period of the interfacial textures. In [89], lumpy silver nanoparticles are designed for an ultra-thin lead halide perovskite solar cell for maximum absorption in order to decrease the use of toxic lead in perovskites. It was shown that the perovskite thickness could be reduced from 300 to 50 nm when nanoparticles are properly designed without sacrificing absorption. Agarvwal and Nair [90] studied the loss mechanisms in

perovskite solar cells and conducted a thickness optimization. Deparis et al. [91] designed pyramidal corrugated interfaces between a-Si and F-doped SnO₂ transparent conductive oxide layer for improved absorption performance. Another study on interface corrugation is conducted by Dewan and Knipp [92]. In their study, integrated diffraction gratings were optimized for maximum short circuit current and quantum efficiency. Ferry et al. [93] demonstrated the spatial correlations for light trapping nanopatterns and mapped corresponding external quantum efficiencies. Wiesendanger et al. [94,95] studied the optimization of randomly and periodically textured thin film solar cells for improved short circuit current. Tsai et al. [96] presented a methodology to optimize the optoelectrical performance of thin film organic solar cells. In [97], various light trapping techniques are investigated for c-Si and a-Si thin absorbers for maximum possible short circuit current. Hou et al. [98] designed a two-dimensional spiral grating for thin film silicon solar cells for maximum absorption. Design based on the parametric search is also worth mentioning. In several studies, TFSC design has also been performed by changing one variable at a time to maximize solar cell performance [99–101].

These studies share a common feature: the design vector is not more than a few dimensions. Exhaustive search methods become computationally unwise, and advanced design optimization techniques should be considered for higher degrees of optimization problems.

3.3. Direct Search

3.3.1. Direct Search Theory

Direct search is the generic name for the methods searching optimum without gradient information, such as random walk and pattern search. One should note that advanced random search methods, i.e., genetic algorithms, simulated annealing, and ant colony algorithms, are classified as heuristic methods as their search techniques are more sophisticated than those in this section.

A random walk is a direct search method where the next iteration is selected randomly [102]. The next point is kept if the current function value is better (smaller in a minimization problem, larger otherwise) and discarded otherwise. Random walk methods do not presume a probability distribution and do not select the next iteration according to previous knowledge, resulting in getting trapped in local optima or long computation times.

3.3.2. Direct Search in TFSC Design

Although not as often as the heuristics, direct search methods have been used in TFSC design problems by several researchers. In [103], Lin and Povinelli designed an aperiodic nanowire solar cell using a random walk strategy starting from a periodic structure. The authors could obtain absorption enhancement compared to the thin film and optimized periodic nanowires. Van Lare and Polman [64] followed a similar random search approach to optimize the light trapping structure of an a-Si solar cell. They optimized random arrays of Mie scatterers for increased power spectral density. Sheng et

al. [104,105] designed various interface textures for silicon solar cells and compared their absorption enhancements. The authors optimized Fourier series shaped textures using a nonlinear, constrained optimization algorithm by linear approximation (COBYLA), which could provide light trapping beyond the Lambertian limit.

3.4. Gradient Based Algorithms

3.4.1. Gradient Based Algorithms Theory

Gradient based optimization algorithms utilize the convexity of the objective function through first (and second) derivatives. One of the first examples of these algorithms, gradient descent, was proposed by Cauchy as early as the 1800s [106]. Another method for gradient based optimization is Newton's method, which is deduced from Taylor expansion of the function to be minimized. Gradient descent and Newton's methods are first and second order methods due to the degrees of derivatives in their formulations, respectively.

$$\mathbf{x}^{k+1} = \mathbf{x}^k + \Delta\mathbf{x},$$

Steepest descent:
$$\Delta\mathbf{x} = -\alpha\mathbf{g}, \tag{3.2}$$

Newton's method:
$$\Delta\mathbf{x} = -\mathbf{H}^{-1}\mathbf{g},$$

where α is the line step, which is determined iteratively, \mathbf{g} and \mathbf{H} are the gradient and the Hessian of the objective function, respectively. Newton's method takes only a single iteration to find the optimum of a perfectly convex function. Nonlinear functions are approximated convex near the vicinity of the current iteration, and the solution is updated every iteration. Generally, the Hessian is either unavailable (black box) or very costly to

compute; therefore, Hessian is calculated through approximation techniques, such as Broyden-Fletcher-Goldfarb-Shanno algorithm in Quasi-Newton methods (QN) [107].

3.4.2. Gradient Based Algorithms in TFSC Design

Gradient based methods are not often used in TFSC design optimization since the objectives in TFSC calculations are usually black boxes that do not have explicit gradients. Nevertheless, gradient based methods have been found successful by several researchers. For example, Yu et al. [108] implemented a gradient based topology optimization (SIMP) to design efficient light trapping structures and compared it with the genetic algorithm. They concluded that SIMP provides a comparatively efficient solution with a relatively small computational cost. In [109], Baloch et al. performed a full device optimization of a multilayer solar cell for maximum power conversion efficiency via several optimization algorithms available in the Matlab toolbox. The authors stated that gradient based algorithms could provide computational efficiency without sacrificing accuracy since their objective was smooth. Razei et al. [110] utilized a sequential nonlinear programming algorithm to optimize an AZO/i-ZnO/CdS/CIGS/Mo solar cell for minimum reflectance. Although gradient based algorithms operate faster than other methods, their performance mostly relies on the objective function shape and the initial point. One approach to overcome this burden is multi start where several optimizations are performed starting from different initial points, but this can overturn the computational advantage of gradient based methods. Another approach is to hybridize global optimizers with gradient based methods to combine the global search ability of heuristics and computational efficiency and local search ability of the gradient based techniques. In [111–113], a simulated

annealing and BFGS quasi Newton hybrid algorithm was used to optimize nanostructured amorphous silicon solar cells for maximum absorption enhancement compared to the bare silicon. The hybrid algorithm is shown to outperform the individual optimizers.

3.5. Heuristic Algorithms

3.5.1. Heuristic Algorithms Theory

Heuristic algorithms are advanced randomized search methods depending on the function value instead of gradient and Hessian of the objective. Well known examples of this class are the genetic, or evolutionary algorithms, particle swarm optimization, and simulated annealing.

The genetic algorithm [114] mimics the biological evolution that the individuals that are less fit to the environment are eliminated. The early studies of genetic algorithms in the 1970s were able to solve complex problems [115,116]. When the evolution concept is translated to optimization, the objective function is expressed as a “fitness”, and design vectors with less fitness are eliminated. The individuals in the population (sets of solutions) go through processes such as crossover to maintain the diversity and increase the likelihood of survival. The search begins with generating an initial random population and calculating their fitness (cost) values. Then individuals with the smallest fitness values are selected as elites and survive to form the next generation. Additional individuals are created by mutation and crossover operations on the parents (previous population). Each individual is represented as a binary “chromosome” consisting of “genes.” The flowchart of a simple genetic algorithm is presented in Figure 3.2.

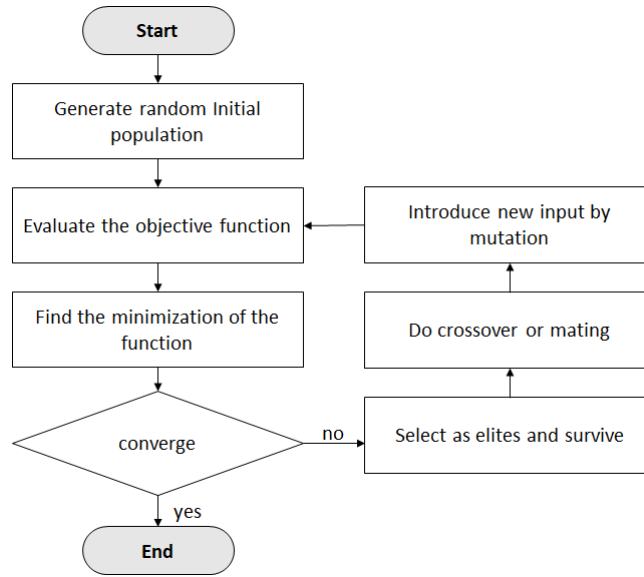


Figure 3.2. Flowchart of genetic algorithm.

Simulated annealing (SA) is a random search algorithm inspired by the annealing process of metals involving controlled cooling from high temperatures to reduce their defects. It was proposed by Kirkpatrick et al. [117] in the 1980s and has been used in various engineering optimization problems effectively. The method can select a worse candidate solution according to a probability calculated by the Metropolis criterion for a global search.

$$p_k = 1 + \exp\left(\frac{f(\mathbf{x}_{cand}) - f(\mathbf{x}_k)}{cT_k}\right) \quad (3.3)$$

The algorithm flow is summarized in Figure 3.3.

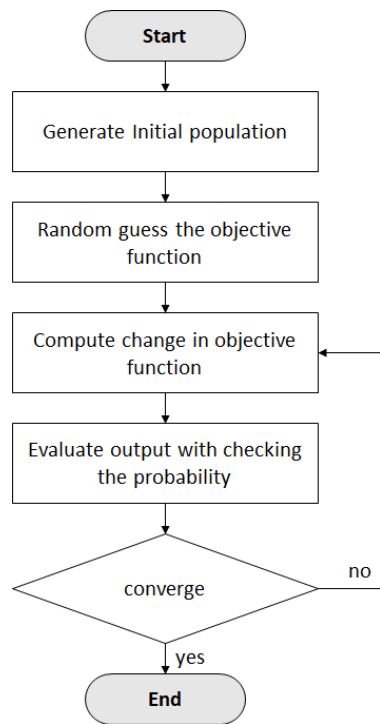


Figure 3.3. Flowchart of simulated annealing.

Particle swarm optimization (PSO) is another heuristic search algorithm to solve nonlinear problems introduced by Kennedy et al. [118]. The idea behind PSO is to simulate the social foraging behavior of some animals such as birds and fish. In general, the particles (sets of solutions) are moved around in the design space according to rules developed by their and overall swarm's best positions. The exploitation and exploration are maintained by the memory of the swarm and individual particles, respectively.

3.5.2. Heuristic Algorithms in TFSC Design

Genetic, or evolutionary, algorithms have been the most popular design approach in the last decade. Lin and Phillips [119] designed rectangular and arbitrarily shaped

gratings using a genetic algorithm for maximum quantum efficiency. In [120–122], the genetic algorithm is used to understand the energy coupling between metal nanoparticles and design photovoltaic cells with high absorptivity. As a result, they could achieve almost 50% improvement compared to the planar cell. In another study, Lin et al. [123] designed a lithographically fabricable random binary mask using a genetic algorithm. Each bit is assigned 0 or 1 according to occupying material in the quasi-random grating design.

Similarly, Wang et al. [124] designed the binary surface grating of an ultra-thin organic solar cell using a genetic algorithm. Compared to the planar design, 2400% absorption enhancement was obtained with the optimized structure, which is above three times the Yablanovitch limit. In a recent study, Gouvêa et al. [125] utilized a similar free geometry optimization approach for light trapping structures of a silicon solar cell using an evolutionary algorithm. In [126], Bittkau et al. studied the losses in a perovskite/c-Si tandem solar cells and designed an interlayer stack between subcells forming a Bragg reflector. The layer thicknesses were optimized for minimum losses, which resulted in an increase in short circuit current compared to optimized and arbitrary cells without interlayer. Muller et al. [127] demonstrated a comparison of quasi-random and periodically inverted pyramidal textures optimized by the genetic algorithm in terms of short circuit current of c-Si solar cells. In this design, realistic pseudo-random structures performed better than the periodic structures.

In addition to the conventional genetic algorithm, different evolutionary algorithms have also been implemented in TFSC design problems. In [128], a modified evolutionary algorithm, average uniform algorithm (AUA), is used along with the genetic

algorithm to optimize ten layers of antireflective coating stack for minimum reflectance. AUA was shown to achieve a similar efficiency with a faster convergence rate compared to the genetic algorithm. Differential evolution has also been used in several TFSC design studies. For instance, Zhao et al. [129–131] demonstrated its use in designing a-Si TFSC with various light trapping and antireflective coating materials for maximum optical performance. Additionally, Solano et al. [132] conducted a design optimization study for tandem solar cells made of a-Si:H alloys using a differential evolution algorithm. The aim is to maximize absorption efficiency while current is matched enforced by Kirchhoff's law. The differential evolution algorithm was also used by Zhou et al. [133] to design two level hierarchical particles for maximum possible short circuit current.

Genetic algorithms are especially preferred when there are multiple objectives. For example, in [134,135], Aiello et al. introduced the reduced volume of silver as the secondary objective to TFSC design problem in order to minimize material cost. For this purpose, they implemented a multiobjective optimizer, parallel self-adaptive low-high evaluation-evolutionary algorithm (PSALHE-EA).

Several researchers have also performed TFSC design optimization using simulated annealing algorithm. Kirsch and Mitran [136] developed a three dimensional optoelectronic model for organic solar cells using rigorous coupled wave analysis and designed a patterned thin film solar cell. With the proposed methodology, the designed solar cell could achieve a 15% improvement in the power conversion efficiency compared to planar cells. Jäger et al. [137] used the simulated annealing algorithm to optimize the coefficients of Perlin noise, which is used to generate the surface texture between silicon

absorber and transparent conductive oxide. Moreover, Hajimirza and Howell [138–140] explored the capabilities of simulated annealing in inverse design and analysis of TFSC to design surface textures and uncertainty modeling in fabrication.

Recently, particle swarm optimization has been utilized by several researchers to design TFSC. Arinze et al. [141] designed a PbS colloidal quantum dot solar cell for maximum possible photocurrent with different transparency. They showed that transparent and different colored devices could be realized, suitable for aesthetic purposes. Ferhati et al. [142,143] demonstrated particle swarm optimization on the design of silicon solar cells for maximizing absorption and minimizing reflection.

3.6. Learning Based Optimization Algorithms

3.6.1. Learning Based Optimization Theory

Learning based (response surface, surrogate based) algorithms have started to become popular with the rise of machine learning as an alternative to black box optimization with reduced cost [144–146]. These are data driven approaches where the state of undiscovered regions in the design space are predicted with the previous information. The main idea behind surrogates is to define an approximate function value, \hat{y} and to select function parameters so that the error between the real and approximate function values, ε is minimum.

$$y = \hat{y} + \varepsilon. \quad (3.4)$$

The key elements of surrogate based modeling are listed as follows [147]:

- 1. Design of (computer) experiments (DOE)** is the procedure of planning where and how to perform computer experiments. Sampling can be performed at once at the beginning (static, one-shot) or step-by-step according to a predefined rule (adaptive, sequential) [148]. Static methods are computationally feasible and representative at the low dimensional input spaces. However, over and undersampling is possible to occur, which may result in poor performance. Adaptive sampling optimizes the search by starting with an initial sample and updating the set of points based on the desired exploration-exploitation criterion [149–152]. Exploitation aims to cover highly nonlinear or *important* subspaces, while exploration targets undersampled regions [153].
- 2. Model fitting:** Once the training method is selected, the training process starts to minimize training error. Training error can be calculated in various ways, such as mean square error, mean absolute error and Bayesian acquisition functions. There are various models for approximating functions, such as Gaussian process [154], artificial neural networks [155,156], support vector machines [157], extreme gradient boosting [158] and so on. More details of different predictors are provided in Sections 3.6.1.1-3.6.1.5.
- 3. Model validation:** One of the critical points in the training is to monitor out-sample, i.e., validation error, to predict future performance and avoid *overfitting*. Furthermore, the size of hyperparameters can be found using validation error. There are several validation methods available in the literature, such as split-sample, cross-validation and bootstrapping. In the split-sample method, all data is

split into two separate sets for training and validation. Although this method is widely used, the training is likely to be biased based on the data. This bias can be eliminated by multiple training where the validation set is changed every time. This method is called cross-validation (CV). In CV, the data set is divided into n folds, and $(n-1)$ of them are used for training, while the rest is used for validation. At the end of the training, n training and validation error values are obtained, which can be used to determine the quality of the fit. In this study, cross-validation is used with $n = 4$. Bootstrapping (e.g., resampling) can be used when the number of data is extremely limited, in which the already available data is sampled multiple times to increase the number of data. Bootstrapping can be a suitable option when the data is experimental.

3.6.1.1. Neural Networks

Artificial neural networks (ANN) are one of the regression methods with significantly generalizable learning capabilities [159–161]. The advances in computation and parallel processing in training large ANNs have led to the very popular domain of deep learning. Figure 3.4 shows a general two-layer neural network for multiple inputs and a single output. Mathematical operations used for presenting input-output relations are also summarized in the figure at the corresponding positions. “+” sign and “ f ” stand for the summation of corresponding (input \times weight) pairs and transfer function, respectively. There is a variety of transfer functions to be used in NN given the problem nature and output space, such as linear ($\text{lin}(x) = x$), logarithmic sigmoid ($\text{logsig}(x) = (1 + \exp(-x))^{-1}$) and tangent sigmoid ($\text{tansig}(x) = \tanh(x)$).

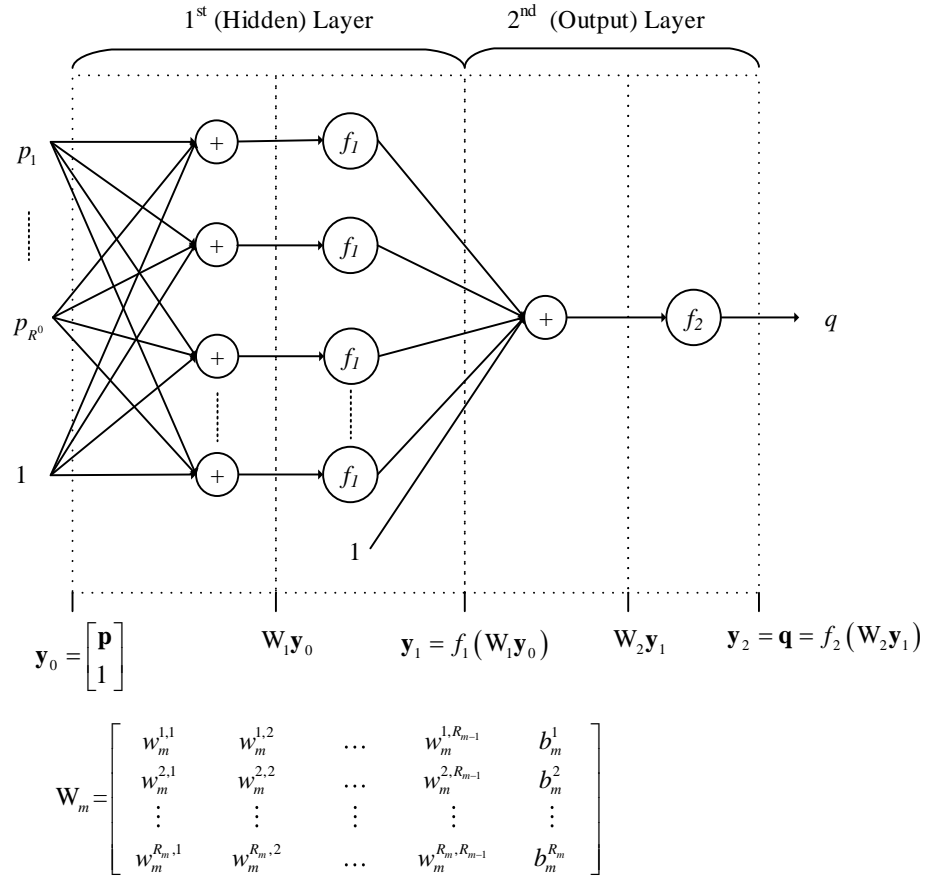


Figure 3.4. A two-layer NN architecture with multiple inputs and a single output. Adapted from [169].

The output of the NN model is

$$\begin{aligned}
f_{NN}(\mathbf{x}) &= \mathbf{y}_L \\
\mathbf{y}_i &= f_i(\mathbf{W}_i \mathbf{y}_{i-1}), \forall 1 \leq i \leq L,
\end{aligned} \tag{3.5}$$

where \mathbf{y}_i is the output vector and \mathbf{W}_i is the coefficient matrix of the i th layer, and L is the number of layers. \mathbf{y}_0 is the input vector normalized to within the $[-1 \ 1]$ range. The inputs are normalized through the transformation ($\bar{z}_1 = 2(z_1 - z_{1,min}) / (z_{1,max} - z_{1,min}) - 1$),

which eliminates bias among inputs. W_i is found as a result of NN training by minimizing the training cost function, $C(\mathbf{v})$:

$$C(\mathbf{v}) = \beta E_e + \alpha E_v, \quad (3.6)$$

where E_e and E_v are the sum of squared error (SSE) and sum of squared weights (SSW) respectively and calculated as follows:

$$\begin{aligned} E_e &= \mathbf{e}^T \mathbf{e} = (f_{NN}(\mathbf{x}) - \mathbf{y})^T (f_{NN}(\mathbf{x}) - \mathbf{y}), \\ E_v &= \mathbf{v}^T \mathbf{v}, \end{aligned} \quad (3.7)$$

where \mathbf{v} is the weight vector. E_v is a penalty term to avoid large coefficients, which results in overfitting. α and β are Bayesian regularization parameters set iteratively.

$$\begin{aligned} \alpha &= \frac{\gamma}{E_v}, \\ \beta &= \frac{E_e}{N - \gamma}, \end{aligned} \quad (3.8)$$

where γ is defined as the effective number of parameters and calculated as:

$$\gamma = \sum_{i=1}^{N_v} \frac{\lambda_i}{\alpha + \lambda_i}, \quad (3.9)$$

where λ_i is the i th eigenvalue of the Hessian of the sum of the squared error matrix, E_v . NN training is done using the Levenberg-Marquardt (LM) method with Gauss-Newton approximation for Hessian of $C(\mathbf{v})$. In this method, Jacobian of \mathbf{e} is sufficient to calculate gradient and Hessian, which reduces the computational cost by computing only the 1st derivative of \mathbf{e} . The backpropagation sensitivity concept enables this procedure. The details of the training algorithm can be found in [156,162].

3.6.1.2. Gaussian Process

Gaussian Process (GP) is a regression tool in which the prior knowledge of a data set is used to make new predictions [154]. The joint distribution of the observations and test values under prior is expressed via the joint normal distribution with zero mean and covariance.

$$\begin{bmatrix} \mathbf{y}_T \\ y_* \end{bmatrix} \sim \mathcal{N} \left(0, \begin{bmatrix} K(X_T, X_T) + \sigma^2 I & K(X_T, \mathbf{x}_*) \\ K(\mathbf{x}_*, X_T) & K(\mathbf{x}_*, \mathbf{x}_*) \end{bmatrix} \right), \quad (3.10)$$

where X_T and \mathbf{y}_T are the input and output sets for training (i.e., calculated previously). \mathbf{x}_* is the new data point to predict the output (y_*). K is the covariance matrix consisting of kernel functions, $k_{i,j} = k(x_i, x_j)$. Some of the examples for kernel functions are squared exponential and Matern 5/2 [154].

Consequently, the conditional distribution of y_* given \mathbf{y} is:

$$\mathcal{P}(y_* | X_T, \mathbf{y}_T, \mathbf{x}_*) \sim \mathcal{N}(\mu_y, \sigma_y^2). \quad (3.11)$$

Then, the mean of the prediction, μ_y and its variance σ_y^2 are calculated from:

$$\begin{aligned} \mu_y &= K(\mathbf{x}_*, X)[K(X, X)]^{-1} \mathbf{y}_T, \\ \sigma_y^2 &= K(\mathbf{x}_*, \mathbf{x}_*) - K(\mathbf{x}_*, X)[K(X, X)]^{-1} K(X, \mathbf{x}_*). \end{aligned} \quad (3.12)$$

3.6.1.3. Regression Trees

Decision trees are partition based prediction methods based on several decision rules [163]. A similar logic is used in classification trees (labeled outputs) and regression trees (continuous outputs). The advantages of the trees include easy visualization and inherent feature importance. On the other hand, trees are sensitive to small changes in the

data, and introduce bias, which can be a limiting factor. A sample tree is presented in Figure 3.5.

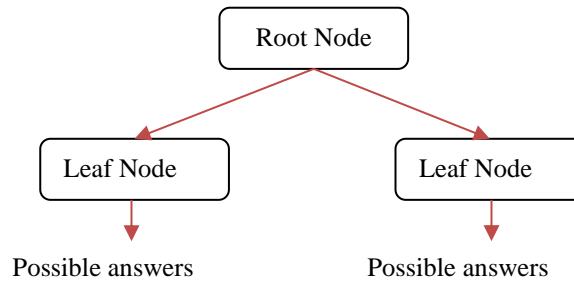


Figure 3.5. Decision tree representation.

3.6.1.4. Extreme Gradient Boosting (XGBoost)

XGBoost is one of the most recent machine learning methods, developed by Chen et al. in 2016 [158]. XGBoost is an ensemble of decision trees utilizing gradient boosting [164]. Boosting is a sequential technique that combines weak learners to improve accuracy. Yet, XGBoost is a more improved form of boosted trees, utilizing an advanced regularization approach, which stands out among similar models. Another strength of XGBoost compared to the other boosting algorithms, such as gradient boosting machine, is the easy implementation of cross validation.

3.6.1.5. Linear Regression

The linear models model the output as the linear combination of the inputs. Although a linear model can fail to express the nonlinearity, it can help establish the general trends in a problem. The predicted output of a linear model is:

$$\begin{aligned}\hat{y} &= m_0 + m_1x_1 + \dots, \\ \hat{y} &= M\mathbf{x},\end{aligned}\tag{3.13}$$

where $M = [m_0, m_1, \dots]^T$ is the coefficient vector.

3.6.2. Learning Based algorithms in TFSC Design

The use of machine learning methods in TFSC design problems is a relatively new concept where most of the examples have been proposed in the last few years. Mlinar discussed the application of machine learning techniques in solar energy previously [165]. Yosipof et al. [166] developed a data mining framework to design full metal oxide solar cells. In [167] a regression tree based optimization method is used for designing a multilayer a-Si solar cell, and its computational cost is compared with conventional heuristic optimization methods. In [168–171], artificial neural networks are used to express surrogate of absorptivity as a function of solar cell geometry and light properties, and numerical design is performed using this surrogate by the author. A similar approach is implemented in [172] by Hamedi et al. for predicting absorptivity of a nanowire solar cell design. The authors demonstrated the effectiveness of neural networks in predicting optical response and compared multilayer perceptrons and radial basis function method. Moreover, the application of Bayesian optimization in designing quasi-random solar cells is demonstrated in [173].

On the other hand, learning based methods have gained more extensive attention from the researchers in optical devices [174–182]. For example, in several studies [174–177], neural networks have been used to design nanostructures with the desired transmission spectrum. Liu et al. [174] proposed a tandem neural network structure to design a nanophotonic structure. Yu et al. [175] designed a plasmonic refractive index sensor with improved performance. Zhang et al. [176] conducted a performance optimization study for the plasmonic waveguide-coupled with cavities structure. In [177], graphene based photonic metamaterials are designed using adaptive batch normalization in the artificial neural network. Inampudi and Mosallaei [178] designed free form periodic metagratings for desired diffraction efficiency distribution. Asano and Noda [179] used deep learning to design two dimensional photonic crystal nanocavities with optimized Q factors. Reinforcement learning has been used in photonic design in a recent study by Sajedian et al. [183]. Peurifoy et al. [180] used neural networks to predict spectral scattering by layered spherical nanoparticles. In [181], deep neural networks are used to assist the differential evolution method in the photonics design problem. Jiang et al. [182] proposed a topology optimization framework based on generative adversarial networks for designing complex metasurfaces for desired optical performances. Although these studies do not directly target photovoltaic devices, since the modeling techniques and objectives are quite similar, it would not be surprising to expect more learning based applications in TFSC design in the near future.

3.7. Transfer Learning

Machine learning algorithms resemble human learning by collecting data for the task in hand and establishing reasonable connections between inputs and outputs. However, conventional machine learning methods start learning from scratch for every new task, unlike the way the human brain functions. The ability of the human brain to transfer knowledge among tasks can lend itself to smarter machine learning algorithms. This is officially known as transfer learning, which has proven to be a promising concept in data science.

Transfer learning has received the attention of data scientists as a methodology for taking advantage of available training data/models from related tasks and applying them to the problem in hand [184]. The technique has been useful in many engineering applications where learning tasks can take various forms, including classification, regression and statistical inference. Example of classification tasks that has benefited from transfer learning include image [185,186], web document [187,188], brain-computer interface [189,190], music [191] and emotion [192] classification. Regression transfer has received less attention compared to transfer classification [193]. However, there are few studies on regression transfer, some examples of which are configurable software performance prediction [194], shape model matching in medical applications [195] and visual tracking [196].

Despite the applications mentioned earlier, transfer learning in optimization problems has not been evaluated thoroughly except for a few fields. There are reports of transfer learning in automatic hyperparameter tuning problems [197–200] to increase

training speed and improve prediction accuracy. Transfer learning is also suitable for the iterative nature of the engineering design, where surrogate based optimization is utilized due to the complexity of the objective function. Li et al. [201] proposed a transfer learning based design space exploration method for microprocessor design. Min et al. [202] investigated the use of transfer learning in aircraft design problems and demonstrated the effectiveness of the proposed algorithms. Gupta et al. [184] reviewed the recent progress in transfer learning in optimization problems and categorized them as sequential, multitasking and multiform transfer optimizations. Recently, transfer learning has also been implemented in TFSC design problems by the author [203,204].

3.8. Conclusion

In this chapter, a review of thin film solar cell design is summarized. A comprehensive chart for the classification of numerical optimization methods is provided. The commonly used optimization algorithms are explained, and the examples from the literature are discussed. For an effective design process, the optimization method should be selected according to the nature of the problem. For TFSC problems, an algorithm that can handle high computational demand is required. In the rest of this dissertation, the learning based methods with heuristic techniques are employed for TFSC performance enhancement.

4. OPTICAL ENHANCEMENT OF THIN FILM SOLAR CELLS*

The optical efficiency of a solar cell can be enhanced by utilizing near field effects of nanoparticles embedded in the absorber layer, as explained in Section 2.3. In general, the size, shape and location of the nanoparticles play an important role in absorption enhancement [205,206], and poor designs can cause even decreased absorption [99,100,207]. The improvement in the absorbed power due to the presence of nanoparticles can be quantified by the absorption enhancement factor (EF). This quantity is defined as the ratio of the number of photons absorbed by the active layer of the plasmonic photovoltaic cell to the absorbed photons without plasmonic contribution (i.e., bare thin film). The calculation of the number of photons is detailed in Section 2.2.1. In mathematical terms:

$$EF = \left(\int \lambda \alpha_p(\lambda) I_{1.5AM}(\lambda) d\lambda \right) \left(\int \lambda \alpha_b(\lambda) I_{1.5AM}(\lambda) d\lambda \right)^{-1}, \quad (4.1)$$

where α_p and α_b are the portion of absorbed optical power by absorber layer of the solar cell with nanoparticles (plasmonic) and without nanoparticles (bare), $I_{1.5AM}(\lambda)$ is the AM

*Reprinted with permission from “Extremely Efficient Design of Organic Thin Film Solar Cells via Learning-Based Optimization” by M. Kaya and S. Hajimirza, 2017. *Energies*, 10(12), 1981, Copyright 2017 by MDPI.

*Reprinted with permission from “Surrogate based modeling and optimization of plasmonic thin film organic solar cells” by M. Kaya and S. Hajimirza, 2018. *International Journal of Heat and Mass Transfer*, 118, 1128-1142, Copyright 2017 by Elsevier Ltd.

*Reprinted with permission from “Application of artificial neural network for accelerated optimization of ultra thin organic solar cells” by M. Kaya and S. Hajimirza, 2018. *Journal of Solar Energy*, 165, 159-166, Copyright 2018 by Elsevier Ltd.

1.5 standard terrestrial solar spectrum [208] and integration is done over the wavelength range of interest.

EF can be used for the optical design optimization of organic solar cells (OSC). OSC is one of the most promising emerging solar cell types due to the ease of fabrication, inexpensive power generation and mechanical flexibility [24–26]. The power conversion efficiency of organic solar cells reached up to 17% as of 2020 [10]. However, due to the narrow absorption band of organic semiconductors, optical enhancement is needed for wide-scale commercialization.

EF is calculated for a photovoltaic cell structure in Figure 4.2 for $t_1 = 33$ nm, $t_2 = 20$ nm, $r = 5$ nm, $s = 11.5$ nm, and for different P , for validation of computational methods in the present study (FDTD). EF values in the present study computed using FDTD are compared with the Finite Element Method (FEM) simulations by Shen et al. [99] in Figure 4.1. The present result agrees well with the literature values.

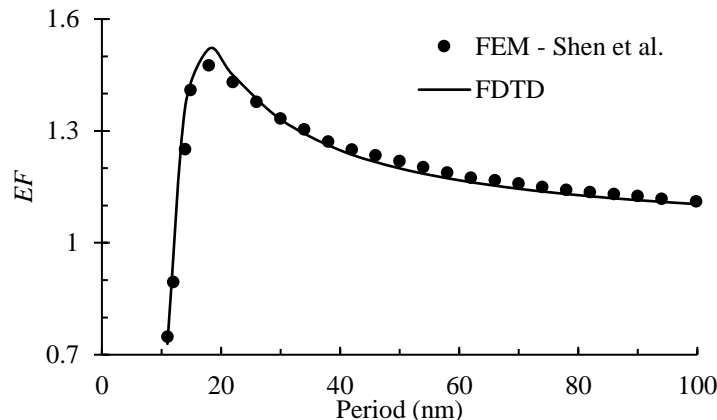


Figure 4.1. Comparison of the results of Finite Element Method (FEM) [99] and FDTD for a plasmonic OSC of $t_1 = 33$ nm, $t_2 = 20$ nm, $r = 5$ nm, $s = 11.5$ nm with respect to periodicity P . Adapted from [169].

In this chapter, two OSC design problems are considered. In the first problem (Section 4.1), Ag nanospheres are placed inside a poly(3-hexylthiophene):(6,6)-phenyl-C61-butyric-acid-methyl ester (P3HT:PCBM) layer. The absorber layer is stacked by poly(3,4-ethylenedioxythiophene): poly(styrenesulfonate) (PEDOT:PSS) and an Al back reflector layer. In the second problem (Section 4.2), P3HT:PCBM active layer with elliptical shape nanostructures is coated with antireflective indium tin oxide (ITO) and aluminum is selected as the back reflector. Two interlayers are also placed near the absorber layer. In each problem, the details of the surrogate model and optimization are presented, the results are presented and discussed, and the computational cost is compared to the conventional methods.

4.1. Thin Film Organic Solar Cells with Spherical Nanoparticles

A standard configuration of an OSC with silver nanospheres is demonstrated in Figure 4.2. The 3D view of the proposed OSC and the simplified 2D view are presented in Figure 4.2a and b, respectively. The problem is reduced from 3D to 2D based on the premises of the study by Moreno et al. [209]. In all the simulations of the present study, a plane wave source is propagated from top to bottom at a specified wavelength λ and at incident angle θ . Bloch and perfectly matched layer (PML) boundary conditions are imposed for x and z coordinates, respectively. Real and imaginary parts of the materials used in the simulations are in Appendix B.

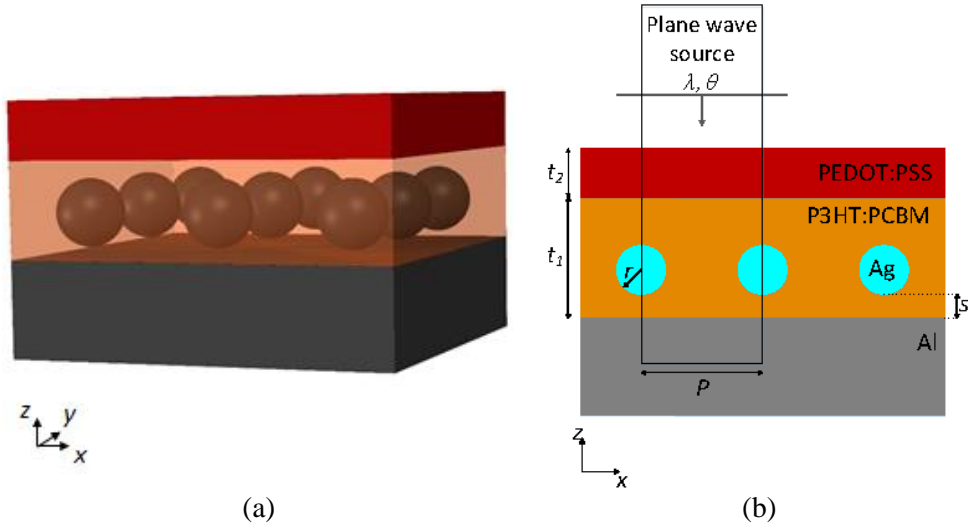


Figure 4.2. (a) 3D view of the OSC, (b) 2D Schematic of OSC with finite difference time domain (FDTD) solution domain. Adapted from [169].

4.1.1. Surrogate Model

The goal of this is to obtain an NN based surrogate model that approximates the absorptivity of the textured cell, $\alpha_p(\lambda)$ in equation (4.1), which is a function of geometry, wavelength and incident angle:

$$\hat{\alpha}_p(\lambda) = f_{NN}(t_1, t_2, r, s, P, \theta, \lambda). \quad (4.2)$$

Note that the absorbed power inside the bare solar cell can also be expressed using the same function f_{abs} by setting $r = 0, s = 0, P = 1$ (with a mesh size of 1):

$$\hat{a}_b(\lambda) = f_{NN}(t_1, t_2, 0, 0, 1, \theta, \lambda). \quad (4.3)$$

The training and validation data sets are obtained based on input values generated randomly between the lower and upper bounds of optimization. Furthermore, the wavelength is sampled between 300-900 nm and the angle of incidence is sampled between 0-89 degrees.

A $7 - R_1 - 1$ NN is then trained to learn the absorptivity model f_{NN} using the training data. The network has one hidden layer with $5 \leq R_1 \leq 50$ nodes. $\text{tansig}(\cdot)$ transfer function is used in both layers. 6,000 data are generated, and the validation error is monitored using the cross validation method with 4 folds. The number of neurons in the hidden layer is determined based on these errors. In this study, R_1 is determined as 30, which provides a good balance between simplicity and accuracy according to the results in Figure 4.3.

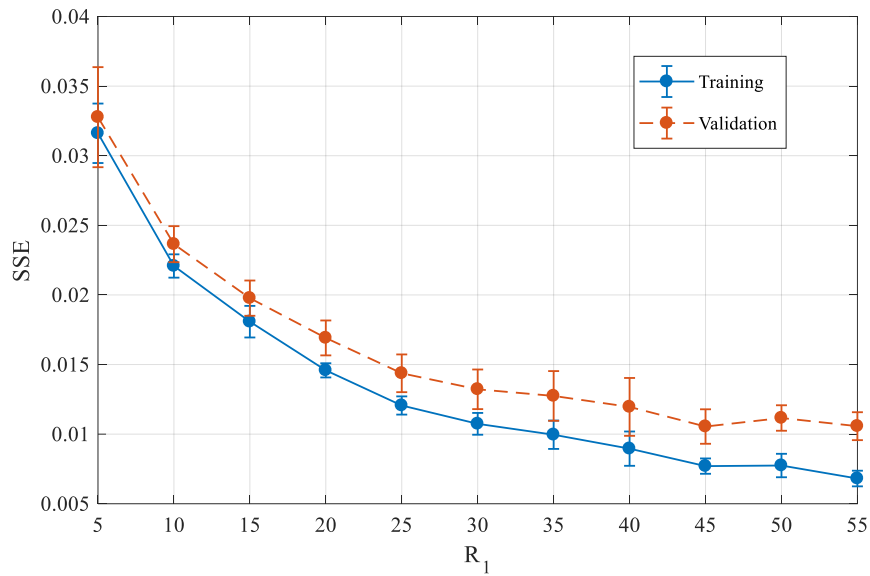


Figure 4.3. Normalized mean sum of squared error (SSE) with respect to the number of neurons in the hidden layer (R_1). Adapted from [168].

4.1.2. Optimization Problem

The objective of the present optimization problem is to maximize EF by modifying the cell geometry. One of the reasons for choosing EF as the objective function is that the

algorithm tends to minimize the active layer thickness when the aim is to maximize EF. Thus, the possibility of recombination is also decreased, although photocurrent is not considered as the objective. The present optimization problem can be formulated as:

$$\begin{aligned}
& \max_{\mathbf{x}} EF(\mathbf{x}), \\
& \text{Subject to: } r < t_1/2, \\
& \quad s < t_1 - 2r, \\
& \quad r < P/2, \\
& \quad \mathbf{x}^L < \mathbf{x} < \mathbf{x}^U,
\end{aligned} \tag{4.4}$$

where \mathbf{x} is the geometry vector with Ag nanoparticles and \mathbf{x}_b is the bare geometry without the nanoparticles, i.e., $\mathbf{x}_b = [t_1, 0, 0, 1, t_2]^T$ and the lower and upper limits for the geometry vector are $\mathbf{x}^L = [10, 0, 5, 5, 5]^T$ and $\mathbf{x}^U = [100, 50, 50, 200, 100]^T$. The bounds are the same as the bounds of training and validation sets except the lower bound of s . $s^L = 5 \text{ nm}$ in order to avoid short circuit possibility due to the Ag–Al contact. $EF(\mathbf{x})$ is then calculated as the ratio of the integrals in the numerator and denominator of equation (4.1) by using the trapezoidal method by evaluating the output of the surrogate model $f_{NN}(\mathbf{x}, \lambda, \theta)$ and $f_{NN}(\mathbf{x}_b, \lambda, \theta)$ for each wavelength increment (1 nm). The cost function in the optimization problem, however, is set to the inverse of EF , and penalty terms are added [107] in order to obtain an unconstrained minimization problem.

4.1.3. Results and Discussion

The optimized geometry obtained by the NN based optimization procedure with QN and SA methods is presented in Table 4.1 for two different initial guesses. NN-SA-QN refers to the hybrid optimization algorithm in which QN is used after the SA algorithm to find the global optimum in the vicinity.

Table 4.1. Optimized geometry of plasmonic OSC and corresponding enhancement factor (EF) values. Adapted from [168].

Method	$[t_1, r, s, P, t_2]_{init.}^T$	$[t_1, r, s, P, t_2]_{opt}^T$	EF
NN-QN	$[50, 20, 5, 100, 50]^T$	$[46, 20, 5, 99, 50]^T$	1.26
NN-SA	$[50, 20, 5, 100, 50]^T$	$[24, 9, 6, 51, 87]^T$	2.21
NN-SA-QN	$[50, 20, 5, 100, 50]^T$	$[24, 9, 6, 51, 87]^T$	2.21
NN-QN	$[40, 11, 15, 80, 20]^T$	$[33, 10, 16, 82, 14]^T$	1.25
NN-SA	$[40, 11, 15, 80, 20]^T$	$[26, 10, 6, 51, 87]^T$	2.14
NN-SA-QN	$[40, 11, 15, 80, 20]^T$	$[24, 9, 6, 51, 89]^T$	2.22

Note that the SA algorithm performs better for finding the global optimum and is less likely to get trapped in local optima, unlike QN. Figure 4.4 compares the optimized plasmonic, the bare, and a random design. The random design is the initial point of the optimization. The electric fields near the nanoparticle are also presented at various wavelengths. In Figure 4.5, the variation of EF during iterations is presented for these three algorithms and for two different initial guesses.

4.1.4. Computational Cost

A sample set of 6,000 points is used to construct the NN and the average duration for a single simulation (at a single wavelength) is 5 minutes. If a full fidelity optimization was desired, the calculation of EF would take 72 simulations where each plasmonic and bare geometry is simulated between 300-650 nm spectrum (solar cell absorption becomes negligible beyond 650 nm). Therefore, 6,000 simulations correspond to ~ 83 EF calculations, which is a significantly small number for a general optimization study.

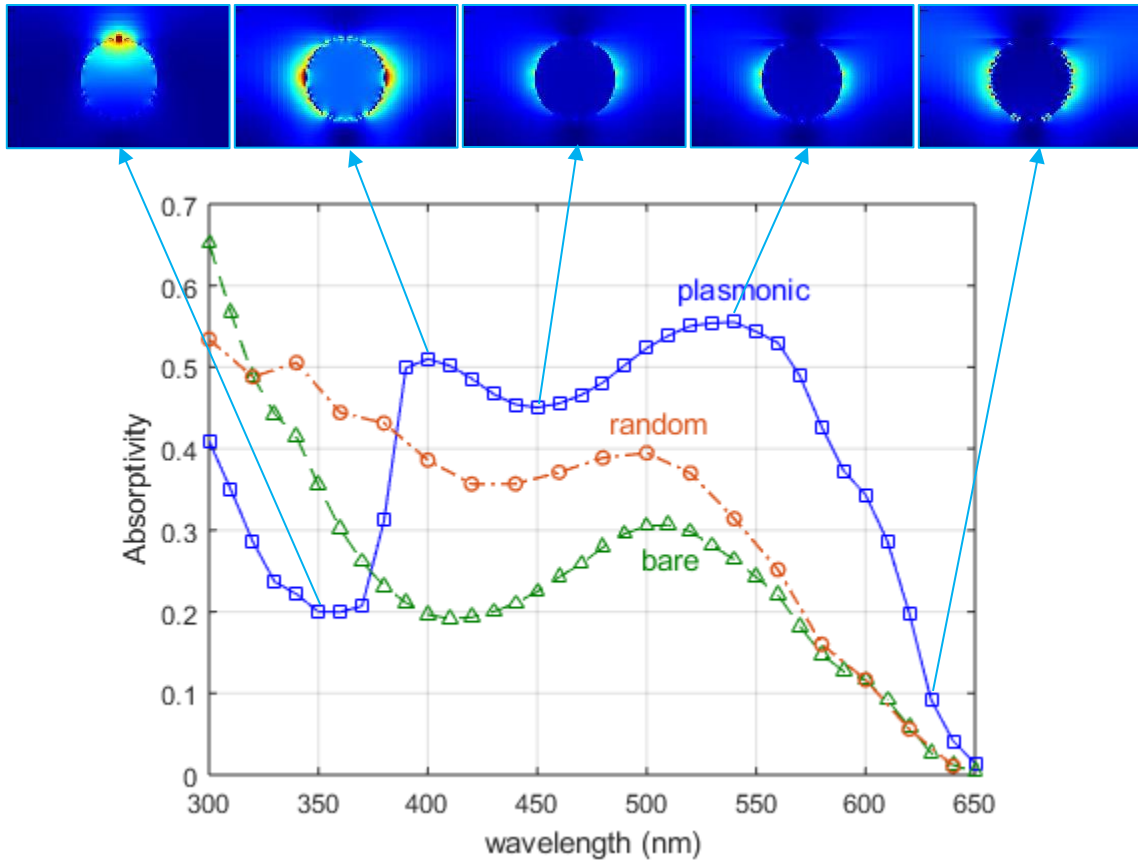


Figure 4.4. Spectral absorptivity of plasmonic, bare and randomly designed solar cells with $\mathbf{x}_p = [24, 9, 6, 51, 89]^T$, $\mathbf{x}_b = [24, 0, 0, 1, 89]^T$ and $\mathbf{x}_r = [40, 11, 15, 80, 20]^T$.

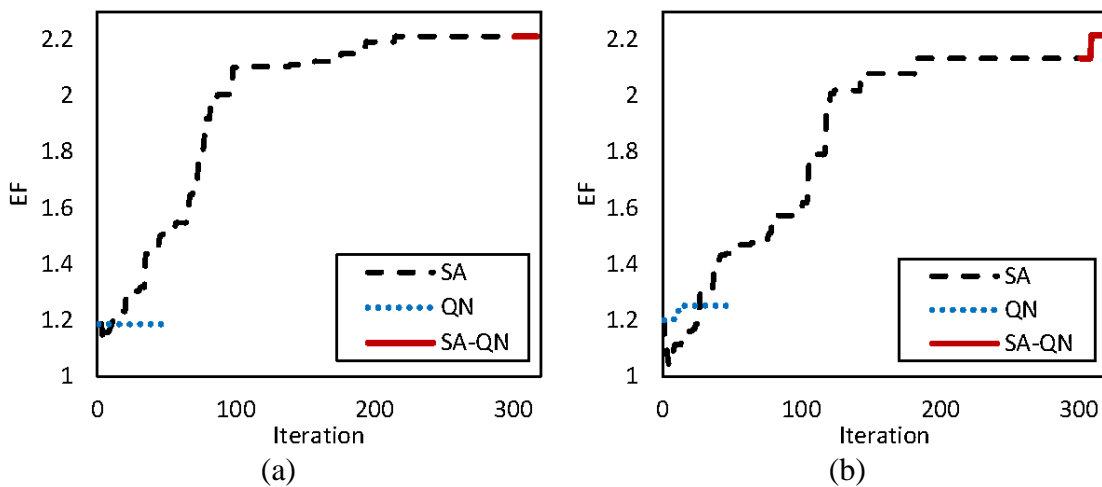


Figure 4.5. Evolution of EF during iterations of SA, QN and hybrid SA-QN for the initial guess (a) $[50, 20, 5, 100, 50]^T$; (b) $[40, 11, 15, 80, 20]^T$. Adapted from [168].

4.2. Thin Film Organic Solar Cells with Elliptical Nanoparticles and Interlayers

The structure of the solar cell used in the present study is shown in Figure 4.6. In this design, the organic bulk heterojunction blend P3HT:PCBM is preferred in the absorber layer, aluminum is selected as the back reflector, and OSC is coated with antireflective indium tin oxide (ITO). Electron and hole transport layers, ZnO and MoO₃, are also included in the design to be optimized [210,211].

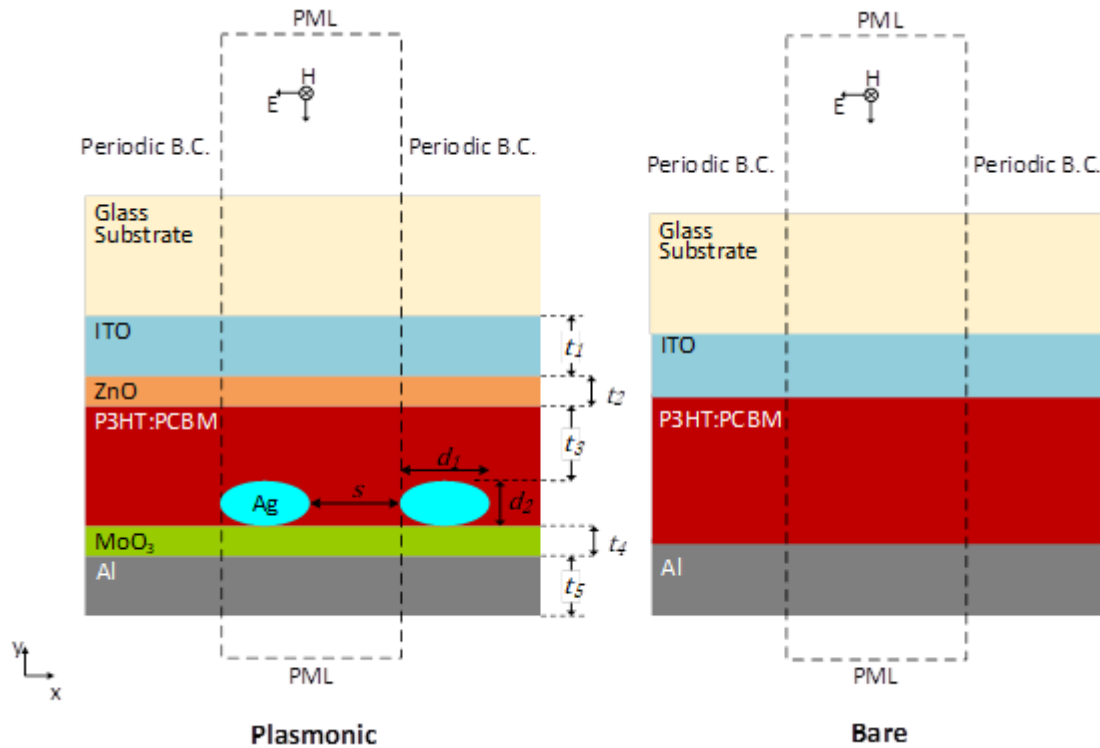


Figure 4.6. OSC device with design parameters specified. Adapted from [170].

The nanostructures are located near MoO₃ because the absorption enhancement in a solar cell is found more significant when plasmonic nanostructures are placed away from

the interface where light enters (back zone) [100]. Ag particles have elliptical shapes. A 2D surface texture is aimed to be modeled with two diameters for the elliptical nanotextures. However, the same design can easily be extended to 3D by only adding more input variables, namely ellipsoid diameter and spacing variables in the z direction. Distance between nanostructures and ZnO layer is taken as a design variable instead of the overall thickness of P3HT:PCBM, in order to avoid a possible short circuit ($t_3 > 0$).

4.2.1. Surrogate Model

NN model is trained where the generalization error is quantified using the cross-validation technique. This time, the number of data used in training is increased by 1000 during incremental training. In Figure 4.7, the mean sum of squared error change with the number of neurons in the hidden layer and the number of total training data is presented for training and validation. Figure 4.7 shows that training error is independent of the number of training data but is a function of the NN model itself. On the other hand, the validation error is decreased to a certain level as the training set covers the input space better and converges.

From the results shown in Figure 4.7, 3000 to 4000 data points can be concluded as sufficient, with 4000 being preferable. However, all four different training scenarios (number of training data) will be considered in the optimization; therefore, 80 different NN models are saved to be used in the next step.

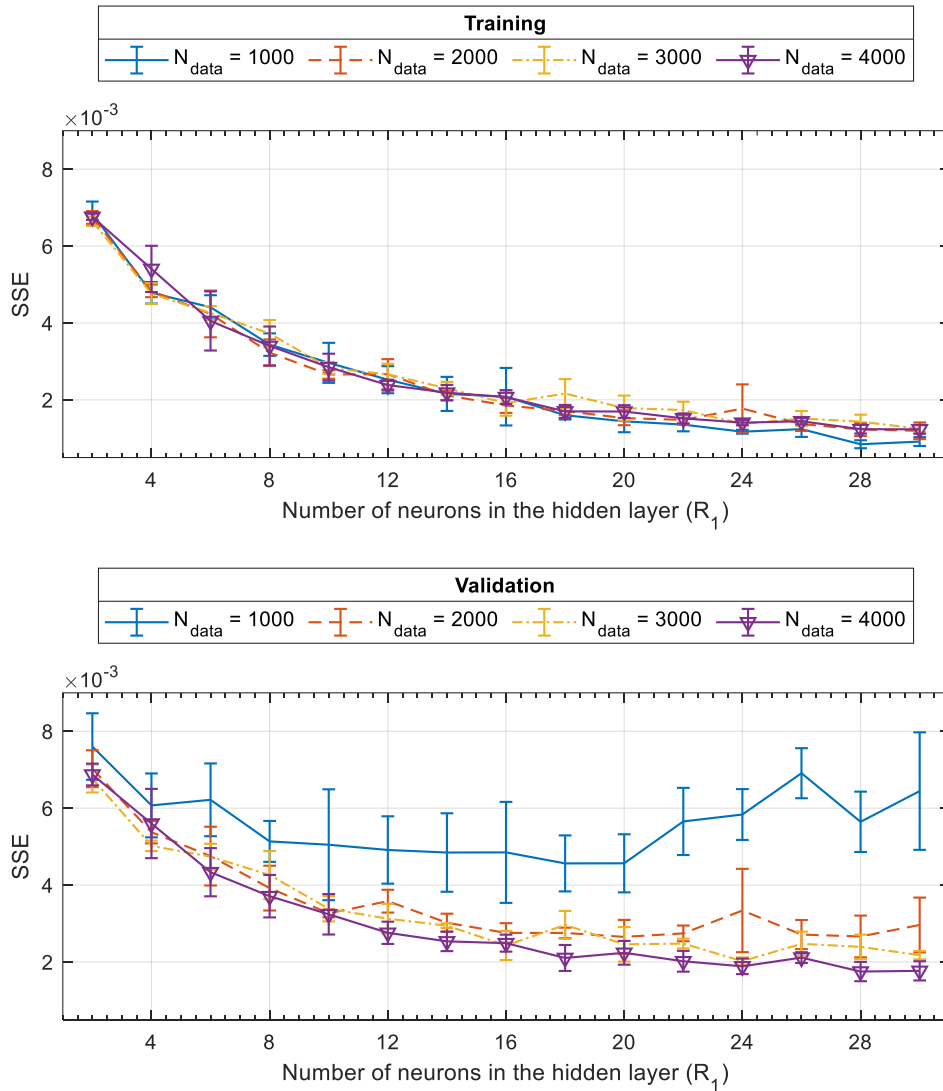


Figure 4.7. Mean sum of squared error (SSE) of training (top) and validation (bottom) sets with respect to the number of neurons in the hidden layer (R_1). Adapted from [170].

4.2.2. Optimization Problem

The aim of the present study is to optimize the organic solar cell structure to obtain the maximum absorption enhancement factor (EF) possible. EF is calculated as a function

of OSC geometry using the surrogate function $f_{NN} \approx f_{abs}$ for the absorptivity. The present optimization problem can thus be formulated as:

$$\begin{aligned} & \max_{\mathbf{x}} EF(\mathbf{x}), \\ & \text{Subject to: } \mathbf{x}^L < \mathbf{x} < \mathbf{x}^U, \end{aligned} \quad (4.5)$$

where $\mathbf{x}_p = [t_1, t_2, t_3, t_4, t_5, d_1, d_2, s]^T$ is the geometry vector with Ag nanostructures and $\mathbf{x}_b = [t_1, t_3, t_5]^T$ is the bare geometry without the nanostructures and interlayers. The lower and upper limits for the geometry vector are: $\mathbf{x}^L = [10, 5, 20, 5, 20, 10, 10, 1]^T$ and $\mathbf{x}^U = [100, 50, 100, 20, 120, 50, 50, 100]^T$, which are the same as the boundaries of ranges from which training and validation data are generated.

4.2.3. Results and Discussion

The optimization results are presented in two successive steps: first, the results of the preliminary optimization (surrogate based) are presented, and then the results of direct optimization within the narrowed bounds are shown. Preliminary optimization is performed using 20 different NNs for every number of training data points. As a result, 80 different NN models are obtained and used in optimization. Even though 4000 data is found the best representative model (smallest validation error) among others in the previous section, optimization is repeated with the corresponding NN models for completeness. The maximized EF values as a result of the optimization, are presented in Figure 4.8.

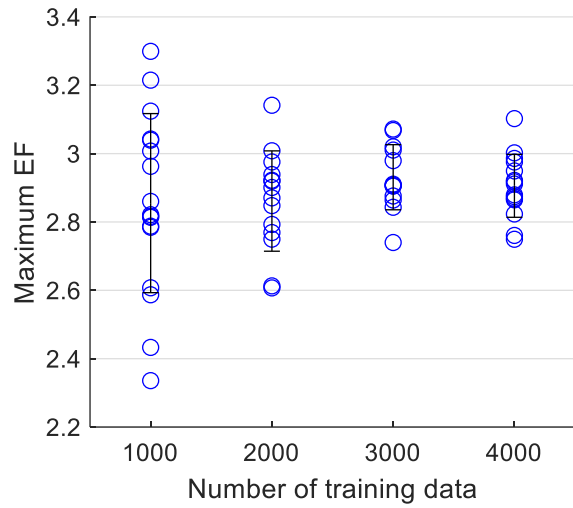


Figure 4.8. Maximized absorption Enhancement Factor as a result of NN based optimization. Adapted from [170].

Figure 4.8 shows that the uncertainty between different NN models decreases as the number of training data is increased. The maximum EF converges to 2.91, with a standard deviation of 0.09 for 4000 data points. The median of EF values is also 2.91. For 3000 data points, the median EF is also 2.91 with a mean value of 2.93 and a standard deviation of 0.09. It can be concluded from Figure 4.8 that although the NN with 4000 data is found to be better than the NN with 3000 points regarding the generalization performance, they converged to the same maximum objective value. The optimal values of the design variables are shown in Figure 4.9 separately.

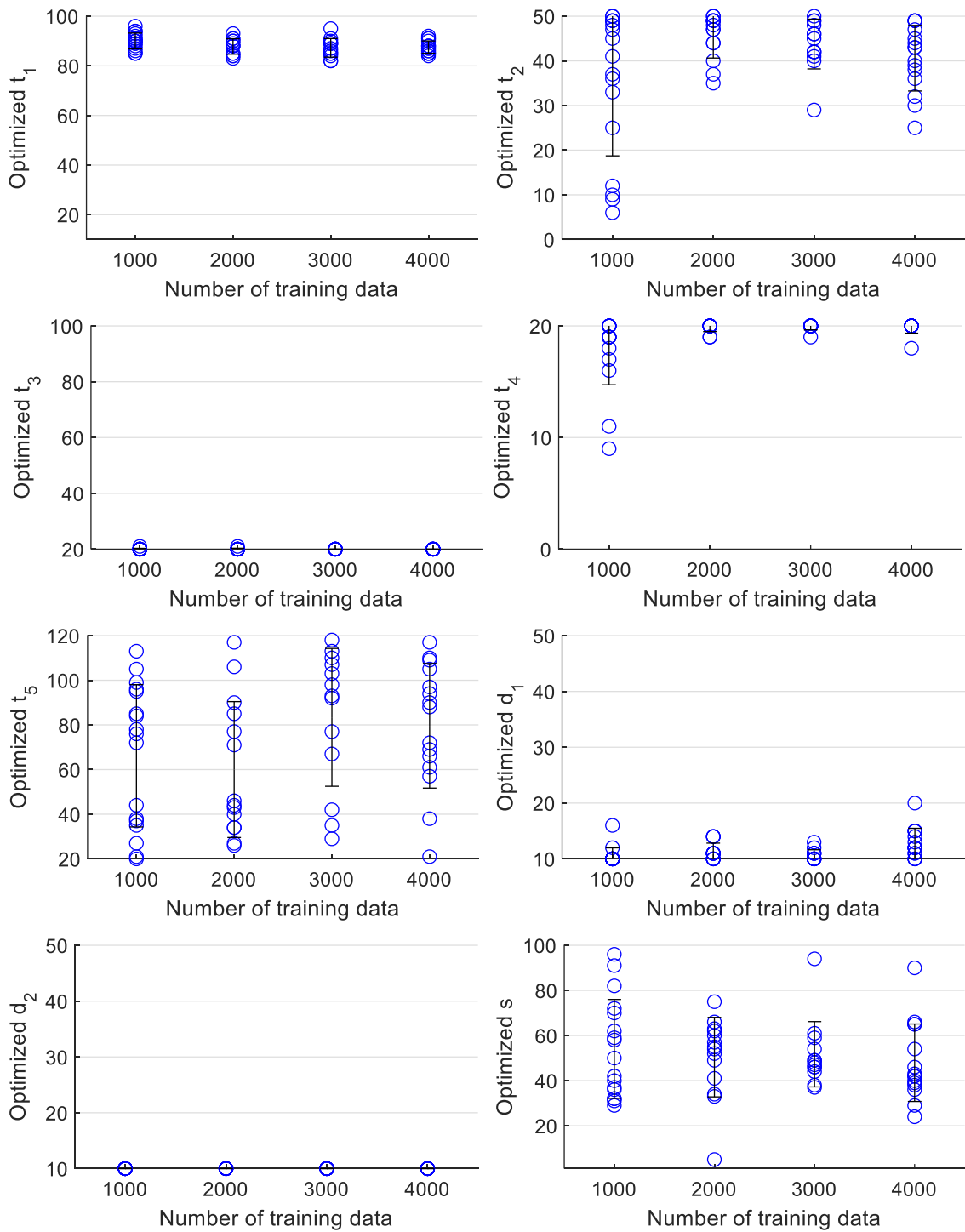


Figure 4.9. Optimal values of design variables. Each point represents the result of a single optimization. Adapted from [170].

The first conclusion drawn from Figure 4.9 is that the maximum enhancement is obtained when the absorber layer thickness is the smallest ($t_{3,min} + d_{2,min} = 30 \text{ nm}$). This is justified by the fact that the optical absorption is very small in the bare structure when the absorber is thin. However, this also indicates that even if the absorber is ultra-thin, almost 3 times more photons can be absorbed when the plasmonic particles are used. Furthermore, the optimal thickness of ITO converges to $t_1 = 87 \text{ nm}$. On the other hand, some of the variables, such as ZnO and MoO₃ converge to the upper bound of optimization, which implies that the corresponding bounds should be shifted upwards. Additionally, the optimal values for Al and spacing between nanostructures do not converge to a consistent value as the number of training data points increases. This can be due to two reasons: (1) the input has a negligible impact on the output; thus, the optimal value can vary a lot; (2) the input has a strong effect on the output, and NN fails to represent this effect.

In order to investigate these effects on the OSC design, we conducted a subsequent optimization study using high fidelity simulations instead of their surrogates within narrowed optimization bounds. The bounds are narrowed down to the values in Table 4.2, based on results from surrogate based optimization. The optimal input vector \mathbf{x}_{opt} is also tabulated. Evolution of EF during iterations is plotted in Figure 4.10.

Table 4.2. Updated optimization bounds and optimization results. Adapted from [170].

	t_1	t_2	t_3	t_4	t_5	d_1	d_2	s
\mathbf{x}_{LB}	87	20	20	15	20	10	10	20
\mathbf{x}_{UB}	87	70	20	50	120	20	10	80
\mathbf{x}_{opt}	87	37	20	28	107	15	10	25

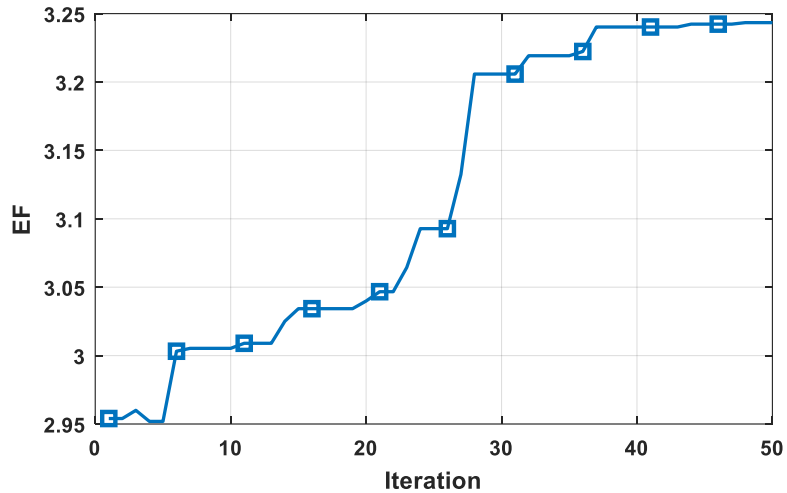


Figure 4.10. Evolution of enhancement factor during iterations of direct optimization. Adapted from [170].

The optimized geometry resulted in a 325% absorption enhancement in a 30 nm P3HT:PCBM with 10/15 nm-dia Ag nanostructures. The resulting absorptivity profiles for optimized plasmonic and bare structures are presented in Figure 4.11. According to the direct and surrogate based optimization results, optimized design variables (except MoO_3) are found in the feasible range suggested by surrogate based optimization. For example, optimized ZnO thickness is very close to the corresponding mean value (40 nm) found in surrogate based optimization. Even though optimized spacing and Al thicknesses are not as well predicted as ZnO, their optimized values are also within the same range found by surrogate based optimization.

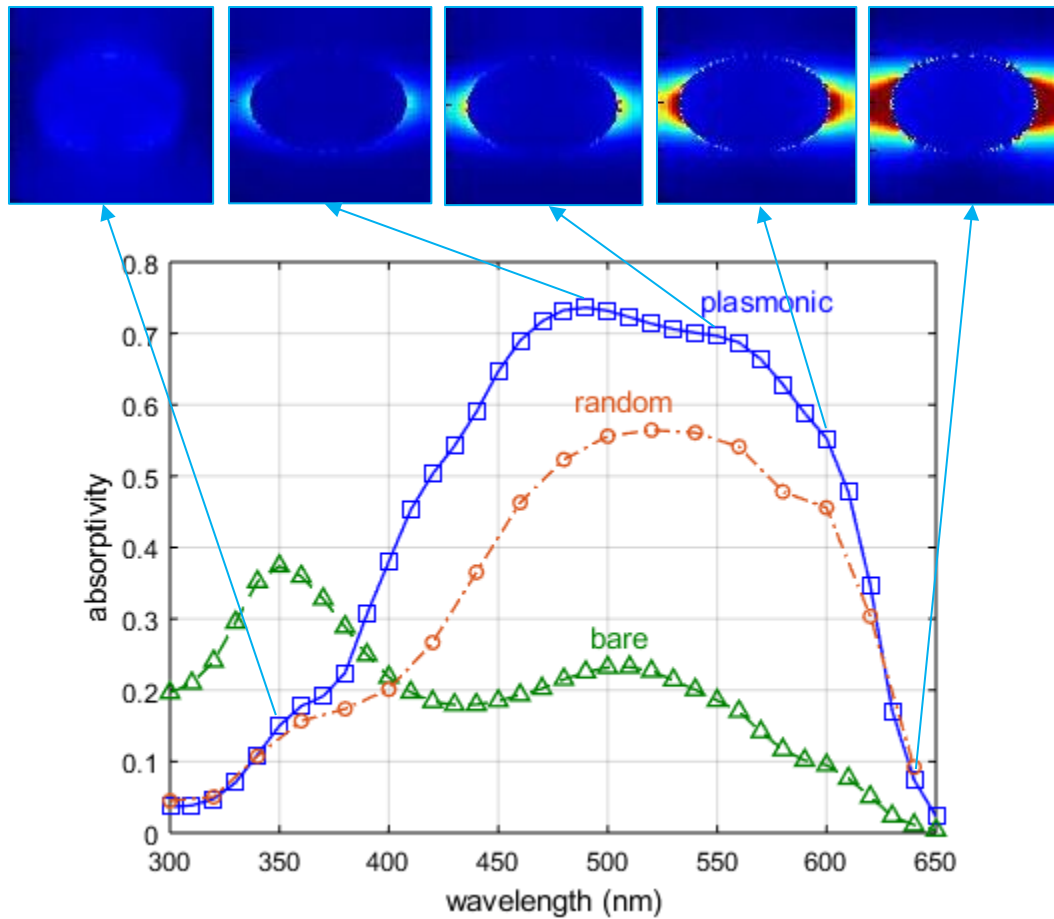


Figure 4.11. Spectral absorptivity of plasmonic, bare and randomly designed solar cells with $(\mathbf{x}_p = [87,37,20,28,107,15,10,25]^T)$

4.2.4. Computational Cost

A summary of the computational requirements of the operations is listed in Table 4.3. The computational cost of the surrogate based optimization method can be quantified based on the total CPU clock time which is needed to complete (1) an FDTD simulation of a geometry at a particular wavelength, (2) NN training time using an average number of neurons ($R_l = 16$) with CV, (3) complete SA search using NN surrogate function.

Table 4.3. Computation times of corresponding operations. Adapted from [170].

FDTD Simulation for $\alpha(x, \lambda)$	t_{fdd}	~180 sec.
NN training with CV (500 iterations)	t_{NN}	~160 sec.
SA algorithm (500 iterations)	t_{SA}	~20 sec.

The number of data points used in this study is 4,000. The time required to collect this data is equivalent to the time needed to run 55 direct EF simulations (when wavelength step for integration is 10 nm). To construct the information in Figure 4.7, $T_{NN} = 4 \times 15 \times t_{NN} = 9,600$ seconds are necessary for 4 different numbers of data points, and 15 different numbers of neurons. Optimizations took $T_{SA} = 4 \times 20 \times t_{SA} = 1,600$ seconds. Therefore, in addition to the time devoted to generating training data, $T = T_{NN} + T_{SA} = 11,200$ seconds were necessary to complete surrogate based optimization. This is equivalent to 0.8 direct EF simulations. Therefore, in general all actions of model fitting and training take negligibly less amount of time than data collection. Adding the computational cost of direct optimization shown in Figure 4.10, 106 full simulations could be performed in the given time. For an 8-dimensional design space, 106 simulations is very unlikely to get us close to the optimal vector using a method like SA. Furthermore, surrogate based approach provides more flexibility for other variations of optimization, e.g. when bounds are changed for some variables. Utilizing more powerful sampling methods can accelerate this procedure even further.

4.3. Conclusion

In this chapter, two plasmonic thin film solar cells are optimized for maximum optical enhancement. The optimization procedure resulted in more than 200% and 300%

enhancement in absorption, respectively. The required computational power is reduced compared to the expectations. Two approaches of surrogate based optimization are used in this chapter. First, a single NN model is obtained through training and used for optimization. In the second approach, NN models used in a way to construct an ensemble, and a secondary high fidelity optimization is performed based on the narrowed optimization bounds.

5. DESIGN OPTIMIZATION OF THIN FILM SOLAR CELLS FOR MAXIMUM OPTOELECTRICAL EFFICIENCY[†]

The optoelectrical efficiency of a solar cell can be quantified by external quantum efficiency (EQE). As discussed in Section 2.2.3, EQE measures the fraction of incoming photons that are converted to electricity. Therefore, the absorption and recombination losses should be considered simultaneously while calculating EQE.

In this chapter, an approximate formulation for EQE is developed and used for a thin film solar design study. An amorphous silicon thin film solar cell with ITO, SiO₂, Al₂O₃ and Al layers is considered in this chapter. First, the details of the approximate EQE formulation are presented in Section 5.1. In Section 5.2, the schematic of the solar cell is presented, and the material selection is explained. Section 5.3 and 5.4 presents the details of the optimization procedure. The results are presented and discussed in Section 5.5 and computational cost comparison is presented in Section 5.6. In the last section, the key results of this chapter are summarized.

5.1. External Quantum Efficiency Formulation for Planar Thin Film Solar Cells

EQE is highly correlated with the short circuit current. As explained in Section 2.2.4, the short circuit current is the current when no voltage is applied to the solar cell.

[†] Reprinted with permission from “Rapid Optimization of External Quantum Efficiency of Thin Film Solar Cells Using Surrogate Modeling of Absorptivity” by M. Kaya and S. Hajimirza, 2018. Nature Scientific Reports, 8, 8170, Copyright 2018 by Springer Nature.

EQE has two components: internal quantum efficiency (IQE) and absorption efficiency (η_A). IQE can be calculated from:

$$\eta_I(\lambda) = \frac{N_e}{N_p} = \frac{J_{sc}/q}{N_p} = \frac{1}{N_p} \frac{1}{q} \left[q \iiint n_p(x, y, z, \lambda) \mathbb{P}_c(x, y, z) \, dx dy dz \right], \quad (5.1)$$

$$\eta_I = \int \eta_I(\lambda) \, d\lambda$$

where J_{sc} is the short circuit photocurrent density, q is the elementary charge, n_p is the carrier generation rate (\mathbf{g} in equation (2.6)), \mathbb{P}_c is the *collection probability* defined as the probability that a carrier generated due to absorption contributes to the photocurrent. The carrier generation rate is equal to the number of absorbed photons, assuming every absorbed photon creates an electron-hole pair. Similar to Section 2.2.1, the spatial and spectral generation rate is calculated as:

$$n_p(x, y, z, \lambda) = hc [\lambda \alpha(x, y, z, \lambda) I(\lambda)]. \quad (5.2)$$

There are various analytical and computational methods to calculate \mathbb{P}_c . In this work, a probabilistic model of EQE similar in principle to those of Xue et al. [39,40], which preserves the dependence of collection probability to the absorber thickness and diffusion length. The essence of the model is as follows: In general, in a p-n junction solar cell, \mathbb{P}_c is unity in the depletion region and decreases exponentially as the distance from depletion region increases [37,38]. Only the vertical position inside the absorber is taken into consideration, assuming $\mathbb{P}_c(x, y, z) \equiv \mathbb{P}_c(z)$. Assuming surface recombination is negligible compared to bulk recombination, \mathbb{P}_c can be approximated as:

$$\mathbb{P}_c(z) = \exp\left(-\frac{|z - t_A/2|}{L_D}\right), \quad (5.3)$$

where t_A is the absorber thickness and L_D is the diffusion length of the semiconductor.

The relation above is represented in Figure 5.1.

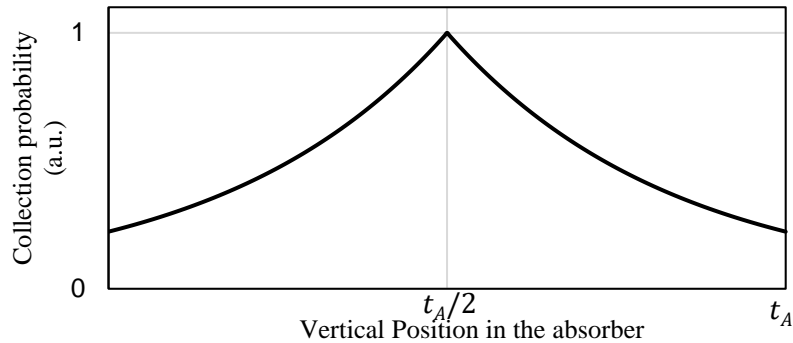


Figure 5.1. Variation of the collection probability in the absorber layer.

L_D is a critical material property for an effective carrier collection (equation (2.7)).

When L_D is much longer than the absorber thickness, all the generated carriers contribute the photocurrent, and IQE is equal to 1. Therefore, EQE solely depends on the absorption efficiency. However, this is generally not the case for most of the emerging technologies. For example, L_D is ~ 100 nm for amorphous silicon [212] which restricts the absorber thickness to the same order. On the other hand, determination of L_D of organic materials is not as straightforward due to bulk heterojunction (BHJ) structure of organic semiconductors. Although the individual values of L_D are known for donor and acceptor materials, it is complicated to calculate it for a heterojunction blend. Most of the organic materials have very short diffusion lengths (< 10 nm), which significantly limits the possibility of sufficient light absorption. Therefore, bulk heterojunction blend solar cells were proposed in order to limit the distance of all the locations to the donor-acceptor

interface to the diffusion length. Therefore, theoretical collection probability is 100% [213–215]. However, this is never the case in practical solar cells due to the microstructure or other internal effects which are out of the scope of the present study. In BHJ organic solar cells, it is better to use the term collection length (L_c) which is defined as the distance that an exciton can travel before reaching to the other layer. An empirical collection length can be found using the measurements in the literature [216–218]. The empirical collection length of the organic materials can be approximated around $L_{c,emp} \sim 100 \text{ nm}$.

In the case of planar solar cells, the charge generation can be assumed uniform in the z-direction. In this case, equation (5.1) simplifies to:

$$\eta_e = \frac{N_p}{N_i} \frac{2L_D}{t_A} (1 - e^{-t_A/2L_D}). \quad (5.4)$$

Note that EQE has two components: an optical component (η_A), which has a complicated tie to all geometry parameters and material choices and can only be determined via solving Maxwell's equations. The second component (η_I) is IQE and is only a function of the absorber height and the diffusion length in this simplified model. Generally, the expectation is that thicker silicon results in higher absorption, increasing recombination, resulting in lower electric factor. The trade-off between these two components is the key to optimal design. This trade-off is shown for a random fixation of all geometry parameters but varying absorber thickness in Figure 5.2.

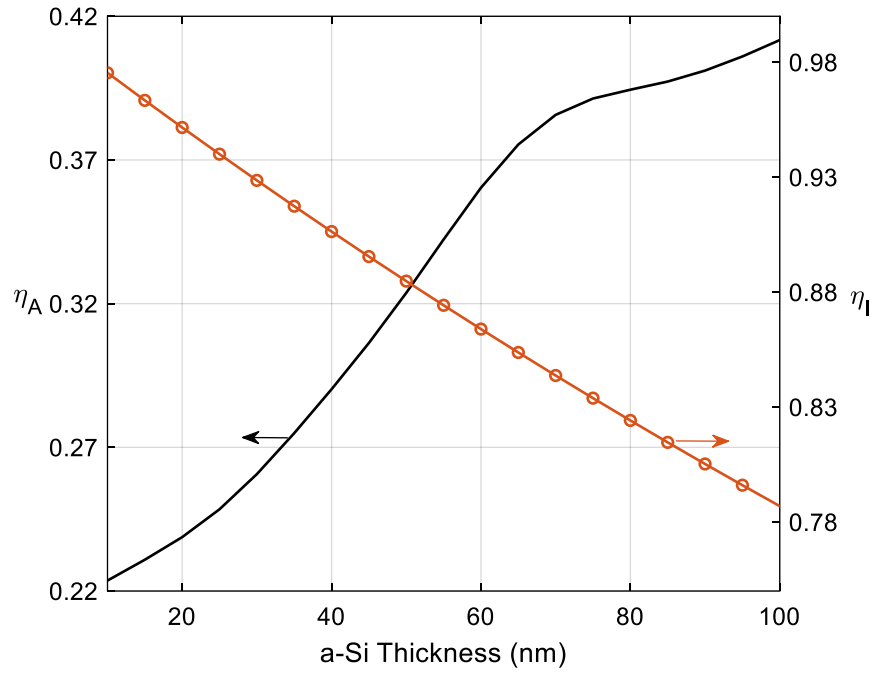


Figure 5.2. The variation of η_A and η_I with respect to the absorber layer thickness. The absorber is a-Si. Adapted from [171].

The proposed EQE model is validated with experimental results in the literature [60]. The authors measured EQE of an Ag/ZnO:Al/a-Si/ITO solar cell and calculated absorbed power in the a-Si layer using FDTD method. The same absorption profile is used to calculate EQE using equation (5.4) for $t_A = 100 \text{ nm}$ and $L_D = 100 \text{ nm}$. The comparison of experiments and present calculations based on absorptivity is given in Figure 5.3. Note that the model matches closely with the experiments for most of the relevant spectrum.

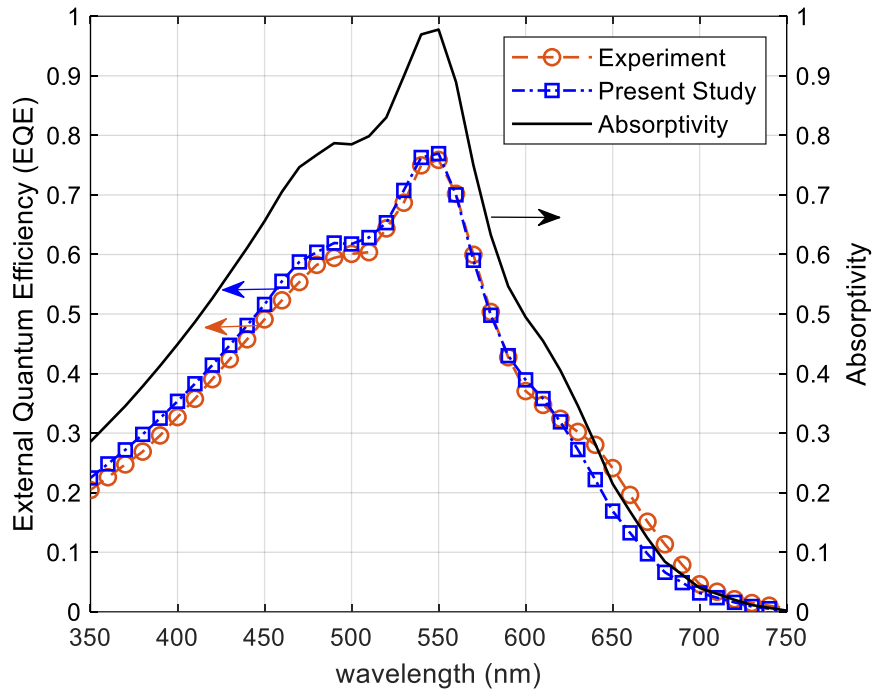


Figure 5.3. Comparison of measured and calculated *EQE* and simulated absorptivity profile for Ag/ZnO:Al/a-Si/ITO solar cell [60]. Adapted from [171].

5.2. Schematic of the Planar Solar Cell

The thin film solar cell structure in Figure 5.4 is considered in the present study. The amorphous silicon (a-Si) active layer is stacked between the aluminum back reflector and antireflective indium tin oxide (ITO) layers. The oxides Al_2O_3 and SiO_2 , formed during manufacturing, could help to improve solar cell performance by balancing the refractive indices between a-Si and the front/back layers [138,167]. Therefore, they are also included in the optimization.

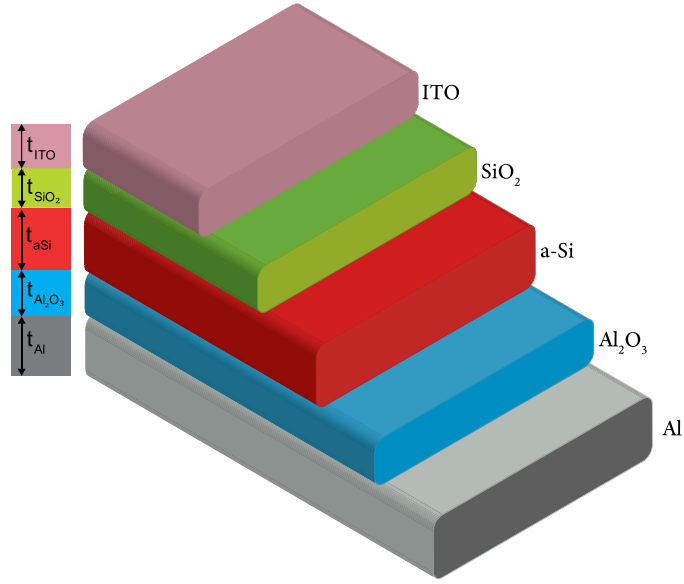


Figure 5.4. Thin film multilayer solar cell structure. Adapted from [171].

5.3. Optimization Problem

The aim of the present study is to maximize EQE given in equation (5.4) by modifying the solar cell geometry vector, \mathbf{x} :

$$\begin{aligned} \max_{\mathbf{x}} \eta_e(\mathbf{x}), \\ \mathbf{x}^L < \mathbf{x} < \mathbf{x}^U \end{aligned} \quad (5.5)$$

Similar to the surrogate modeling of the absorption enhancement factor in the previous section, the surrogate EQE becomes:

$$\hat{\eta}_e = \frac{\hat{N}_p}{N_i} \frac{2L_D}{t_A} (1 - e^{-t_A/2L_D}), \quad (5.6)$$

where \hat{N}_p is calculated with the surrogate absorptivity.

$$\hat{N}_p(\mathbf{x}) = \frac{1}{hc} \int \lambda \hat{\alpha}(\mathbf{x}, \lambda) I(\lambda) d\lambda. \quad (5.7)$$

5.4. Surrogate Model

A total of 1000 points are uniformly sampled from the input space, and the corresponding output values (absorptivity) are obtained from FDTD simulations. Lower and upper bounds are imposed on the input vector in order to restrict our focus to a reasonably limited range. These bounds are shown in Table 5.1.

NN architecture is 6- R_1 -1 where R_1 is the number of neurons in the hidden layer and is determined based on minimum validation error principle: Cross validation is used during training, and mean training and validation errors are calculated as the average of $n = 4$ folds. Optimal R_1 is where the validation error does not improve despite increasing R_1 . The results for the NN training are presented in Figure 5.5. The optimal R_1 is determined as 7 in this case (see Figure 5.5a). The final coefficient matrices are then obtained by training the NN with this configuration over the entire available data. The variation of Sum Square Error (SSE) during the final training is presented in Figure 5.5b. The trained model is then used as the surrogate for FDTD simulations in optimization, the results of which will be demonstrated in the next section.

Table 5.1. Upper (UB) and lower (LB) bounds for the multilayer solar cell. Adapted from [171].

Parameters	t_{ITO}	t_{SiO_2}	t_{aSi}	$t_{Al_2O_3}$	t_{Al}	λ
UB (nm)	20	5	20	5	20	300
LB (nm)	80	20	200	20	120	750

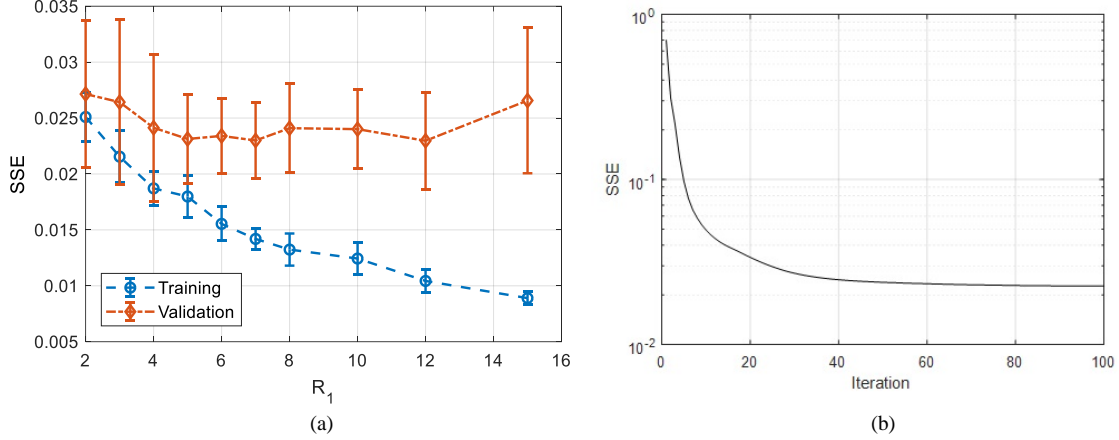


Figure 5.5. Neural network training. (a) Normalized mean sum of squared error (SSE) with respect to number of neurons in hidden layer (R_1), (b) Evolution of SSE cost function during final NN training. Adapted from [171].

5.5. Results and Discussion

The trained NN surrogate model is used instead of original FDTD simulations for designing the optimal structure. The search is done using two randomly selected starting points of $\mathbf{x}_{i,1} = [50,12,110,12,70]^T$ and $\mathbf{x}_{i,2} = [20,10,70,10,60]^T$. Every search includes a SA optimization followed by a local QN optimization starting at the optimal point of SA. Final optimization results are presented in Table 5.2 and compared with the previous study [167]. The reference [167] used a regression tree based optimizer and SA on direct FDTD simulations to find the optimal solution. However, since the objective function in [167] is slightly different than the present objective function, a deviation between the results of these two studies is expected. The present study achieved a marginally higher EQE than that in [167]. The evolution of EQE during the iterations for the results presented in Table 5.2 is shown in Figure 5.6.

Table 5.2. Results of optimization. Adapted from [171].

Solution	t_{ITO}	t_{SiO_2}	t_{aSi}	$t_{Al_2O_3}$	t_{Al}	η_e (NN)	η_e (FDTD)
1.NN-SA-QN	29	19	65	20	101	0.356	0.370
2.NN-SA-QN	29	20	65	20	98	0.356	0.369
Reference [167]	30	16	62	20	50	0.350	0.361

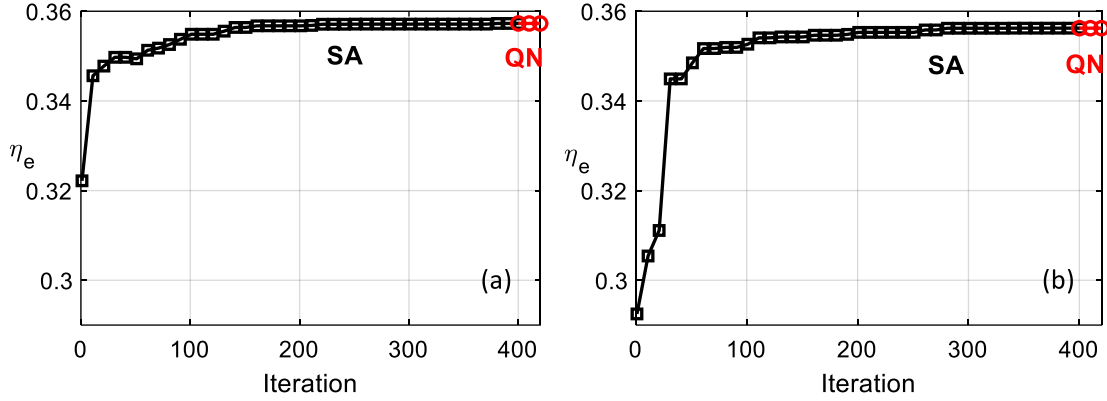


Figure 5.6. Evolution of surrogate EQE during optimizations with initial guesses (a) \mathbf{x}_1 , (b) \mathbf{x}_2 . Adapted from [171].

The absorptivity and EQE spectrum of the initial solution \mathbf{x}_1 and the one obtained by optimization starting from $\mathbf{x}_{i,1}$ are shown in Figure 5.7. Note that the majority of improvement is due to a wider absorption spectrum in the case of the optimal solution, especially at wavelengths shorter than 450 nm. The optimal solution has more than 25% improvement in efficiency, is more broadband, and has larger optical absorption despite a thinner silicon layer. The optimal solution also has 50% more EQE compared to optimal thickness bare silicon ($\sim 50\text{nm}$ [167]).

The (surrogate) spectral absorptivity of optimized geometry is also compared with the results from FDTD for the same geometry in Figure 5.8. Note that the profiles are in a

good agreement in most of the spectrum except $\lambda = 500 - 600$ nm which is the reason of the discrepancy between EQE values obtained by NN and FDTD.

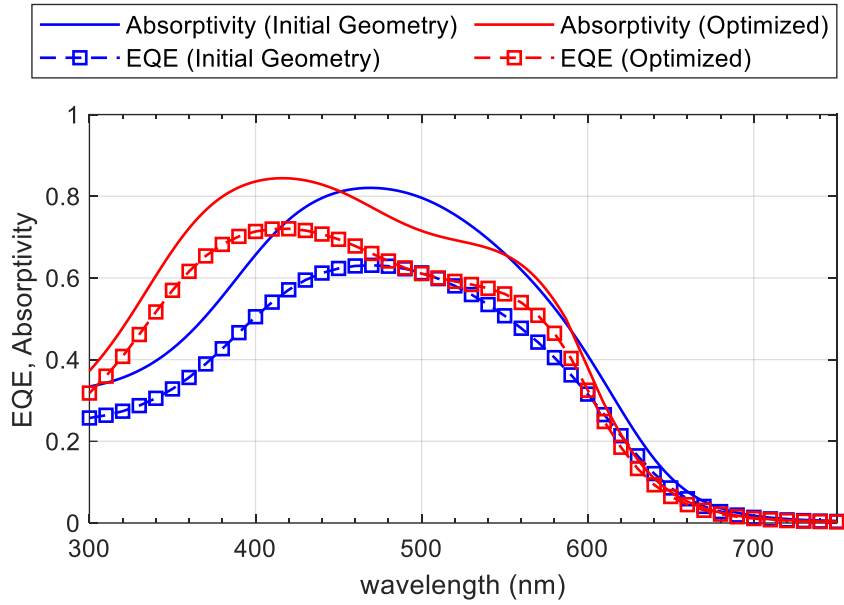


Figure 5.7. Absorptivity and EQE of initial ($\mathbf{x}_{i,1}$) and optimized geometries in Table 5.2. Adapted from [171].

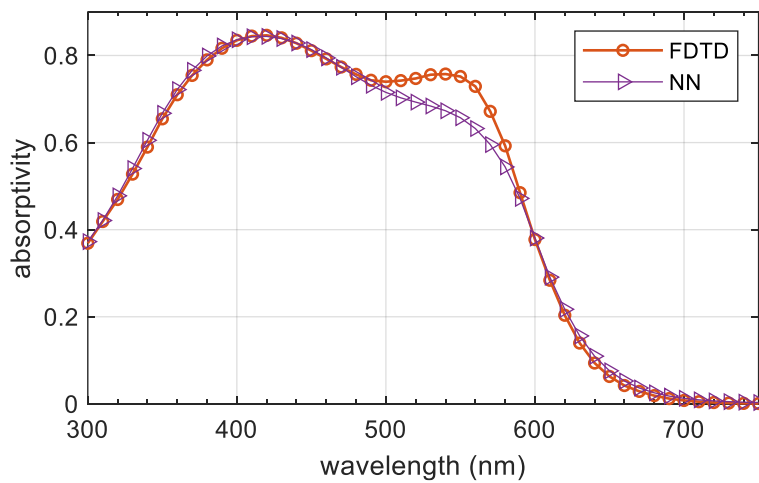


Figure 5.8. Absorptivity of optimized geometry obtained by NN and FDTD. Adapted from [171].

5.6. Computational Cost

Each SA algorithm is iterated 400 times, and the consequent QN takes several extra iterations. NN based SA-QN takes 30 seconds to find an optimal solution, which is negligible compared to the amount of time spent at finding the true EQE value for a given geometry using FDTD (~600 seconds). The overall number of computations is equivalent to only 20 full-spectrum FDTD calculations, which is impressively smaller than approximately 100 iterations in regression tree based search and 200-400 iterations in SA on direct FDTD calculations used in the reference study [167]. Therefore, the overall computation time is reduced by a factor of 5-20 using the proposed surrogate based optimization.

5.7. Conclusion

In this chapter, the optical absorptivity of a thin film multilayered a-Si solar cell is modeled accurately with NNs and efficiently approximated as a function of cell geometry and wavelength. Using this framework and the approximate external quantum efficiency of the cell as a function of absorptivity and electrical recombination factor, a multilayer thin film solar cell structure consisting of ITO front coating and metallic back reflectors and oxide layers is optimized for maximum efficiency. Our required computation time for an entire model fitting and optimization was 5 to 20 times faster than the optimization times of the best previous results, therefore proving the value of surrogate modeling. The final design suggests that a 50% improvement in the external quantum efficiency of silicon is achievable by designing simple multilayer front-back ITO/metallic and oxide coatings.

6. TRANSFER OPTIMIZATION OF THIN FILM SOLAR CELLS FOR MAXIMUM OPTOLECTRIC EFFICIENCY[‡]

In this study, a new method for design optimization is proposed based on *transfer learning*. The proposed framework improves the accuracy and efficiency of surrogate based optimization. When design specifications change, the objective function changes too. Therefore, there is a need for a new surrogate model. However, the concept of transfer learning can be used to refit the new surrogate more efficiently. In other words, insights from previous experiences can be used in learning and optimizing the new function.

In this chapter, two surrogate based transfer optimization methods are proposed for thin film solar cell design. The first one uses the neural network surrogates, and the second uses the Gaussian process surrogates. At least one optimization is assumed to have taken place (base case). The aim is to repeat optimization for a structure with different material combinations (transfer cases). The rest of this chapter is organized as follows: In Section 6.1, the optimization problem is presented with the details of the solar cell structure, material choices and the optimization problem formulation. In Section 6.2, the transfer learning concept is introduced. Section 6.3 and 6.4 are devoted to the neural network and Gaussian process based methods, respectively. In each section, the specific

[‡] Reprinted with permission from “Using a Novel Transfer Learning Method for Designing Thin Film Solar Cells with Enhanced Quantum Efficiencies” by M. Kaya and S. Hajimirza, 2019. Nature Scientific Reports, 9, 5034, Copyright 2019 by Springer Nature.

[‡] Reprinted with permission from “Using Bayesian Optimization with Knowledge Transfer for High Computational Cost Design: A Case Study in Photovoltaics” by M. Kaya and S. Hajimirza, 2019. Proceedings of ASME 2019 International Design Engineering Technical Conferences and Computers and Information in Engineering Conference, Copyright 2019 by ASME.

details of the methodology are explained, and the results are presented and discussed. Finally, this chapter is concluded in Section 6.5.

6.1. Multilayer Thin Film Solar Cell Optimization

The solar cell design optimized in this chapter is very similar to the one in Figure 5.4. The solar cell structure is presented in Figure 6.1 in a more general sense indicating the functions of the individual layers.

In the previous sections, the importance of solar cell geometry is emphasized. In addition to the dimensions, the choice of materials used in the solar cell layers can dramatically affect the optical and electrical properties. On the other hand, when the material choices are included as a design variable, the optimization problem becomes mixed-integer programming, which is known to be computationally costly. Furthermore, for the present problem where the optimizations are done one by one, the optimization study should be repeated $(m_1 \times m_2 \times \dots \times m_d)$ times for all possible material combinations where d is the input space dimension and m_j ($1 \leq j \leq d$) is the number of choices for the j^{th} input. In this case, knowledge transfer between different material combination tasks is worthwhile, as similar geometries with different material combinations can have similar optoelectrical responses. In general, the initial assumption is that source and target domains are similar [201]. Sometimes, the false similarity assumption can cause negative transfer and hurt the learning [219]. Therefore the similarity assumption must be monitored and evaluated carefully.

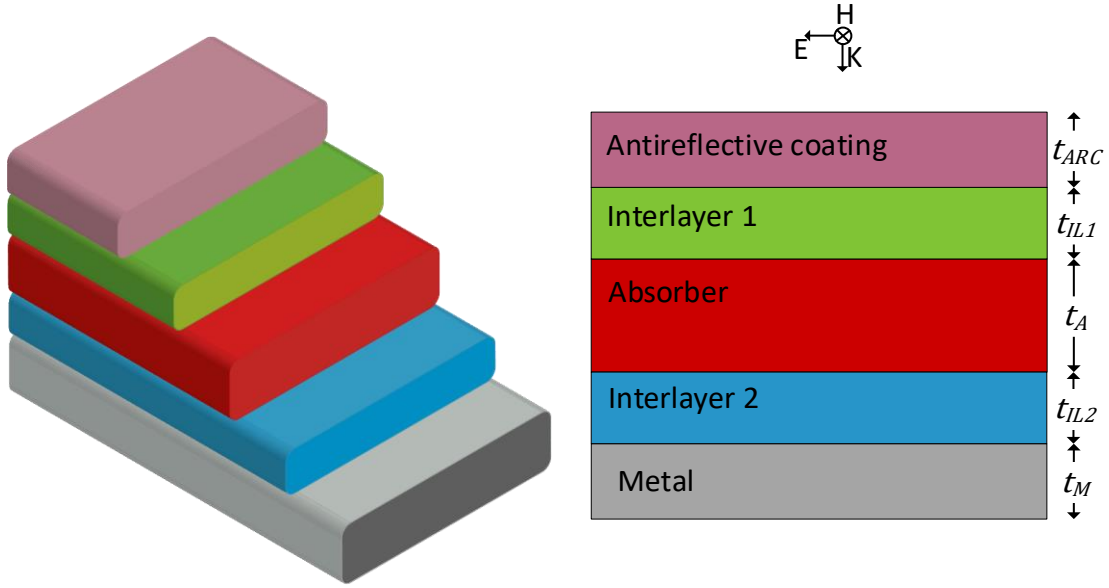


Figure 6.1. Multilayer solar cell.

Once an optimization study is carried out for a base case, the transfer optimization can be used to optimize a solar cell structure with the same geometry but different materials. For example, once we optimize an ITO/ZnO/P3HT:PCBM/MoO₃/Al solar cell structure as a base case, less effort should be necessary to optimize a five layer solar cell consisting of different materials. For this purpose, a base case and transfer cases are selected as follows:

$$\begin{aligned}
 \mathbf{x}_B &= [t_{ITO}, t_{ZnO}, t_{P3HT:PCBM}, t_{MoO_3}, t_{Al}]^T \\
 \mathbf{x}_{TL-1} &= [t_{ITO}, t_{SiO_2}, t_{aSi}, t_{Al_2O_3}, t_{Al}]^T \\
 \mathbf{x}_{TL-2} &= [t_{Si_3N_4}, t_{PEDOT:PSS}, t_{PCPDTBT:PCBM}, t_{Al_2O_3}, t_{Al}]^T
 \end{aligned} \tag{6.1}$$

These materials are widely used in thin film solar cells. TL-1 case is optimized in chapter 5 without transfer optimization. TL-2 is optimized for the first time. The optimization problem solved in this study is given as the same as the previous chapter:

$$\max_{\mathbf{x}} \eta(\mathbf{x}), \quad (6.2)$$

$$\mathbf{x}^L < \mathbf{x} < \mathbf{x}^U.$$

6.2. Transfer Learning

The transfer learning method consists of a base surrogate model and a transfer learning framework to share the gained knowledge. The response of the surrogate model can be expressed as:

$$F(\mathbf{x}) = \mathbf{y}_t + \varepsilon, \quad (6.3)$$

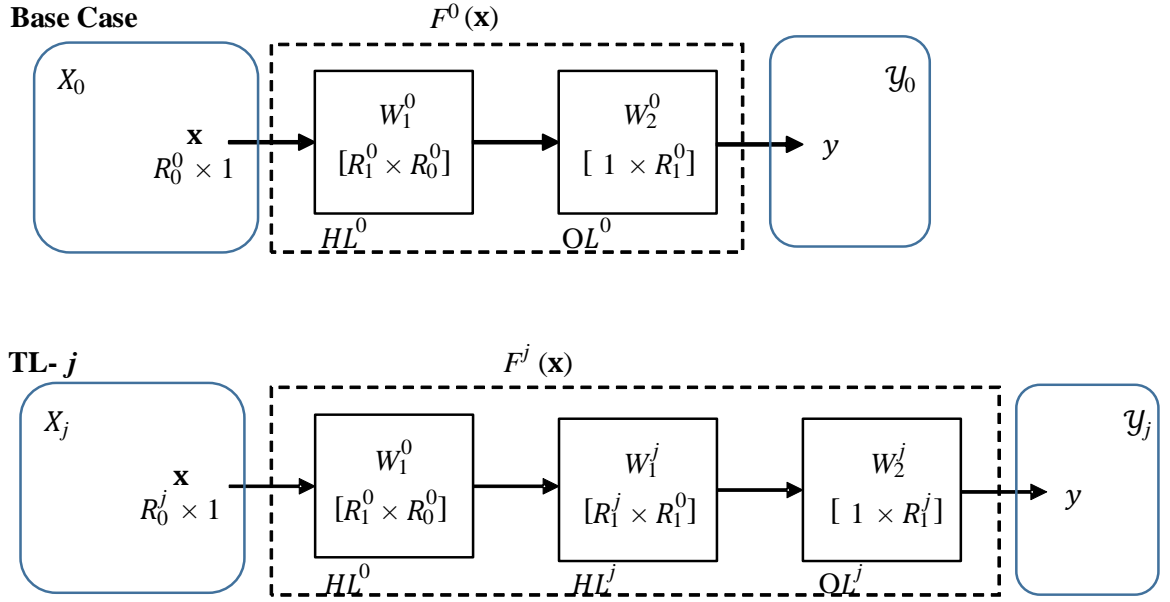
where $\mathbf{y}_t \in \mathcal{Y}$ is the target output, $F(\mathbf{x})$ is the objective function approximation at $\mathbf{x} \in \mathcal{X}$ and ε is the error between the target and the predicted outputs. F is obtained by an iterative training procedure similar to the previous sections. As a result of the training, coefficients of the predefined metamodel (e.g., hyperparameters of neural networks and Gaussian process) are obtained.

Depending on the similarity between the input-output spaces, the knowledge can be transferred from one domain (*source*) to another (*target*). This transfer can be achieved in many ways depending on the metamodel. Knowledge transfer using Gaussian Processes, for instance, can be achieved by learning a joint probability distribution and defining a common response surface [184]. Knowledge transfer in neural networks was previously recommended via shared layers [220]. NN and GP surrogates are used in the first and the second parts of this chapter, respectively.

6.3. Transfer Optimization of Thin Film Solar Cells Using Neural Networks

6.3.1. Methodology

Neural networks are one of the most ideal tools for surrogate model building in complex tasks particularly for knowledge transfer, due to excellent prediction performance and the ability to handle high dimensional and highly nonlinear data [159]. The knowledge in neural networks can be transferred via borrowing hidden layers. One hidden layer of the previously trained network is borrowed as an intermediate layer. The dimensions of the new hidden layer then become $R_1^0 \times R_1^1$ where superscripts 0 and 1 refer to the base case and the first transfer learning sequence. Therefore the input space is transformed into another space through the previous knowledge. This method is shown in Figure 6.2. The dimensions of the input and output spaces can be the same or different. In the case of different dimensions, knowledge is transferred between the matching features, and the rest is treated as usual. Thus, the method reduces to a dimensionality reduction approach, and the accuracy of the new predictions is expected to be improved due to the similarity between the subspaces in the two different input spaces.



HL^j : hidden layer and OL^j : output layer of j th transfer learning sequence.
 $j=0$ for traditional machine learning (base case)

Figure 6.2. Schematic of neural network with transfer learning for a single output.
 Adapted from [203].

The output of a two layer feed forward neural network is calculated from:

$$y = F^0(\mathbf{x}) = f_2^0(W_2^0 f_1^0(W_1^0 \mathbf{x})), \quad (6.4)$$

where W_1^0 and W_2^0 are the coefficient matrices of the base case NN found from iterative training. $f_j(\cdot)$ is the functional operation at the j^{th} layer, such as sigmoid and linear function. The knowledge transfer is then accomplished by transferring the hidden layer of the base case to the new case, expressed as:

$$y = F^1(\mathbf{x}) = f_2^1(W_2^1 f_1^1(W_1^1 f_1^0(W_1^0 \mathbf{x}))), \quad (6.5)$$

where W_1^0 is transferred from the base case. Training of the new case is done to find W_1^1 and W_2^1 . When another case is to be optimized in the same manner, the same procedure can be repeated, or the trained layer of the new case can be transferred. One drawback of the proposed method is the increase in the number of coefficients of the neural network if $R_1^0 > R_0^1$ the new number of coefficients to train increases from $R_1^1(R_0^1 + 1)$ to $R_1^1(R_1^0 + 1)$, which may result in overfitting [221].

The surrogate based optimization procedure starts with the DOE [147]. Then, the outputs of the forward problem are evaluated at the sampled points using the simulation tool. The input/output pairs constitute the training set, which is then fed to the NN trainer. For optimization, simulated annealing [117] is used to optimize the surrogate objective function. The details of these methods can be found in chapter 3.

The performance of a predictive model can be quantified, considering the validation set. The most common performance metric is the mean squared error defined as:

$$MSE = \frac{1}{N_j} \sum_{i=1}^{N_j} \varepsilon_i^2, \quad (6.6)$$

where N is the number of data, $j = T, V$ for training and validation sets, respectively. ε_i is the error between real and approximate output for i^{th} instance.

As shown in Figure 6.2, the base case is optimized by using traditional surrogate based optimization methods. Then the hidden layer of the trained model is transferred to other cases.

6.3.2. Results and Discussion

6.3.2.1. Base Case

The training of the base case is done using 1,000 data points with 750 of them used as the training set and the rest for validation. The number of neurons in the hidden layer is determined based on the principle of minimum validation error as follows: The in-sample and out-sample errors are recorded as the number of neurons in the hidden layer is increased. The network configuration providing the minimum out-sample error is selected for the optimization. This procedure is repeated 10 times to eliminate the possibility of the training algorithm being trapped in local optima. Optimization is also repeated 10 times using all NN models obtained. This results in 10 possible optimal points. These points are run through the high-fidelity (FDTD) model, and the highest function value is selected accordingly. The number of neurons in the hidden layer for the base case is selected as 12 based on the results in Figure 6.3a. Then the optimization is done using the NN models with 12 neurons using all the generated models. Full-fidelity optimization is also done using the software in order to validate the results (See Table 6.1). The optimized values are in good agreement with a maximum 5% error. The evolution of EQE during surrogate based optimization iterations is presented in Figure 6.3b. Note that the best reported EQE in Table 6.1 is obtained using simulations, so discrepancies between this value and that of Figure 6.3b are expected.

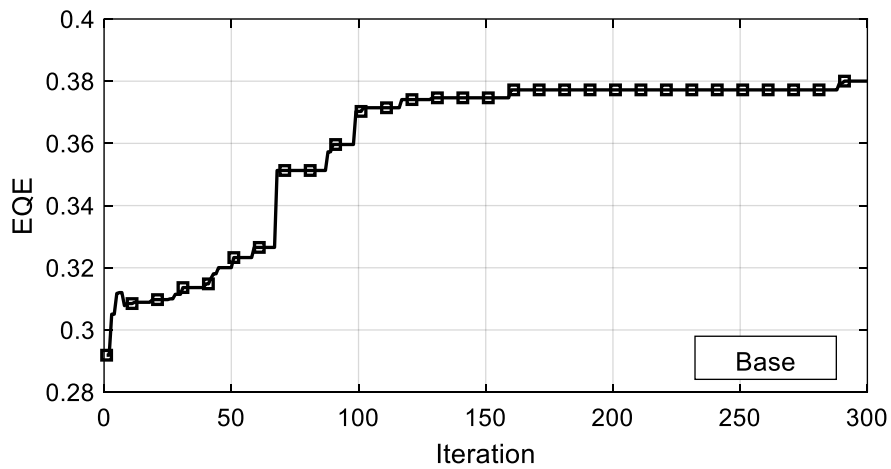
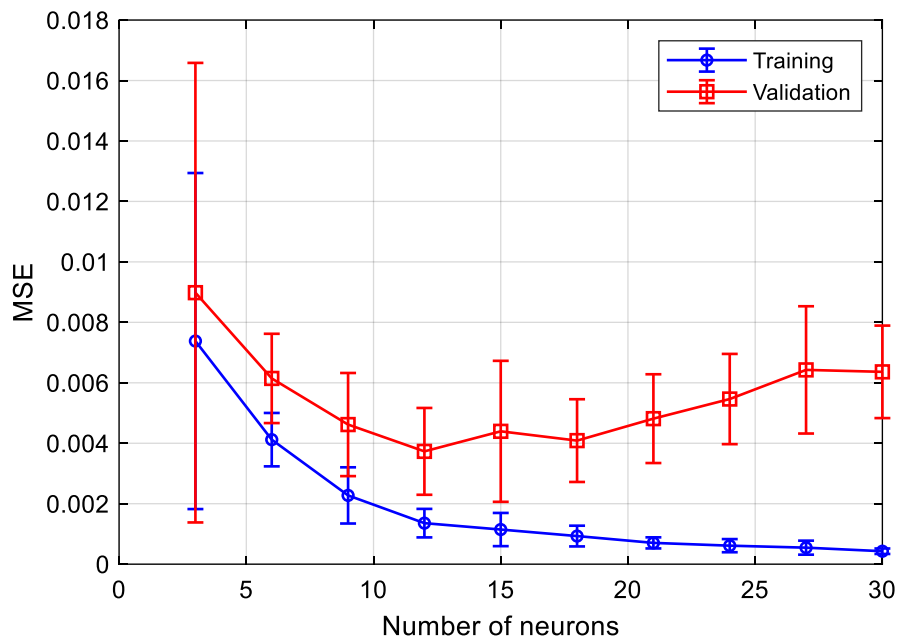
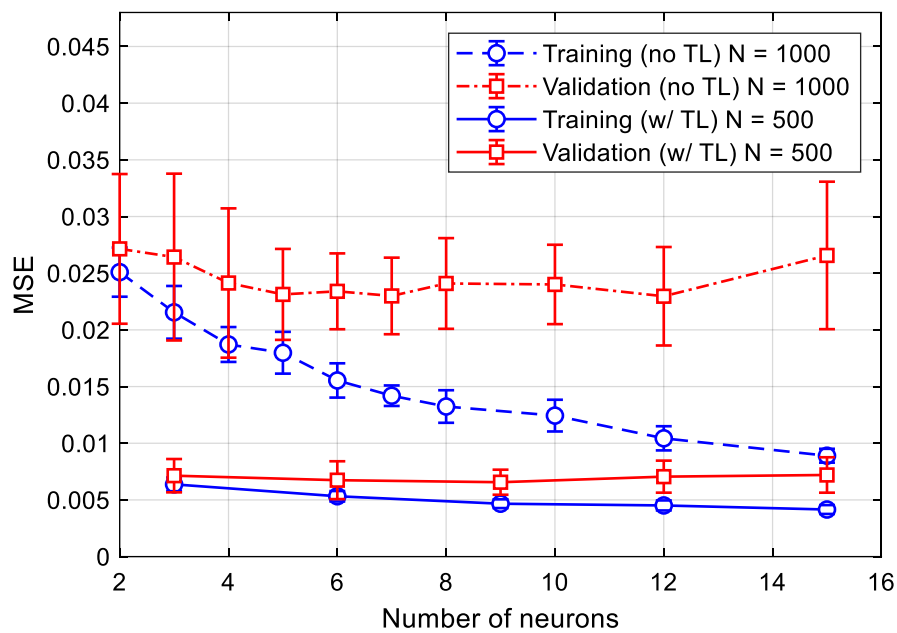


Figure 6.3. (a) Variation of mean squared error for training and validation data sets with respect to the number of neurons in the hidden layer of NN for base case, (b) Evolution of EQE during optimization for the base case. Adapted from [203].

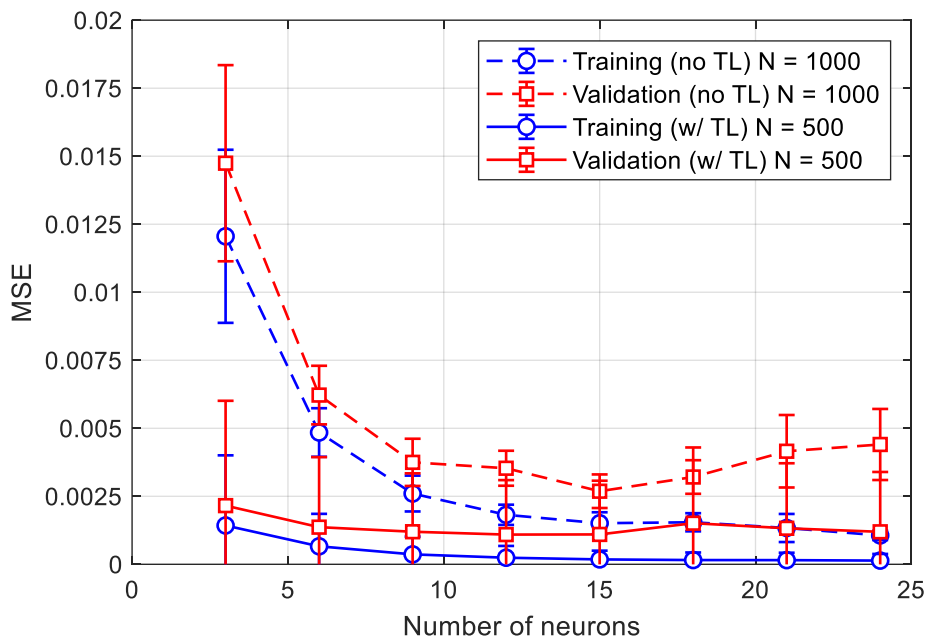
6.3.2.2. Transfer Cases

In order to demonstrate the proposed approach, two material sets different from the base case are considered for transfer optimization. These sets are represented by vectors $\mathbf{x}_{\text{TL-1}}$ and $\mathbf{x}_{\text{TL-2}}$. First, the same steps as in the base case are followed without the transfer learning framework as a comparison. In these cases, 1000 data points are used with 4 folds for cross validation. Then training is repeated for the transfer learning cases using equation (6.5) with 500 new data points. The prediction performances using transfer learning are presented and compared with the traditional method in Figure 6.4a and b.

Figure 6.4 shows the effectiveness of the transfer learning method. The smallest out-sample MSE of no TL case in TL-1 is more than 3 times larger than the largest out-sample MSE w/ TL case even though the number of data is half of the no TL case. Furthermore, although the improvement in TL-2 case is not as significant as in TL-1, using the transfer layer reduces the error to almost half of the TL-2 (no TL). The reason for this less significant improvement is that the validation error of TL-2 case without the transfer layer is similar to that of the base case. On the other hand, the validation error of TL-1 (no TL) case is ~ 5 times larger than that of the base case. As shown in Figure 6.4b, the most significant improvement in validation error is obtained when 3 neurons are used where the largest deviation between errors of TL-2 and base cases is observed. Therefore the relation between the deviation between errors of transfer and base cases suggests that the more accurate the base case is, the more the validation error is reduced. Furthermore, if the base case is less accurate than the transfer cases, prediction performance can worsen. This is known as the negative transfer, which is an undesirable phenomenon in transfer learning.



(a)



(b)

Figure 6.4. Results for (a) TL-1 (ITO-SiO₂-aSi-Al₂O₃-Al) and (b) TL-2 (Si₃N₄-PEDOT:PSS-PCPDTBT:PCBM-Al₂O₃-Al) without transfer layer (no TL, dashed lines) using 1000 data and with transfer layer (w/TL, solid lines) using 500 data. Adapted from [203].

The effect of the negative transfer on prediction accuracy is illustrated in Figure 6.5 by switching the base and TL-1 cases where the hidden layer of TL-1 (ITO-SiO₂-aSi-Al₂O₃-Al) is transferred to the base case (ITO-ZnO-P3HT:PCBM-MoO₃-Al). As seen from Figure 6.5, the training MSE does not change as expected; however, the validation error significantly increases since the transferred layer is adopted from a less accurate model. Therefore, the similarity between the cases should be known for improvement. In TL-1 case, 12 and 9 neurons are selected for no TL and w/ TL, respectively, for optimization. The results are compared with the previous optimization studies for the same 5-layer a-Si solar cell in chapter 5 and reference [167]. Similarly, in TL-2 case, 15 and 12 neurons are selected for no TL and w/TL, respectively for optimization.

The results obtained using transfer learning are in good agreement with the direct optimization results for both cases. The optimized geometry in TL-1 case is also very close to the results from chapter 5. In the other study [167], a regression tree based optimizer is used as well as simulated annealing on direct FDTD simulations to find the optimal solution. However, since the objective function in this study is slightly different from the present objective function, a deviation between the results of these two studies is expected. The present study achieved a marginally higher EQE than the previous findings [167]. The optimization results are presented in Table 6.1, and evolutions of EQE are shown in Figure 6.6 and Figure 6.7.

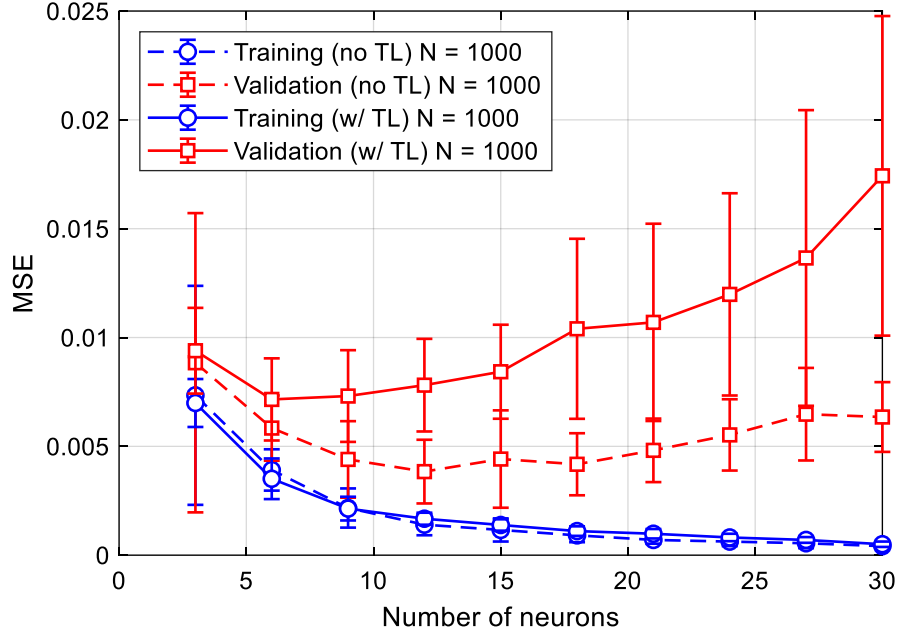


Figure 6.5. Negative Transfer: Comparison of MSE of no TL Base case (dashed) and w/ TL from TL-1 (solid). Adapted from [203].

Table 6.1. Optimization results for Base, TL-1 and TL-2 cases. Adapted from [203].

Case Name	N_{sims} [-]	t_{ARC} [nm]	t_{IL1} [nm]	t_A [nm]	t_{IL2} [nm]	t_M [nm]	EQE [-]
Base – NN based	1,000	76	19	79	12	100	0.370
Base - Direct	6,900	77	20	80	10	95	0.371
TL-1 – NN based – w/TL	500	31	20	65	20	102	0.371
TL-1 – NN based – no TL	1,000	29	19	65	20	101	0.370
TL-1 – Direct	9,200	30	19	65	20	103	0.372
TL-1 – Reference [167]	4,600	30	16	62	20	50	0.361
TL-2 – NN based – w/TL	500	40	5	98	5	95	0.355
TL-2 – NN based – no TL	1,000	38	7	95	5	100	0.352
TL-2 – Direct	5,520	42	5	100	5	97	0.360

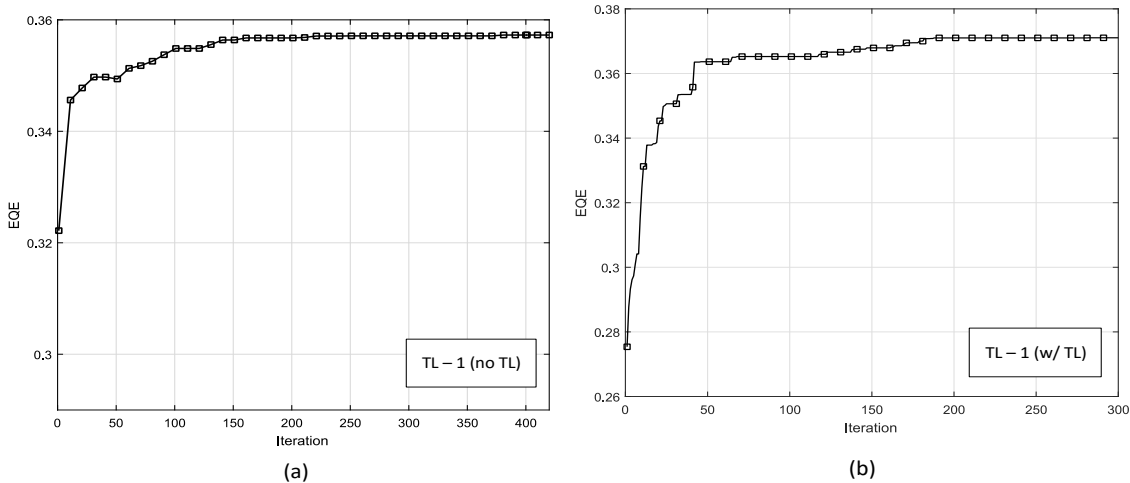


Figure 6.6. Evolution of EQE during optimization for (a) TL-1, w/out TL, (b) TL-1 w/ TL. Adapted from [203].

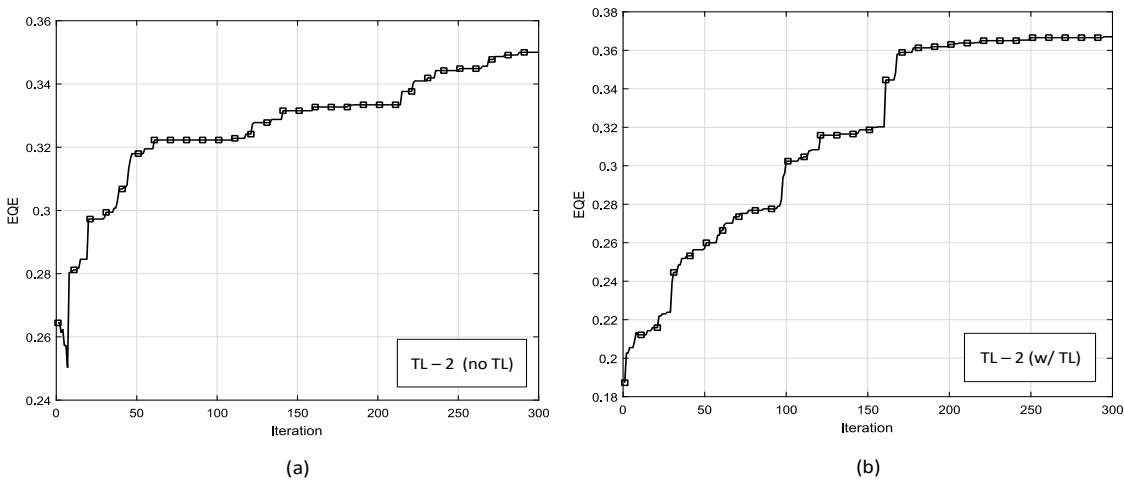


Figure 6.7. Evolution of EQE during optimization for (a) TL-2, w/out TL, (b) TL-2 w/ TL. Adapted from [203].

Results show that equivalent EQEs can be obtained from an amorphous silicon and an organic P3HT:PCBM solar cell. EQE of PCPDTBT:PCBM solar cell is lower than the others because the longer wavelengths where PCPDTBT:PCBM can absorb more than a-

Si and P3HT:PCBM are ignored in EQE calculation. EQE is calculated between $\lambda = 300 - 750$ nm for all cases for consistency.

6.4. Transfer Optimization of Thin Film Solar Cells Using Gaussian Process and Bayesian Optimization

The knowledge transfer in Gaussian process can be achieved using several ways. One solution to transfer knowledge from experiences to the current task is to assume a joint probabilistic model and use a product covariance function [184,222]. Another approach is to assume a common response surface [197,222]:

$$\tilde{y} = \frac{y - \mu_{common}}{\sigma_{common}} \quad (6.7)$$

6.4.1. Similarity Metric

The common response surface approach can be generalized between different design spaces by considering rank correlations between data, such as Spearman rank correlation coefficient. At each transfer, we can rank the previous tasks according to their correlations with the new one, and transfer can be made between more similar tasks. For example, the following weighted average can be used to obtain a common mean and a standard deviation:

$$\begin{aligned} \mu_{common} &= \frac{\sum_{k=1}^K w_k N_k \mu_k}{\sum_{k=1}^K w_k N_k}, \\ \sigma_{common}^2 &= \frac{\sum_{k=1}^K (w_k N_k)^2 \sigma_k^2}{\sum_{k=1}^K (w_k N_k)^2}, \end{aligned} \quad (6.8)$$

where w_k is the weight which is a function of similarity among the current task and the task knowledge is transferred from. This similarity can be calculated by the deviation of the responses of the current task (y) and the k th previous task (y_k) to the same input set (X_{init}). The similarity $\varphi(y, y_k)$ can be calculated as ($1 - deviation$):

$$\varphi(y, y_k) = 1 - \frac{1}{C} \sqrt{\frac{1}{n} \sum_{i=1}^n (y_i - y_{k,i})^2} \quad (6.9)$$

where n is the size of the initial sample. C is the normalization constant, representing the maximum possible deviation. In the extreme case, $y = 0$ and $y_k = 1$ (or vice-versa), which translates to a deviation of 1, thus $C = 1$. However, C can be selected according to the desired allowable deviation. Additionally, it is safer to transfer knowledge from the tasks with high similarity by establishing a threshold to prevent the initial sample from being misleading. Therefore, the weight can be calculated using the similarity metric and a predefined threshold:

$$w_k = \begin{cases} \varphi(y, y_k) & \varphi(y, y_k) > 0.5 \\ 0, & \varphi(y, y_k) < 0.5 \end{cases} \quad (6.10)$$

6.4.2. Gaussian Quadrature Integration

The use of Gaussian Process is not limited to optimization problems but can be helpful in many areas where uncertainty information is needed. For example, the computation of the integral in equation (2.3) requires evaluating the function many times for only one optimization iteration. This method is similar to sigma-points methods [223] and relies on evaluating the objective function only where most contributions are made.

As the uncertainty of the predictions can be obtained in GP predictions, evaluating functions only at high uncertainties will result in an exploration based numerical integration framework. The GP based integration procedure is explained in Table 6.2.

Table 6.2. GP based numerical integration. Adapted from [204].

Evaluate $I = \int_{x_1}^{x_2} y(x) dx$

Input:
 n : initial number of sampling points,
 δ : convergence criterion,
 $N_{iter,max}$: maximum allowed iterations.

1. Sample n initial points: $\mathbf{x}_{1:n}^0 \sim \mathcal{U}(x_1, x_2)$.
2. Evaluate the initial points: $y^0 = y(\mathbf{x}^0)$
3. Fit a $\mathcal{GP}(\mathbf{x}^0, y^0)$
4. Set $\mathbf{x} = \mathbf{x}^0, y = y^0, t = 0$

Until terminate do:

5. Calculate the numerical integral using trapezoidal rule: $I_t = trapz(\mathbf{x}, y)$
6. Find k s.t. $x^{new} = \arg \max_{\chi} |I_{pred} - I_t|$ where

$$I_{pred} = trapz([\mathbf{x}; \chi], [\mathbf{y}; \mu_y(\chi)]) \mu_y(\mathbf{x}^{test}), \sigma_y^2(\mathbf{x}^{test}) \sim \mathcal{GP}(\chi | \mathbf{x}, y)$$
7. Sample the new point: $x_{new} = \chi$ and calculate $y_{new} = y(\chi)$
8. Set $\mathbf{x} = [\mathbf{x}, x_{new}]^T$ and $\mathbf{y} = [\mathbf{y}, y_{new}]^T$
9. $t = t + 1$
10. Terminate if $\frac{(I_t - I_{t-1})}{I_{t-1}} < \delta$ or $t > N_{iter,max}$. Else go to step 5.

6.4.3. Optimization Procedure

Bayesian optimization [224] is a global optimization method that searches for the optimum point of a function by using a surrogate, i.e., Gaussian Process. The most important feature of this method is to use the exploration and exploitation of the design space. Therefore a suitable surrogate must provide accurate point estimates as well as

uncertainty in the new predictions. Surrogate functions can be selected from a wide range of possibilities, and Gaussian Process is one of the most widely used methods in the Bayesian optimization framework. Bayesian optimization targets an acquisition function instead of the original objective. There is a variety of acquisition functions such as the probability of improvement, entropy search, upper confidence bound (*UCB*) and the expected improvement (*EI*). Specifically, *UCB* is calculated as follows:

$$UCB(\mathbf{x}) = \mu_y(\mathbf{x}) + \kappa \sigma_y(\mathbf{x}) \quad (6.11)$$

where $\mu_y(\mathbf{x})$ and $\sigma_y(\mathbf{x})$ are the mean and standard deviation of prediction at input \mathbf{x} determined by using Gaussian Process regression. κ is the exploration-exploitation tradeoff parameter. In this study, κ is taken 2.

As mentioned earlier, at least one optimization is assumed to be already performed (task 0). When we move to a new task, the similarity of the tasks is first evaluated on a small representative batch of data using equation (6.9). This initial batch is selected as the first n iterations of task 0 so that we make the comparison without spending extra computation. Moreover, this initial batch can also be used for constructing the first GP model. Then the first point which maximizes the objective function is found, and the GP is updated. The cycle of sampling, evaluation, and objective function maximization continues until convergence. In GP models, Matern 5/2 kernel is preferred. In this study, the infinite-metric GP optimization (IMGPO) algorithm developed by Kawaguchi et al. [225] is used.

The materials used in different layers of the solar cells in different tasks are presented in equation (6.1).

6.4.4. Results and Discussion

In this section, the optimization results are presented. The similarity metrics among the tasks are shown in Figure 6.8. The similarity is quantified by the metric in equation (6.9). Furthermore, Pearson (r) and Spearman (ρ) correlation coefficients are calculated as reference. These coefficients are commonly used to determine correlations among different data sets. As can be seen from the plots and numerical values of r and ρ , there are strong correlations among almost all of the tasks. However, a strong linear relation can be a weak estimator of similarity as it only shows the increase/decrease with the same change in the inputs. Therefore, the similarity metric is formulated to determine the effect of deviation between the tasks. The numerical values translate to the weights when calculating the mean and standard deviation of the common surface.

The results of the optimizations are shown in Table 6.3. Optimal geometry vectors from Bayesian optimization with and without transfer learning are presented. Furthermore, the spectral absorptivity profiles of the optimized designs are presented in Figure 6.9. Note that the black lines are the results of the direct optimizations presented as references. The results of the optimizations show that the final absorptivity profiles are consistent with the direct optimization results.

In all of the cases, direct optimizations were carried out using a heuristic optimization method, i.e., simulated annealing without approximation methods. Furthermore, it can be seen in Figure 6.9 that GPBO could reach the final absorption profiles close to the ground truth. After GPBO optimizations were performed without transfer learning, the information in Task 0 is transferred to Task 1 and information in

Tasks 0 and 1 are transferred to Task 2. The evolution of EQE values during optimizations are also presented in Figure 6.10. One of the conclusions from these results is that transfer learning reduces the time of optimization by leading the predictions for the function value improvements to better subspaces in the design space.

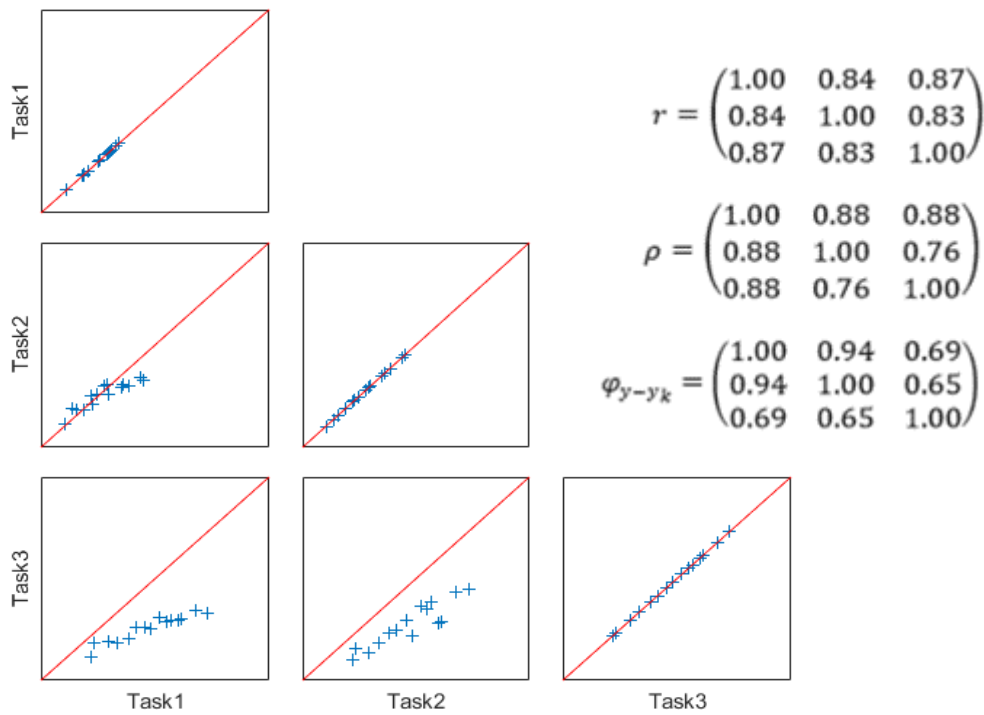


Figure 6.8. Comparison of the responses of the tasks given the same input set with the similarity metric (φ), pearson (r) and spearman (ρ) correlation coefficients. Adapted from [204].

Table 6.3. Results of optimizations. Adapted from [204].

Task	t_{ARC}^*	t_{IL1}^*	t_A^*	t_{IL2}^*	t_M^*	EQE^*
0 no TL	82	15	78	12	108	0.367
1 no TL	26	17	64	26	99	0.368
1 w/ TL	28	20	66	22	102	0.371
2 no TL	40	8	92	8	110	0.355
2 w/ TL	38	12	96	5	100	0.357

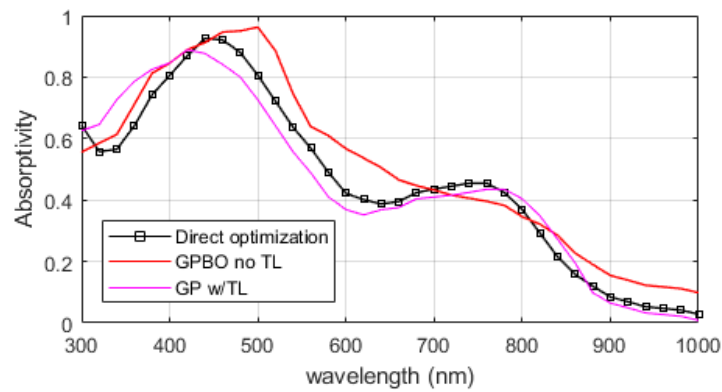
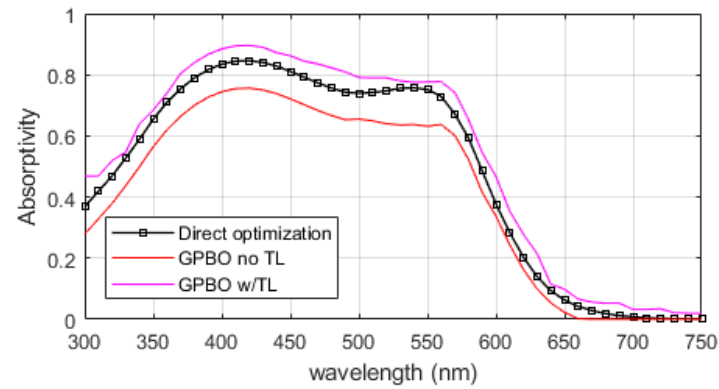
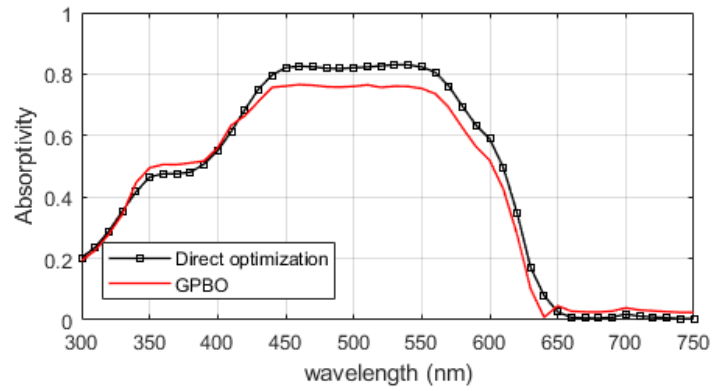


Figure 6.9. Top: Absorptivity profiles of the 0th task (base) for optimized geometries using direct optimization and GPBO. Middle and Bottom: Absorptivity profiles of the 1st task (Middle), 2nd task (Bottom) for optimized geometries using direct optimization and GPBO without (no TL) and with transfer learning (w/ TL). Adapted from [204].

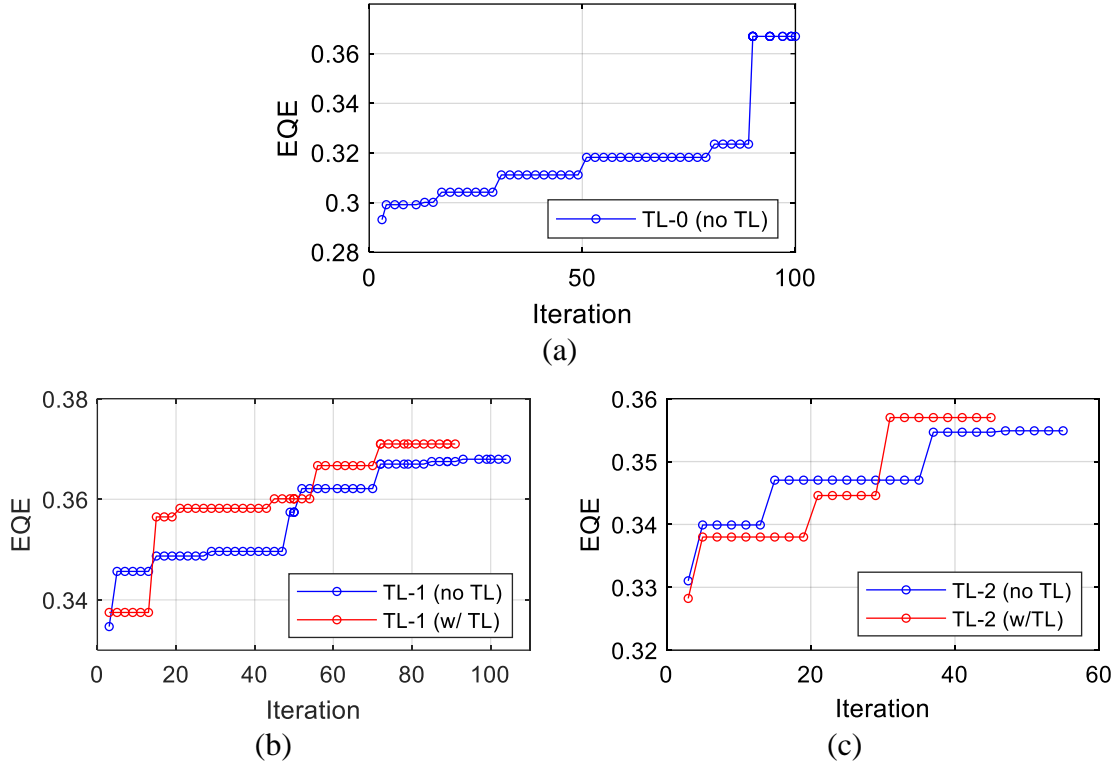


Figure 6.10. Evolution of the EQE during optimization of (a) Task 0 without TL. (b) Task 1 without and with TL. (c) Task 2 without and with TL. Adapted from [204].

The similarity of these cases is mostly originated from the spectral behavior of the absorber materials. Although the materials used in this study are not chemically similar, they share some common characteristics. For example, all three materials show peak absorptivity in the visible region. Furthermore, P3HT:PCBM of Task 0 and amorphous silicon of Task 1 have similar band gaps so that the absorption approaches zero at similar wavelengths. These similarities can be observed in the similarity metric.

6.5. Conclusion

In this chapter, two transfer learning based design optimization methods are presented. The proposed method is applied to a case study where a multilayer thin film solar cell is to be optimized for the best EQE. The first method utilizes neural network surrogates, where knowledge is transferred via hidden layers of NNs. The second method uses Bayesian optimization using Gaussian Processes. Knowledge transfer was modeled through a common response surface where mean and standard deviations from the previous optimizations are used to increase the accuracy of the Gaussian Process predictions and, consequently, the speed of the optimization.

The NN based transfer optimization is more time efficient than the GPBO due to their differences in handling the wavelength. Since NN uses wavelength as one of the inputs, integral operations do not require many simulations. However, GPBO utilizes a sequential approach for sampling since the surrogate is updated after every optimization iteration, increasing the number of simulations compared to NN.

7. SHAPE OPTIMIZATION OF NANOPARTICLES FOR MAXIMUM SCATTERING

The design procedure always relies on intuition from the user because of the parametrization requirement. In contrast to most of the design approaches in the literature, topology optimization can provide intuition-free and nonparametric design platforms in which no prior assumptions are made about the shape of the structure. Topology optimization is a framework for exploring material distribution in a domain for a given design objective. The concept was first proposed for structural mechanics problems [226,227], such as bridge and truss designs. It has also been used within different disciplines in the last decades, such as fluid dynamics and microelectromechanical systems. Topology optimization has also been used in photonics problems for desired optical properties [124,228–230].

Nonetheless, in none of these mentioned studies, the physical mechanism leading to the optical enhancements was targeted directly. In this chapter, a theoretical framework for designing complex plasmonic nanoparticles yielding maximum scattering is presented using topology optimization. Silver is used as the particle material throughout this study due to its high scattering and low loss (parasitic absorption) compared to other common metals [70]. The rest of this chapter is organized as follows: first, the problem is described, and computational modeling is detailed in Section 7.1. Then, in Sections 7.2 and 7.3, the optimization procedure and post processing steps are explained. In Section 7.4, the results are presented and discussed. The key results of this chapter are summarized in the last section.

7.1. Physical Model Description

The study aims to find the optimal shape of a nanoparticle within a given domain \mathcal{D} resulting in maximum scattering. The study objective and the schematics of the problem are presented in Figure 7.1. The gray region in Figure 7.1a is the solution domain where the incident light is absorbed and scattered. Two and three dimensional views of a hypothetical nanoparticle are illustrated in Figure 7.1b and c, respectively. Particle shape is defined by a density function, $\rho(\mathbf{x})$ (Figure 7.1b) which represents discretized elements corresponding to a design variable with possible values of 0 or 1. When the element value is 1, there is solid, and when the value is 0, there is void:

$$\rho(\mathbf{x}) = \begin{cases} 1, & \mathbf{x} \in \mathcal{D}_{solid} \\ 0, & \mathbf{x} \in \mathcal{D}_{void} \end{cases} \quad (7.1)$$

$$\forall \mathbf{x} \in \mathcal{D} = \mathcal{D}_{solid} \cup \mathcal{D}_{void},$$

where \mathbf{x} is the position in the solution domain \mathcal{D} , and \mathcal{D}_{solid} and \mathcal{D}_{void} represent the solid and void regions, respectively. The size of the discrete elements is selected as $\Delta d = d/20$.

Total power absorbed and scattered are calculated via power monitors of FDTD software placed inside and outside the light source. Total-field scattered-field (TFSF) light source is originated in the x-direction, which is the plane wave light source specialized for the simulations of the scattering objects. All boundaries are modeled as perfectly matched layers (PML). The locations of the absorption and scattering monitors are indicated in Figure 7.1 b.

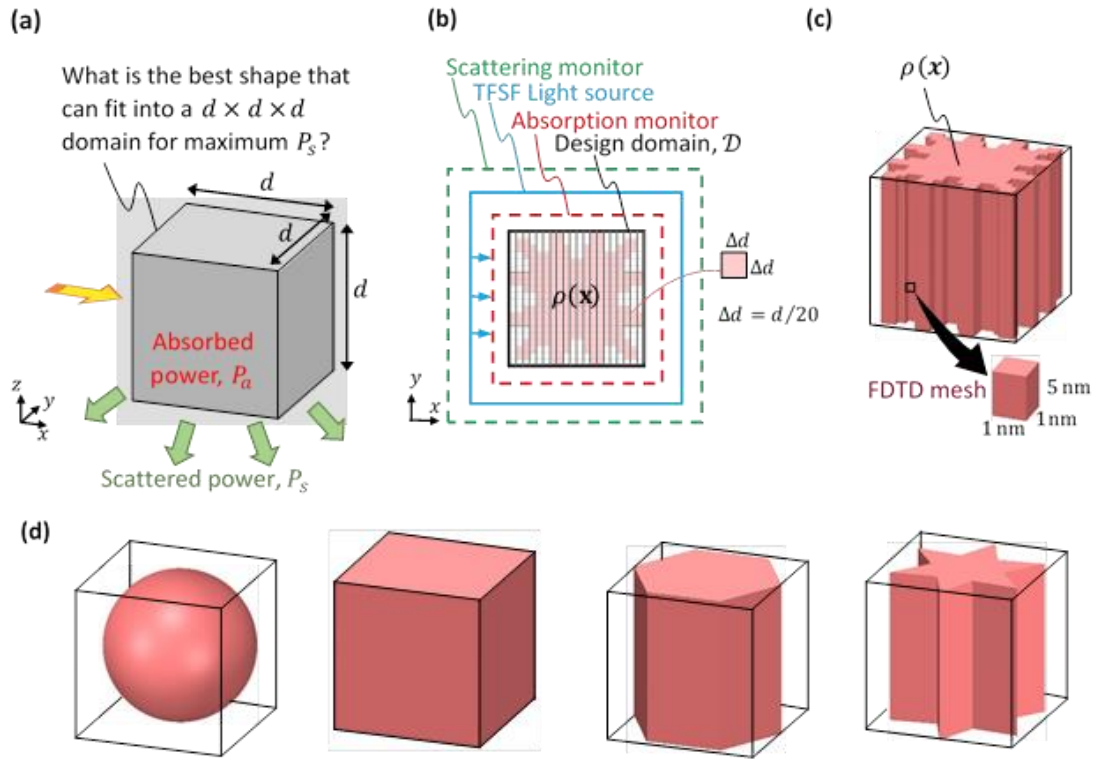


Figure 7.1. (a) Problem illustration and physical mechanisms involved, (b) schematic of a hypothetical geometry, monitor locations and the light source. $\rho(\mathbf{x})$ is the density function and Δd is the size of the discrete element, (c) three dimensional representation of the arbitrary geometry with computational mesh used in the study, (d) known shapes: sphere, cube, and prisms of hexagon and hexagram. The cubic domain with black edges is $d \times d \times d$, $d = 100\text{nm}$ in the present study.

The size of the computational mesh is selected as $d/100$ in the x and y directions, and $d/20$ in the z direction, respectively (Figure 7.1c). Mesh size in the x - y plane is kept smaller in order to capture changes in the density function. The mesh size strongly affects the reliability of the results. The spatial mesh is commonly recommended to be between $\lambda/20$ and $\lambda/10$ for dielectric materials, where λ is the operating wavelength [231–233]. Furthermore, since the wavelength is shorter inside metal particles due to large refractive indices, smaller mesh sizes are preferred. The mesh size in the present study corresponds

to $\lambda/60$ and $\lambda/300$, for the shortest wavelength in this study, $\lambda = 300$ nm. Figure 7.2 shows the variation of the C_s with different mesh sizes. The effects of dx and dy are presented in Figure 7.2 a and the effect of dz is shown in Figure 7.2b. $dx = dy = 1$ nm and $dz = 5$ nm are used throughout the study. The differences in C_s between the mesh used and the finest mesh are less than 6%. The percentage values of the results compared to the finest mesh are indicated in the figure.

Figure 7.1 d indicates a possible set of three-dimensional nanoparticles used for comparison in this study. Each particle is selected to fit in the same domain as the designed particles. These structures are chosen since they are commonly used and well-defined with distinct geometric characteristics. For example, the cube is more polarizable than the sphere due to its sharp corners. On the other hand, as the number of corners of a convex shape increases, it approaches a sphere, such as a hexagon. Due to possessing sharper edges, star-like geometries are also more polarizable compared to compact shapes.

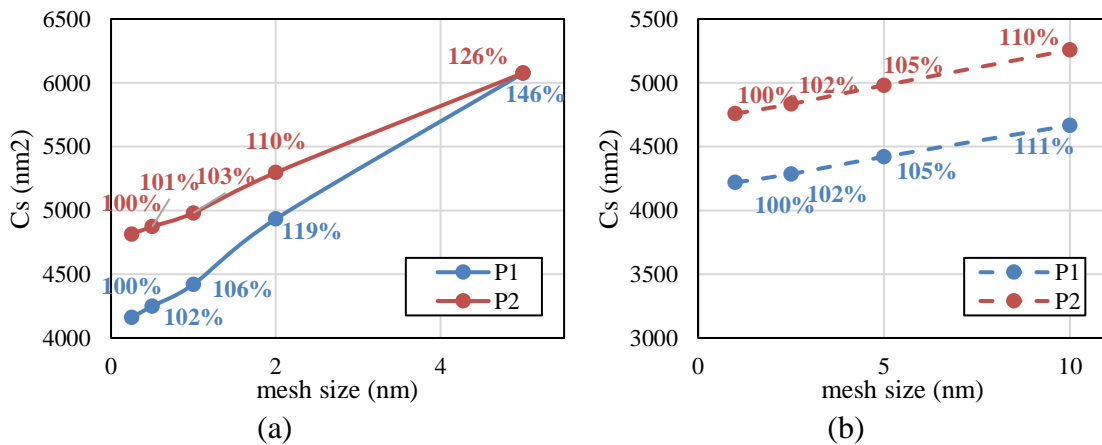


Figure 7.2. The variation in the C_s values of the optimized shapes from P1 and P2 at $\lambda = 300$ nm with respect to the (a) x and y meshes, (b) z mesh

7.2. Optimization

In the present problem, the aim is to maximize the scattering cross section in a given domain. The restriction on the geometry is given by the constraint: $x_{max} = d$ and $x_{min} = 0$, enforcing the structure to be designed in a box with a side length d . In general, every maximization problem can be written as an equivalent minimization problem as:

$$\max_{\rho(\mathbf{x})} f(\mathbf{x}) \equiv \min_{\rho(\mathbf{x})} \{-f(\mathbf{x})\} \quad (7.2)$$

The problem objective can be stated at a single wavelength or multiple wavelengths:

P1. Single λ :
$$f(\mathbf{x}) = C_s(\rho(\mathbf{x}), \lambda) \quad (7.3)$$

P2. Multiple λ :
$$f(\mathbf{x}) = \sum_{i=1}^{N_\lambda} C_s(\rho(\mathbf{x}), \lambda_i) \quad (7.4)$$

The number of wavelengths N_λ at which the optimization is performed can vary based on the problem requirements and computational resources. If a broadband enhancement is desired, a large N_λ must be selected. Additionally, the objective function can be chosen differently, such as a weighted sum, in order to highlight some portion of the spectrum.

Topology optimization can offer a vast space of possible designs for given structural design problems. There are several classes of topology optimization, such as density based methods and level set based methods. In density based methods, the domain is represented by a density function: $\rho: \mathcal{D} \rightarrow \{0,1\}$ given in equation (7.1). Note that ρ can be both binary and continuous. In this study, the binary density function is considered. In genetic algorithms (GA), sets of solutions (populations) are generated by rules mimicking biological evolution such as crossover and mutation, followed by a natural selection-like

process for likely survival of the best bits (genomes) of the previous designs. The search begins with generating an initial random population and calculating their fitness (cost) values. The cost function of the present problem is given as the negative of the objectives in equations (7.3) and (7.4). Then individuals with the smallest fitness values are selected as elites and survive to form the next generation. Additional individuals are created by mutation and cross-over operations on the parents (previous population). GA operates with binary strings, which makes topology optimization a natural extension of GA [124].

7.3. Filtering

In order to avoid checkerboard appearance (small voids and solid islands in the solution domain), some form of regularization is necessary for density based topology optimization, which is called filtering. Filtering can be divided into density based and sensitivity based methods. Sigmund [234] proposed several filtering techniques based on image morphology operators, avoiding grey transition areas while providing equivalent quality with density based filtering methods. Here we used the basic morphology operators like “dilate” and “erode” as well as their extensions, “open” and “close” (obtained by sequentially applying “dilate” and “erode”, respectively). The basic density filtering [235] is also illustrated. Sensitivity filtering is not used in the present study since gradient information is not explicitly available.

The filtering operators are applied to the neighborhood of the individual cells. The neighborhood of the k^{th} cell comprises the cells that have centers equal or closer to the center of k^{th} cell than filter radius R :

$$N_k = \{i \mid \|\mathbf{x}_i - \mathbf{x}_k\| \leq R\}, \quad (7.5)$$

where \mathbf{x}_i and \mathbf{x}_k are the center coordinates of the cells i and k , respectively. One of the most convenient choices is the 4-connected ($R = \Delta x$) neighborhood, which involves the target cell and four adjacent cells.

The filtering methods used in this study are summarized in Table 7.1. $\rho_i = \rho(\mathbf{x}_i)$ is the cell value of the density function in equation (7.1). Weight function, $w(\mathbf{x}_i)$ in the density filter method favors the target cell compared to the adjacent cells for checkerboard suppression [235]. v_i is the volume of the individual cells, which is identical in the present study. β is a filtering parameter and chosen as a result of an independent optimization.

Table 7.1. Filtering methods used in the present study.

Method	Expression	Notes
Dilate (d)	$\tilde{\rho}_d(\rho_i) = \frac{1}{\beta} \log \left(\frac{1}{N_k} \sum_{i \in N_k} e^{\beta \rho_i} \right)$	$\beta = 100$
Erode (e)	$\tilde{\rho}_e(\rho_i) = 1 - \frac{1}{\beta} \log \left(\frac{1}{N_k} \sum_{i \in N_k} e^{\beta(1-\rho_i)} \right)$	$\beta = 100$
Close (c)	$\tilde{\rho}_c(\rho_i) = \tilde{\rho}_e(\tilde{\rho}_d(\rho_i))$	
Open (o)	$\tilde{\rho}_o(\rho_i) = \tilde{\rho}_d(\tilde{\rho}_e(\rho_i))$	
Density filtering (df)	$\tilde{\rho}_{df}(\rho_i) = \frac{\sum_{i \in N_k} w(\mathbf{x}_i) v_i \rho_i}{\sum_{i \in N_k} w(\mathbf{x}_i) v_i}$	$w(\mathbf{x}_i) = \begin{cases} 4, & i = k \text{ (center)} \\ 2, & i \neq k \text{ (adjacent)} \end{cases}$

Furthermore, a simple yet effective technique is utilized for removing checkerboard patterns following the filters. According to this technique, solid boundary cells surrounded by voids are emptied; or void interior cells surrounded by solids are filled:

$$\begin{aligned} \text{Boundary cells: } \rho_k &= 0 && \text{if } \rho_k = 1 \text{ and } \forall \rho_i = 0, i \in N_k(i \neq k) \\ \text{Interior cells: } \rho_k &= 1 && \text{if } \rho_k = 0 \text{ and } \forall \rho_i = 1, i \in N_k(i \neq k) \end{aligned} \quad (7.6)$$

The equation above maintains the unique geometric features on the edges of the domain while filling the small interior voids. This way, unrealistic features are avoided.

7.4. Results and Discussion

The results are presented for both single wavelength ($P1 = 600 \text{ nm}$) and multi-wavelength ($P2 = \{300 \text{ nm}, 500 \text{ nm}, 700 \text{ nm}\}$) cases. Wavelengths of the case P2 are selected from the visible spectrum. Although N_λ is selected arbitrarily for the present study, it can be enforced by the problem or computational resources. The geometry of the structures is taken as 2-D (Figure 7.1 b), and simulations are performed in 3-D (Figure 7.1 c). 1/8 of the geometry is optimized, and the rest of the domain is extended, assuming symmetry, adopting a strategy similar to those of [124,230]. The geometry is restricted to be designed in a $d = 100 \text{ nm}$ domain. In GA, the population size is 100 and cross-over fraction is 0.8. The size of discrete elements is selected as $d/20$ (can also be smaller or larger based on the fabrication constraints and other conditions). One should choose this size carefully since a smaller size increases the computational cost while a larger size may fail to represent all geometric features. Figure 7.3 shows the topologies of the resulting structures. The optimized (1/8 of the all) regions are indicated here with red triangles. The final cost functions are presented and compared to those of sphere, hexagonal prism and

cube in Table 7.2. The final objective function of P1 is 5 – 35 times larger than those calculated for benchmark shapes. It is 2 – 10 times larger for P2, compared to the benchmark cases computed at multiple wavelengths.

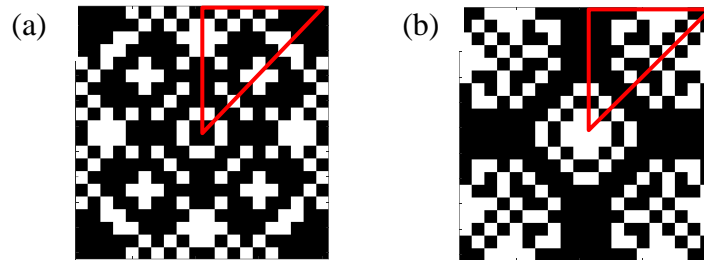


Figure 7.3. Optimized particle shape results from (a) P1, (b) P2. (black: solid, white: void).

Table 7.2. Optimized objective functions in nm^2 (equations (7.3) and (7.4)) compared to cube, sphere, hexagon, and hexagram prisms.

	Optimized	Cube	Sphere	Hexagon	Hexagram
P1: Single-wavelength (600 nm)	132,025	28,650	3,790	6,353	8,150
P2: Multi-wavelength (300, 500, 700 nm)	194,984	90,579	20,337	30,715	85,680

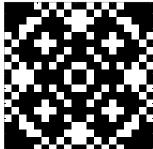
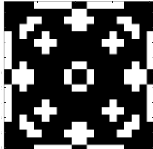
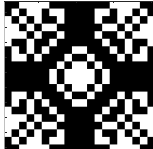
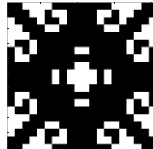
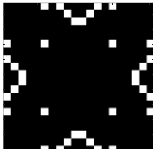


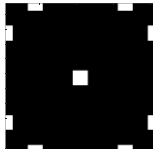

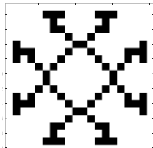
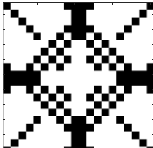
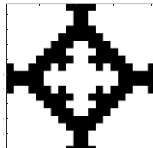

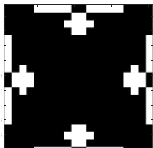
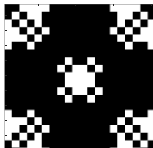
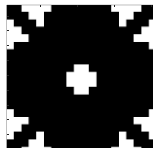

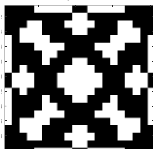
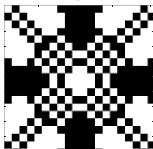
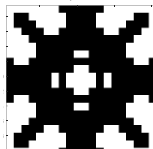
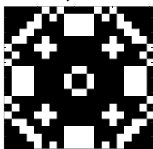
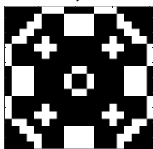
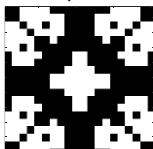
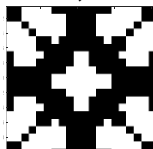
As demonstrated in Figure 7.3, the optimal design shapes have checkerboard appearances in some areas. As a post-processing step, different filtering methods are applied to the optimized shapes. In Table 7.3, the resulting shapes from the filtering study are listed with the objective values for P1 and P2. Note that the checkerboard control (CB) technique (equation (7.6)) is implemented as a separate filter (original w/CB control) or following the initial filters (d, e, c, o w/CB). When the checkerboard (CB) control is off (columns 1

and 3 in Table 7.3), the “close” method can be considered as the most successful for P1 in terms of fidelity to the original shape; since the highest cross section is obtained among those filtered. Nevertheless, the scattering cross sections are significantly smaller than the optimization result. Furthermore, the checkerboard appearance still exists in the filtered shapes, especially in the domain boundaries.

The CB control eliminates the checkerboard appearance significantly. The highest objective values are obtained in the “open” technique despite the relatively low objectives it yields when CB is off. Moreover, the objective of “open w/CB” P1 is slightly higher than the original P1 result, which shows that GA converged to a point near the global optimum. Using a local search following GA can resolve the immature optimization and result in finding the global optimum. Yet, one should note that the optimized objective value in P1 is only 1.5% smaller than the “open w/CB” P1 result, which can be regarded as a successful optimization.

In the case of P2, “open w/CB” provides a relatively higher objective value than other filtered structures and the geometry is more realizable. On the other hand, the original result of P2 is 1.6 times larger than that of P2 “open w/CB” unlike the previous case. One explanation can be that the optimal point of the multi-wavelength problem is an isolated instant; therefore, the objective function drops in the vicinity of the optimum. As a result, the “open w/CB” filter is concluded as the most useful filter. We refer to the output of “open w/CB” as the “filtered” result in the rest of the paper. Figure 7.4 compares the objective functions of the filtered geometries, the original results and the benchmark shapes.

Table 7.3. Objective function values (equations (7.3) and (7.4)) of the original shape and the filtered shapes in nm^2 using different methods. d: dilate, e: erode, c: close, o: open, df: density filtering with and without checkerboard control.

	P1 ($C_{s,\lambda=600\text{nm}}$)		P2 ($\sum_{\lambda=300,500,700\text{nm}} C_{s,\lambda}$)	
	No CB control	w/ CB control	No CB control	w/ CB control
original	 132,025	 89,263	 194,984	 77,411
d	 37,504	 34,420	 118,495	 112,078
e	 40,674	 440	 13,764	 24,014
c	 61,322	 44,637	 113,047	 26,764
o	 26,490	 134,439	 85,970	 120,304
df	 478	 2,800	 13,165	 11,182

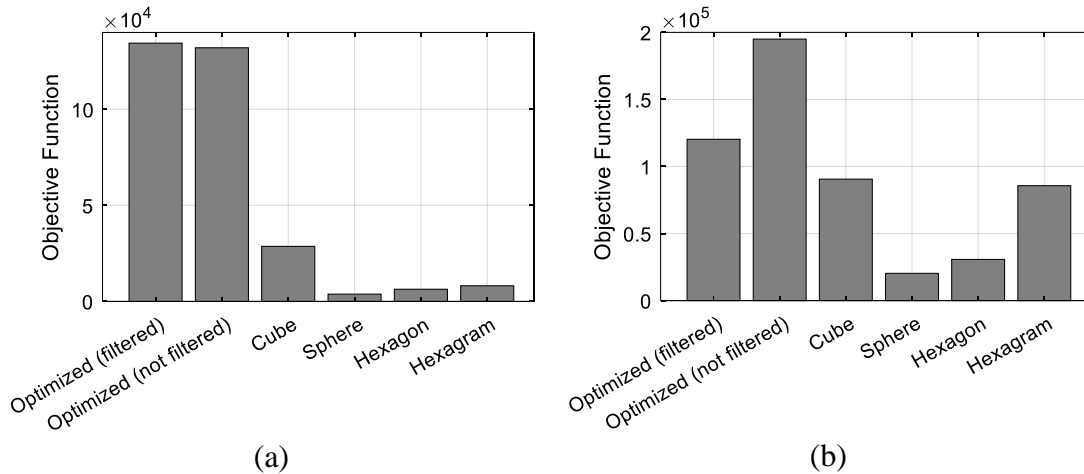


Figure 7.4. Comparison of the objective function values of filtered optimum (method: open w/CB), unfiltered optimum and benchmark shapes. (a) P1, (b) P2.

A noteworthy result from Table 7.3 is that when CB is off, the highest objective function is obtained with the “dilate” filter, where the filtered geometry looks more like a cube than the original optimized shape. Although, as shown in Table 7.2, the objective value of the cube is not very high, objective values of “dilate no/CB and w/CB P2” are almost 1.2 times more than that of the cube despite their similar shapes. Another interesting result is that despite the visible similarity between the resulting shapes by “original w/CB” and “df w/CB” of both P1 and P2, objective values of “original w/CB” are around 30 and 7 times larger than that of “df w/CB” of P1 and P2, respectively. These results reinforce our initial claim that the optical response of nanoparticles changes considerably, even with the presence of tiny differences among particles.

The optimized C_s profiles are presented in Figure 7.5a and Figure 7.6a for P1 and P2, respectively, and compared to those of benchmark shapes. In general, topology optimization is successful at maximizing C_s at the wavelength of interest. C_s is higher than

those of benchmark shapes at the wavelengths where optimization is performed (indicated by stars). Since the original and filtered shapes of P1 resulted in similar objective values, the corresponding spectral scattering cross sections are also quite similar. On the other hand, the scattering spectra of P2 blueshift after filtering. The peak scattering by the filtered shape occurs at 600 nm while occurring at around 680nm before filtering. One way to avoid this amount of change in the scattering profile is to implement the filtering method after each optimization step. Nevertheless, the objective function is still considerably larger than all the reference shapes; thus, one can say that the purpose of this problem is fulfilled.

Even though the comparison of common shapes is out of the scope of the present study, a brief discussion about their optical properties is included for completeness. Cube and sphere result in the largest and the smallest objective function values among the benchmark cases, which is expected for several reasons: The cube has several corners and has a larger volume to surface ratio. Also, the sphere is a compact shape with no advantage of sharp edges. An alternative objective function is the scattering efficiency obtained by the ratio of the scattering cross section to the physical one when the amount of material is also an important consideration. With this objective function, the hexagram is expected to yield the highest objective value among the benchmark shapes due to its small area. It will be a valid argument to expect different shapes as a result of this optimization.

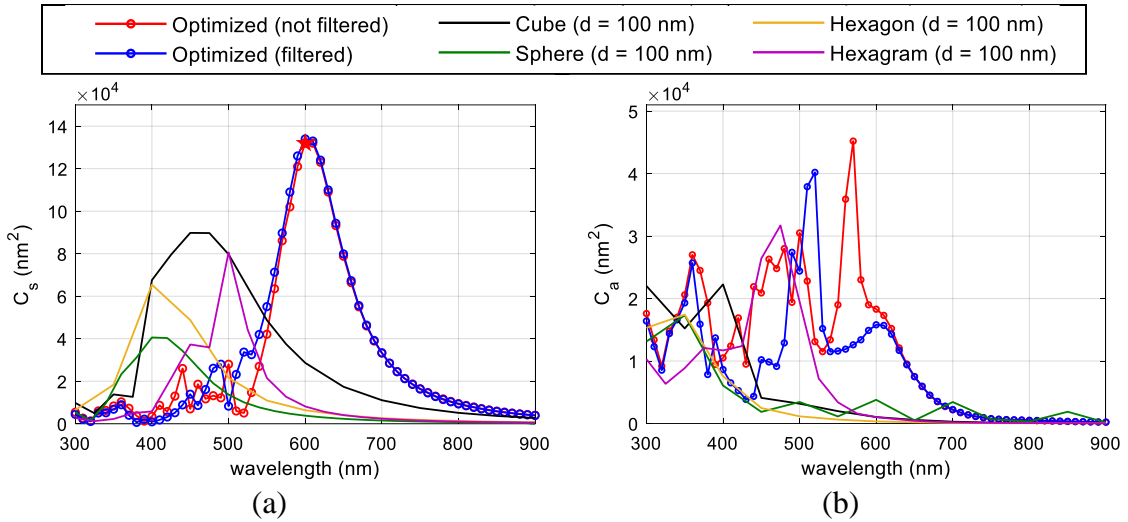


Figure 7.5. C_s and C_a from the optimized geometries P1 compared with the profiles of benchmark shapes obtained from FDTD simulations.

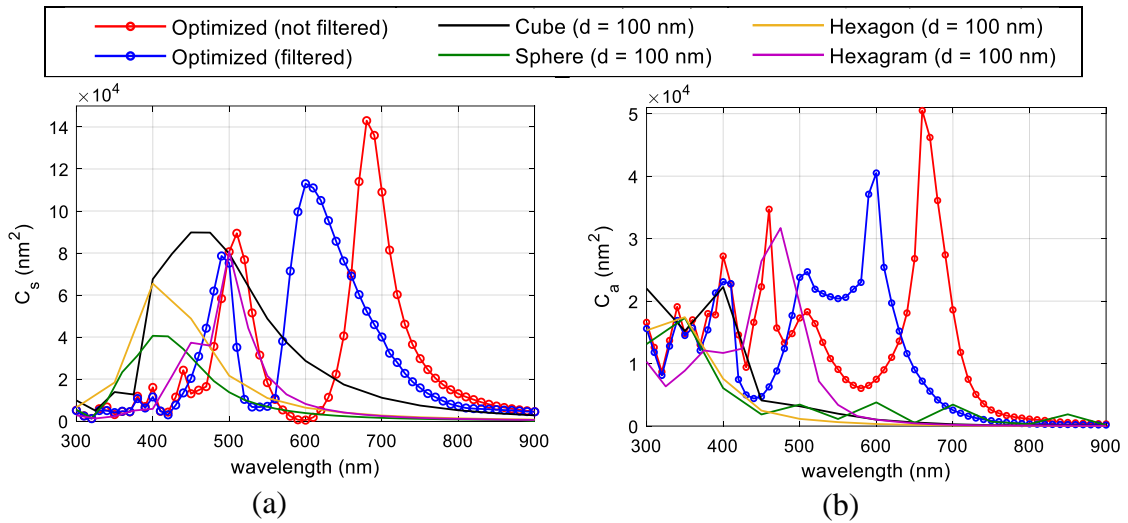


Figure 7.6. C_s and C_a from the optimized geometries P2, compared with the profiles of benchmark shapes obtained from FDTD simulations.

Furthermore, though not included in the present study as an explicit objective, absorption cross sections of the optimized structures are presented in Figure 7.5 b and Figure 7.6 b for P1 and P2, respectively. Absorption cross sections can be an important metric in some applications. In others, it can be regarded as a loss. It can also be included

in the objective as a secondary cost function or a constraint. For this analysis, the host medium (absorber) is important; therefore, it can be analyzed for different applications separately.

The impact of the particle shape on the optical properties for small particles is established by equation (2.13) by the shape factor ξ in polarizability. The size range in the present study is much larger than a single dipole; therefore, higher-order resonances occur. Additionally, targeting different objective functions resulted in scattering spectra having peaks at desired wavelengths. P1 has a single peak centered at 600 nm, while several other resonances are located at shorter wavelengths. With its two distinct peaks, P2 behaves as a superposition of two different particles. In P1 and P2, absorption occurs at short wavelengths due to the nonzero imaginary refractive index of silver. On the other hand, at the longer wavelengths, neither absorption nor scattering is observed. The reason why the scattering spectra of P1 and P2 have certain characteristics can be perceived by the electric fields in the solution domain in the solution domain in Figure 7.7 and Figure 7.8.

The electric fields are localized at the corners of the shapes as expected. The highly localized field enhancement for both P1 and P2 at 600 nm explains the scattering enhancements in both problems at the same wavelengths. Although the electric fields are intense at 500 nm, it translated to the absorption enhancement in P1, where the particle behaves like an electromagnetic trap. For P2, electric field magnitudes are large, resulting in the second peak of the scattering spectra; yet, it is observed in a spatially small region; therefore, the scattering enhancement is not as significant.

Furthermore, the forward and backward scattering cross sections are plotted in Figure 7.9. Here the forward scattering is the sum of the scattering in the positive horizontal direction, and backward scattering is that in the negative horizontal direction. Thus, the upper and lower sides of the shapes are also included in the calculations. The forward and backward scattering spectra are mostly identical except asymmetry at 600 nm. This asymmetry occurs at peak wavelength, 600 nm, which can also be observed from in Figure 7.7 and Figure 7.8.

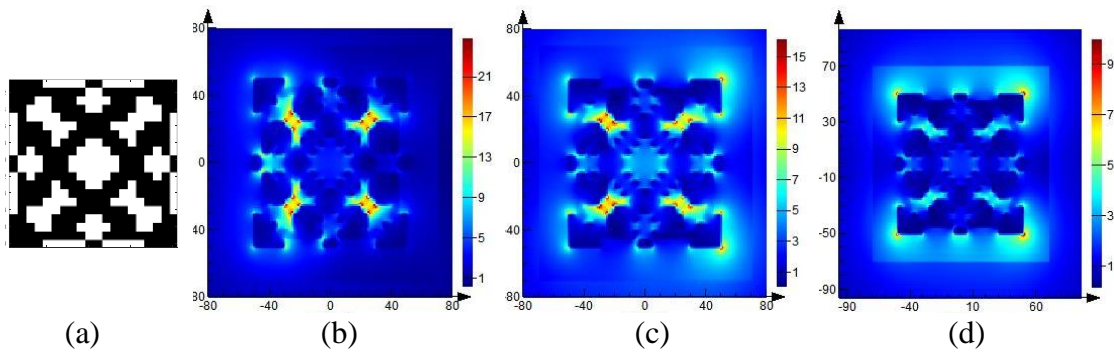


Figure 7.7. (a) Filtered optimized geometry from P1. (b-d) Magnitudes of the electric field near the particle in part (a) at wavelengths (b) 500 nm, (c) 600 nm, (d) 700 nm.

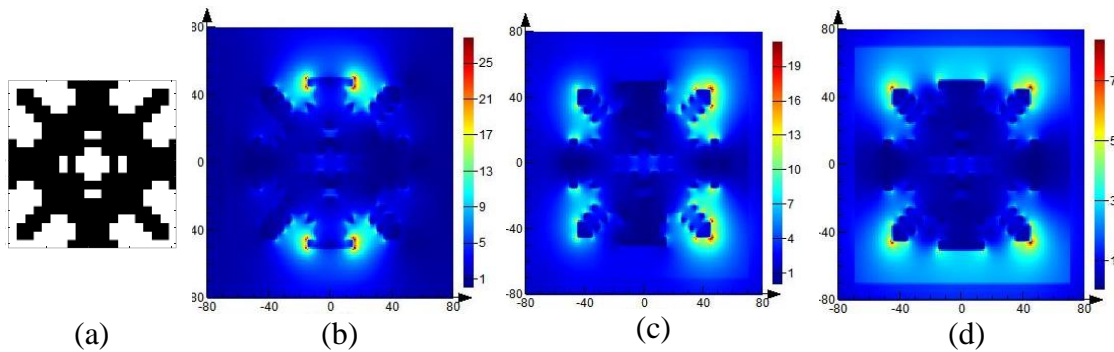


Figure 7.8. (a) Filtered optimized geometry from P2. (b-d) Magnitudes of the electric field near the particle in part (a) at wavelengths (a) 500 nm, (b) 600 nm, (c) 700 nm.

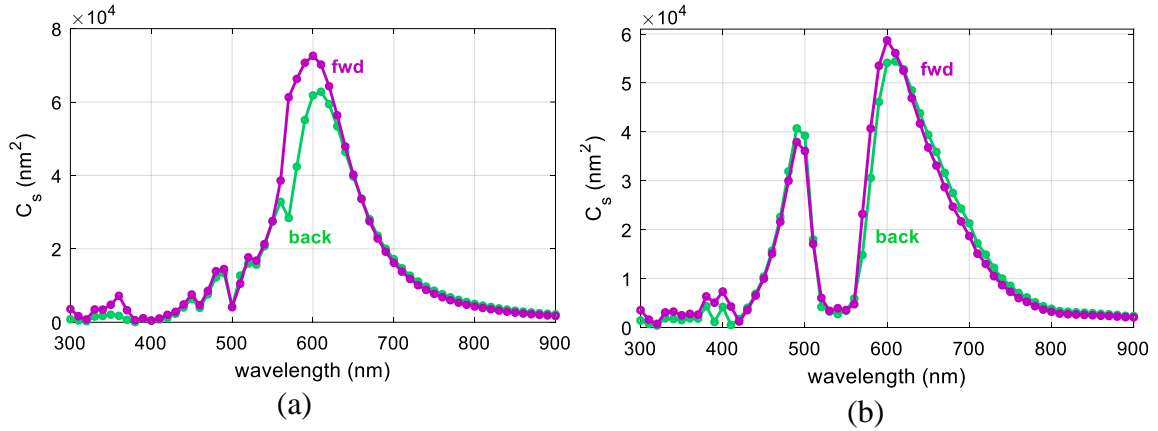


Figure 7.9. Forward and backward C_s of the optimized (filtered) geometries (a) P1, (b) P2.

The anisotropic shapes can exhibit nonuniform angular characteristics; therefore, it is important to quantify the angular variation of the scattered power. The angular variation of the scattering can be calculated using the Poynting vector from equation (2.18). Defining \mathbf{p} as the real part of the Poynting vector, the normalized real part of the Poynting vector, p , is calculated as:

$$\mathbf{p} = \text{Re}(\mathbf{E} \times \mathbf{H}),$$

$$p = \frac{|\mathbf{p}|}{I_0} = \frac{1}{I_0} \sqrt{p_x^2 + p_y^2 + p_z^2} \quad (7.7)$$

The angular scattering is calculated in three main planes: x-y, x-z, and y-z. A circular monitor comprising of 360 point monitors equally spaced in the angular direction is located at a $1.2d$ radius. These point monitors calculate the spatial components of the electric and magnetic fields ($E_x, E_y, E_z, H_x, H_y, H_z$). Figure 7.10 shows the placement of these monitors with their starting points (0).

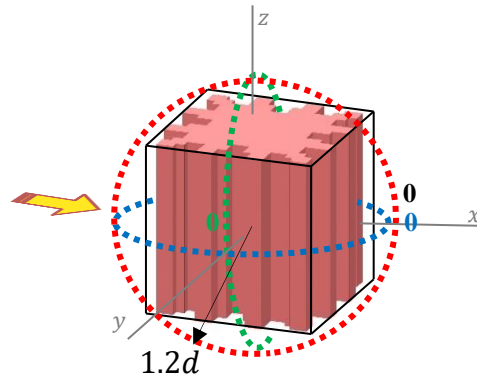
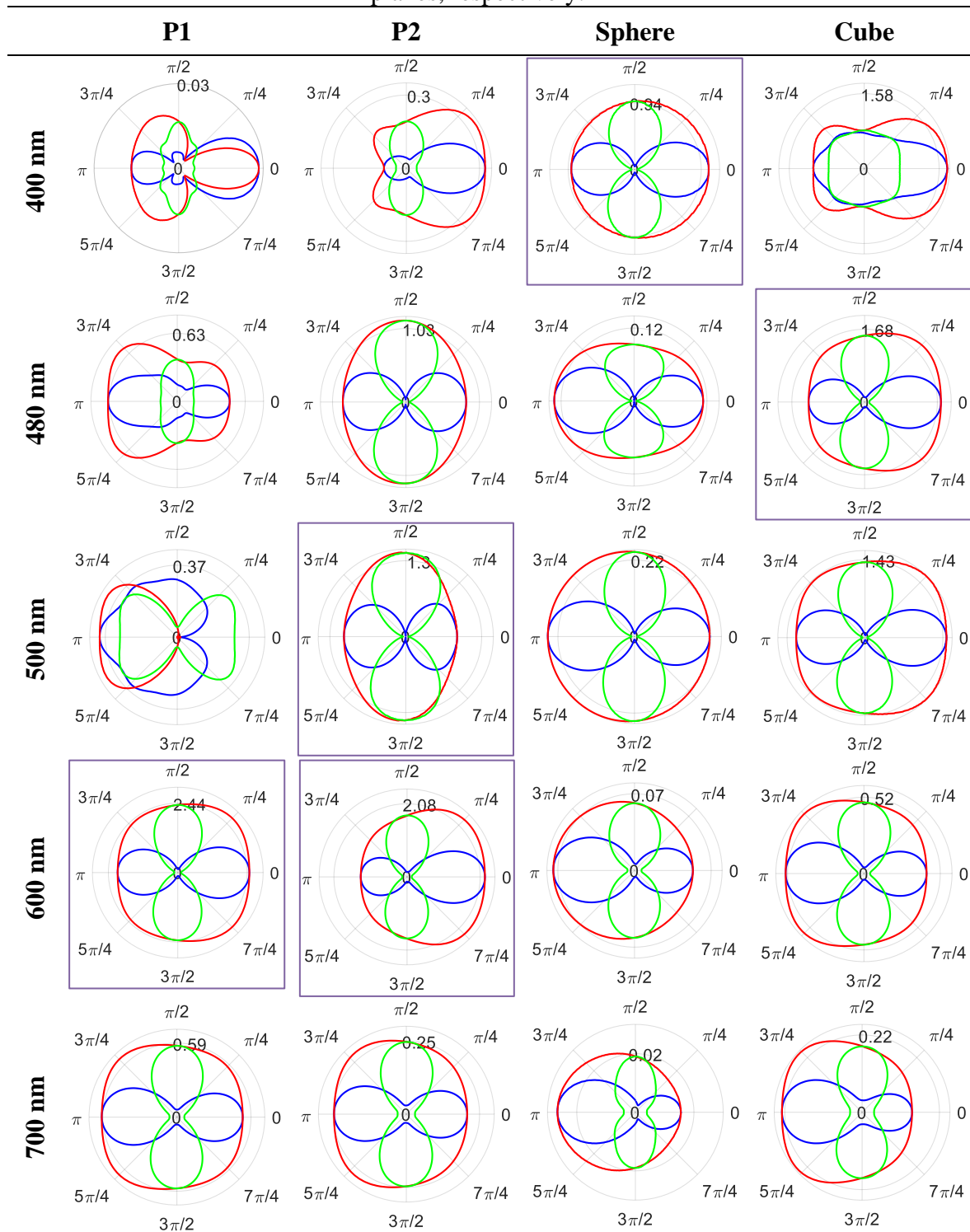


Figure 7.10. Locations of the circular monitors.

In Table 7.4, the polar plots of angular scattering on x-y (blue), x-z (red), and y-z (green) planes shown in Figure 7.10 are presented. Results of the sphere and cube are also included for comparison. Polar plots are presented at the wavelengths that each shape has a primary or secondary resonance close to 400nm (sphere), 480nm (cube), 500nm (P2), 600nm (P1 and P2). 700nm is also included for comparison. At longer wavelengths, the angular scattering characteristics become similar even though the numerical values are different. It is noteworthy that in P1, despite no distinct resonances, the scattering power is larger than those of the sphere and cube. The effect of the shape can be especially seen at the scattering on the x-z plane. All shapes except sphere show square-like profiles at the angles $\pi/4$ and its integer multiples, owing to their sharp edges. At resonance wavelengths, the angular profiles become rounder and more uniform along the angular position. At wavelengths, where a significant amount of scattering occurs, the polar plots show that the anisotropic particles do not lead to a highly directional scattering. When scattered power is small, the angular variation is almost arbitrary for P1 and P2.

Table 7.4. Polar plots of the normalized real part of Poynting vectors from filtered optimized P1 and P2, sphere, and cube. Blue, red, and green lines show x-y, x-z, and y-z planes, respectively.



In Figure 7.11, the average p is plotted for these planes with their angular deviation. Note that the trends of the average angular scattering are similar to the results in Figure 7.5 and Figure 7.6. The smallest angular variation occurs in the x-z plane which can also be observed in Table 7.4.

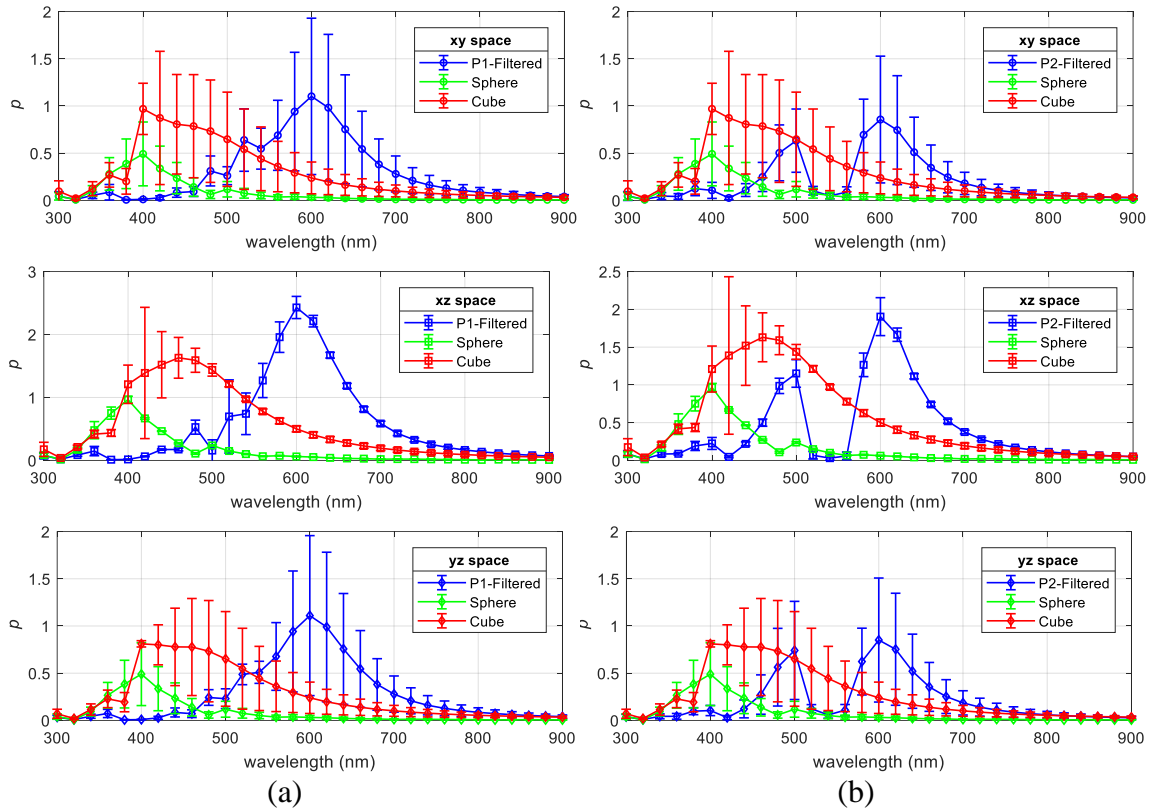


Figure 7.11. Angular variation of the real part of pointing vector on different principle axes with the wavelength.

7.5. Conclusion

In this chapter, a theoretical study was conducted to obtain efficient scatterers at the nano scale using evolutionary topology optimization. As a result, the objectives of the

optimization studies increased 2-35 times compared to common shapes such as cube, hexagon, hexagram, and sphere. Spectral scattering cross sections were increased between 1-10 times. Furthermore, we proposed using filtering methods to reduce the chance of undesired structures getting picked up by the search. Density filtering and image morphology methods were used with the proposed checkerboard control techniques. Among these methods, the “open” method with the checkerboard control (open w/CB) is found to be the most effective in reducing undesired geometric features and fidelity to the original geometry. Filtering and checkerboard methods can also be included as intermediate steps of the optimization; thus, unrealistic features are avoided in the simulations. This can also accelerate the overall optimization time since the number of possible solutions is reduced.

Although the enhancement in the scattering performance is promising, the manufacturability of the structures should be considered to obtain realizable geometries. For example, the discrete element size of topology optimization should be selected according to the fabrication capability. Custom optimization constraints can also be imposed, such as minimum feature size. Nonetheless, the presented design framework can be useful in many applications where tailored optical properties are desired with common materials. One of the potential applications of this framework is to design light trapping nanoparticles for thin film solar cells by including additional physical considerations, such as periodic interactions among the designed particles and surrounding solar cell materials.

8. SHAPE DESCRIPTORS TO PREDICT SCATTERING BY NANOPARTICLES

The strong dependence of the nanoparticle radiative response to the particle shape makes the geometry design an attractive method for unique devices that utilize nanoparticles [67–69]. However, a major hurdle in the study of arbitrary shapes' physical responses is the lack of universal (geometry) parameterization. One of the solutions to this challenge is topology optimization, as studied in Chapter 7. As commonly used in image recognition, geometric predictive features can also collectively characterize a particle of arbitrary shape. When taken in as independent variables, they can result in predictive models for the radiative response of nanoparticles. Data driven methods can achieve two goals: first, the computational burden of the optical modeling is overcome; second, an intuitive relationship is established between the geometric features and spectral radiative response.

In this chapter, a data driven approach is used to predict the optical scattering of nanoparticles with arbitrary shapes. The geometric shape features are computed using image characterization methods adopted from image recognition with a novel approach to incorporate the interaction of light. The methodology of the study is summarized in section 8.1. Then, the arbitrary shape generation methodology is explained in Section 8.2. The predictive geometric features for shape characterization are presented, and the dataset is described in Sections 8.3 and 8.4, respectively. The results of the training and test sets are presented and discussed in Section 8.5. The conclusions of the chapter are presented in the last section.

8.1. Methodology

This study aims to establish a relationship between the nanoparticle shape and its radiative scattering using data driven prediction methods. The predictive models use custom designed geometric features as input. The procedure is summarized in Figure 8.1. First, random polygons are generated using a methodology described in the next section. Then electromagnetic simulations are performed to find target outputs (scattering cross section) for the generated shapes. Meanwhile, the values of geometric features for the generated polygons are calculated (Section 8.3). The dataset containing the features (X -values) and the targets (y -values) is then supplied to regression models for training. Finally, the prediction performance is evaluated using a test set that has not been used by the regression models during training.

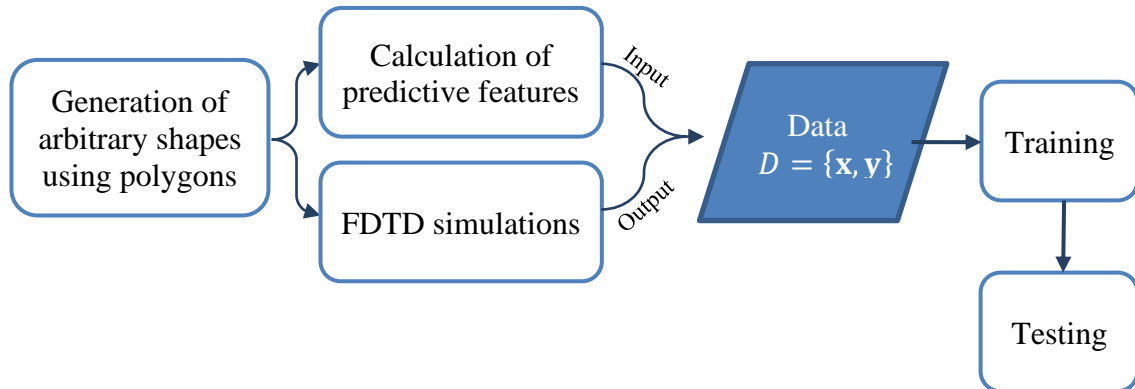


Figure 8.1. Flowchart describing the proposed predictive modeling design pipeline.

8.2. Construction of Random Shapes

The arbitrary shapes are represented by *polygons* due to their geometric diversity and ease of construction. A polygon is a closed shape in R^2 that can be fully characterized via its adjacent vertex coordinates. The only condition to identify a valid polygon is that the segments connecting adjacent vertices must not intersect (Figure 8.2). The polygon generation procedure involves the following steps:

1. Randomly selecting the number of vertices, N_v ,
2. Dividing the coordinate system to N_v angular segments (to avoid intersection),
3. In each segment, randomly selecting a radius and an angular position for each vertex.

Cartesian and radial coordinates of the i^{th} vertex are represented by V_i and Ψ_i . All polygons in our database are represented with equisized vectors. To do so, we use a different mathematical representation, where the polygon boundary is divided into n_d elements (Figure 8.2). n_d is a user defined value, selected as 360 in this study. Figure 8.2 shows the schematic of a polygon. i is the index of a vertex and N_v is the number of vertices in the given polygon. j is the index of boundary points. The point G indicates the centroid of a polygon. The centroid location of a polygon is calculated as:

$$G = \begin{bmatrix} \bar{x} \\ \bar{y} \end{bmatrix} = \frac{1}{3 \sum_{i=1}^{N_v} (x_i y_{i+1} - x_{i+1} y_i)} \begin{bmatrix} \sum_{j=1}^{n_d} (x_j + x_{j+1})(x_j y_{j+1} - x_{j+1} y_j) \\ \sum_{j=1}^{n_d} (y_j + y_{j+1})(x_j y_{j+1} - x_{j+1} y_j) \end{bmatrix} \quad (8.1)$$

where (\bar{x}, \bar{y}) is the centroid location and n_d is the number of boundary points.

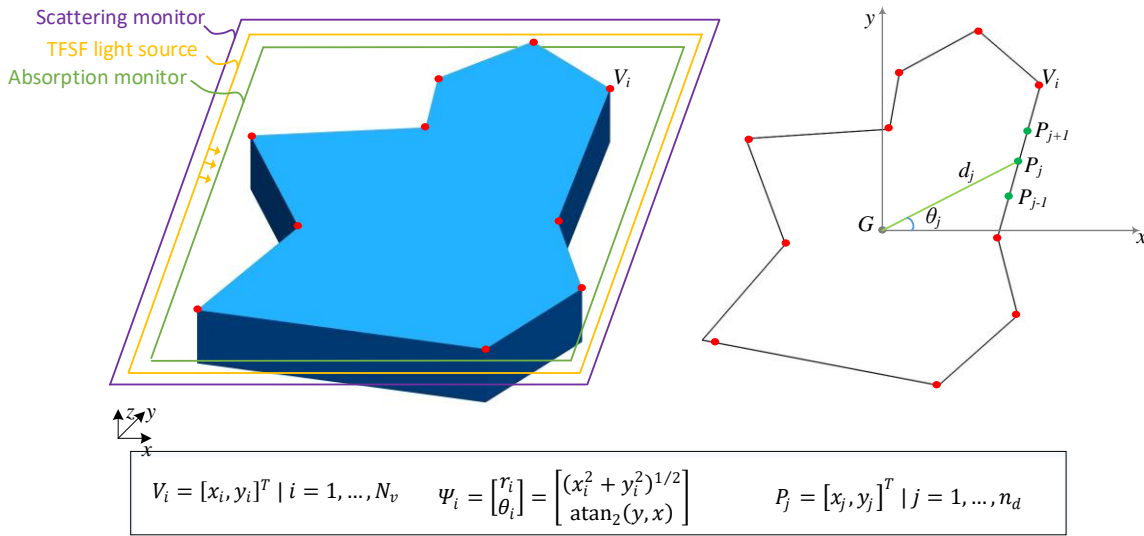


Figure 8.2. Schematic of a polygon. Left: three dimensional polygon-prism with FDTD solution setup, right: definition of vertices, boundary points, and the centroid.

8.3. Predictive Geometric Features

Arbitrary shapes can be characterized using techniques adapted from object recognition and computer vision. In object recognition, shapes are expressed as features and classified using models that take features in as inputs. The shape feature extraction methods in object recognition and classification mainly differ in whether they use the object boundary (*boundary based* methods) or the interior points of the shapes (*region based*) [236]. Since the polygons in this study have no holes, the boundary based methods seem more appropriate. Some of the most widely used approaches for shape representation are polygonal approximations, interrelation evaluation, moments, transforms, chain codes [237], beam angle statistics (BAS) [238], shape context [239], chord distributions [240], and Fourier and wavelet transforms of shape signatures [241,242] and so on [243].

Different moments can be realized, such as invariant moments [244,245], Zernike moments [246], and more. One of the approaches to quantifying the geometric features is the bounding rectangles [247,248] that can help calculating orientation and elongation related features. Additionally, simple descriptors, such as area, perimeter, compactness, eccentricity and perimeter-area ratios, can be given as examples [249]. For the detailed classification of the shape representation methods and specific examples, interested readers are referred to the comprehensive reviews in the literature [236,243,250–252].

Most of the shape representation methods mentioned above characterize a shape via a distribution, which is simply a vector with a size of boundary points n_d . As the distribution based features significantly increase the number of inputs, only the scalar geometric descriptors are selected among the mentioned methods. Furthermore, contrary to object recognition, the scale of the shapes and their orientation with respect to the light direction are essential; therefore, several intuitive features are proposed to capture the directional and local properties of shapes. For example, the symmetry of the particles in the same and perpendicular direction with the light can be a meaningful descriptor. Additionally, the local geometric features in the vicinity of the main axes can be useful. Although quite common, feature elimination and extraction steps in data driven methods are not performed here to allow the collective effect of several features.

In summary, we consider the following criteria in our feature engineering:

- 1) *Shape boundary is sufficient*: the shapes in this study are represented by straight lines with no holes inside.
- 2) *Features are scalars*: the descriptors expressed as distributions are not considered to limit the feature vector size.

- 3) *Orientation matters*: In the current study, the orientation of shapes is important because the light direction is along one direction. A polygon and its certain amount rotated version are different shapes.
- 4) *Scale is important*: Size certainly changes scattering response. Scattering of light by a polygon-shaped object is different from that of the same polygon but scaled up or down in size. Therefore, there must be features characterizing the scale of particles. On the other hand, the features with a primary purpose other than the scale must be scale-independent.

8.3.1. Simple Features

At first glance, an arbitrary polygon can be marked by some simple metrics that explain its very general characteristics. The number of vertices (or edges) (N_v), the area (A), and the perimeter (P) are among the most basic features. Instead of the perimeter, normalized perimeter (p_n) can also be used to obtain a size-independent feature.

$$A = 0.5 \sum_{i=1}^{N_v} (x_i y_{i+1} - x_{i+1} y_i) \quad (8.2)$$

$$p_n = \frac{P}{2\pi\mu_r} = \frac{1}{2\pi\mu_r} \sum_{i=1}^{N_v} \|V_i - V_{i+1}\|$$

where $V_i = [x_i, y_i]^T$ is the coordinate of i th vertex. μ_r is the mean radius of a polygon, calculated by the average of the distances between the boundary points to the centroid (equation (8.1)).

$$\mu_r = \frac{1}{n_d} \sum_{j=1}^{n_d} d_j \quad (8.3)$$

$$\mathbf{d} = [d_1, \dots, d_j, \dots, d_{n_d}]^T$$

$$d_j = \|P_j - G\|$$

Eccentricity is a measure of aspect ratio, where the circle has an eccentricity of 1, and the eccentricity of ellipses approach 0.

$$\xi_e = \frac{c_{xx} + c_{yy} - \sqrt{(c_{xx} + c_{yy})^2 - 4(c_{xx}c_{yy} - c_{xy}^2)}}{c_{xx} + c_{yy} + \sqrt{(c_{xx} + c_{yy})^2 - 4(c_{xx}c_{yy} - c_{xy}^2)}} \quad (8.4)$$

where c_{xx} , c_{xy} and c_{yy} are the coefficients of the following covariance matrix:

$$C = \frac{1}{n_d} \sum_{j=1}^{n_d} \begin{pmatrix} x_j - g_x \\ y_j - g_y \end{pmatrix} \begin{pmatrix} x_j - g_x \\ y_j - g_y \end{pmatrix}^T = \begin{pmatrix} c_{xx} & c_{xy} \\ c_{yx} & c_{yy} \end{pmatrix}$$

$$c_{xx} = \frac{1}{n_d} \sum_{j=1}^{n_d} (x_j - g_x)^2, \quad c_{yy} = \frac{1}{n_d} \sum_{j=1}^{n_d} (y_j - g_y)^2, \quad (8.5)$$

$$c_{xy} = c_{yx} = \frac{1}{n_d} \sum_{j=1}^{n_d} (x_j - g_x)(y_j - g_y).$$

The expression in equation (8.4) is the ratio of the eigenvalues of the matrix C .

Compactness (ξ_c) measures how close an arbitrary shape to a circle, which is considered as the most compact form of the closed shapes. The compactness descriptor is defined as the ratio of the perimeters of a shape and a sphere with the same area ($P^2/A = 4\pi$ for a circle).

$$\xi_c = \frac{2\sqrt{\pi A}}{P} \quad (8.6)$$

Similarly, the rectangularity is the comparison of the shape with a rectangle along a prespecified direction. The rectangularity of a shape can be determined using the bounding box approach (Figure 8.3). In a general sense, the bounding box representation of a polygon refers to the side lengths of the bounding rectangle, making an angle δ with the original x axis [248]. The rectangularity feature is calculated using this approach as:

$$\xi_r = \frac{A}{(L_{\delta=0,x})(L_{\delta=0,y})} \quad (8.7)$$

Other novel features are also proposed to describe a shape. Imagine an observer located on the +x axis, far away from the shape centroid. The angle between two straight lines drawn from the observer to the topmost and bottommost points of the shape is used as a feature called observer angle (ξ_α). Likewise, the observer can see some of the vertices, while the rest stays behind the shape with respect to the observer. The ratio of the visible vertices to the total number of vertices becomes the visible “vertices to the observer” (ξ_v). These features are visualized in Figure 8.4.

$$\xi_v = \frac{\# \text{ of visible vertices}}{N_v} \quad (8.8)$$

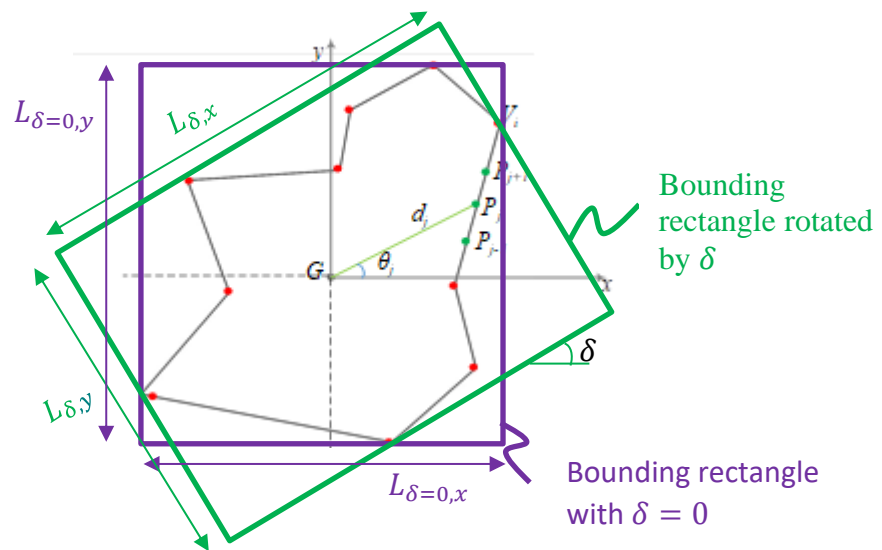


Figure 8.3. Bounding box representation.

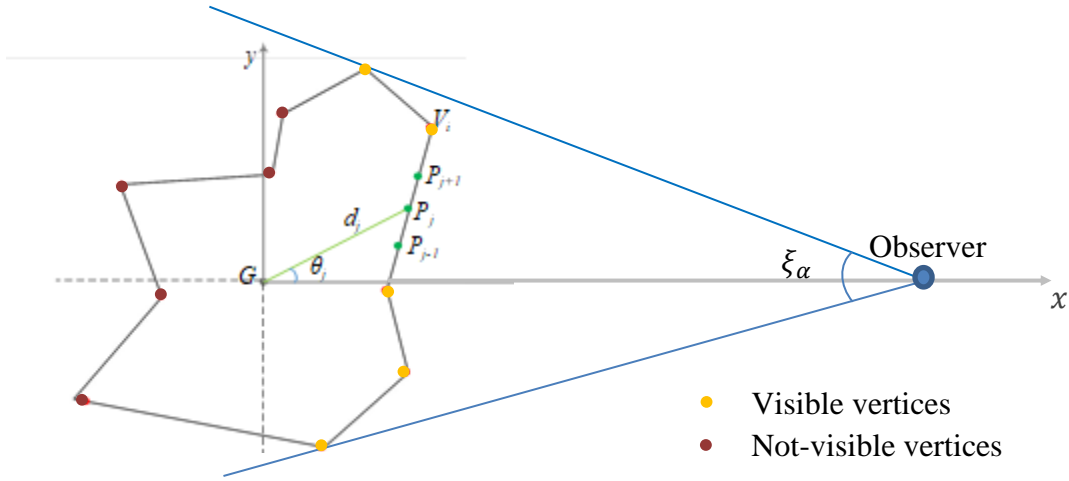


Figure 8.4. Coverage angle from an observer far from the shape and the ratio of the visible vertices from an observer to the total number of vertices.

8.3.2. Moment Based Features

Moment invariants (or image moments) have been one of the earliest approaches to shape identification [253,254]. This approach calculates seven moment invariants derived from the central moments. Central moments of order (p, q) integrates the shape density over a closed region or along a path enclosing a closed shape. For a digital image, (p, q) -th central moment along the shape boundary is defined as:

$$m_{pq} = \sum_{(x,y \in \mathcal{C})} (x - \bar{x})^p (y - \bar{y})^q \quad (8.9)$$

Then the scaled moment becomes:

$$\eta_{pq} = \frac{m_{pq}}{m_{00}^{p+q+1}} \quad (8.10)$$

One should note that the moments are invariant to translation, rotation, and size, which contradicts the guidelines at the beginning of this section; however, as they represent the overall properties of a shape, similar to the simple features, moments are not discarded. Here only the first three moment invariants are included since the rest are almost zero. The first three moment invariants are as follows:

$$\begin{aligned}
\phi_1 &= \eta_{02} + \eta_{20} \\
\phi_2 &= (\eta_{02} - \eta_{20})^2 + 4\eta_{11}^2 \\
\phi_3 &= (\eta_{30} + \eta_{12})^2 + (\eta_{03} - 3\eta_{21})^2
\end{aligned} \tag{8.11}$$

8.3.3. Elongation Related Features

Elongation of a shape can distinguish if the sphere-like or rod-like particles result in more scattering. There are different approaches to calculate elongation. For example, moments can also be used to calculate other useful features, such as elongation [247,248,255].

$$\phi_{e,1} = \frac{\sqrt{\phi_2}}{\phi_1} \tag{8.12}$$

Another approach for elongation is obtained using N -th order central moments, which is obtained using bounding box representation (Figure 8.3):

$$I_N = \sum_{(x,y \in \mathcal{C})} (-x \sin \delta + y \cos \delta)^N \tag{8.13}$$

where δ is the rotation angle from the bounding box approach. Elongation is then expressed as:

$$\phi_{e,N} = \frac{\max\{I_N | \delta \in [0, 2\pi)\}}{\min\{I_N | \delta \in [0, 2\pi)\}} \quad (8.14)$$

In this study, 4th order central moment ($\phi_{e,4}$) is used to calculate elongation (N = 4). In addition, the ratio of the bounding rectangle perimeter to the original perimeter is used as a feature (l_y).

$$l_y = \frac{2(L_{\delta=0,x} + L_{\delta=0,y})}{P} \quad (8.15)$$

To introduce the directionality of the elongation, the extends of the shape along x and y axes are compared to the extent of the shape along arbitrary axes. $\tau_{x,max}$ and $\tau_{y,max}$ compares the distance between the start and the end of the shape along x and y axes, respectively, to the maximum distance in any direction. Similarly, these distances can be compared to the average of the distances between the extends of the shape ($\tau_{x,avg}$ and $\tau_{y,avg}$). These distances can be easily calculated using the boundary points in Figure 8.2.

The formal definitions of these features are as follows:

$$\begin{aligned} \tau_{x,max} &= \frac{d(\theta = 0) + d(\theta = \pi)}{\max[d(\theta_j) + d(\theta_j + \pi) | j = 1, \dots, n_d]} \\ \tau_{y,max} &= \frac{d(\theta = \pi/2) + d(\theta = 3\pi/2)}{\max[d(\theta_j) + d(\theta_j + \pi) | j = 1, \dots, n_d]} \\ \tau_{x,avg} &= \frac{d(\theta = 0) + d(\theta = \pi)}{\text{mean}[d(\theta_j) + d(\theta_j + \pi) | j = 1, \dots, n_d]} \\ \tau_{y,avg} &= \frac{d(\theta = \pi/2) + d(\theta = 3\pi/2)}{\text{mean}[d(\theta_j) + d(\theta_j + \pi) | j = 1, \dots, n_d]} \end{aligned} \quad (8.16)$$

where $d_j = d(\theta_j)$ is the distance between the jth boundary point and the centroid.

8.3.4. Orientation Related Features

The particle orientation with respect to the light direction matters since the light interacts with different sections of the particle differently. To express the orientation of the shape, overall and directional features are used. The orientation angle, γ is the angle of the principal axis of the minimum bounding rectangle with the x-axis using the scaled moments in equation (8.10) [247]. γ gives an idea of the general shape.

$$\gamma = \frac{1}{2} \tan^{-1} \left[\frac{2\eta_{11}}{\eta_{20} - \eta_{02}} \right] \quad (8.17)$$

With a more detailed analysis, local features of the shapes can be identified. For example, a directional perimeter term can be developed to obtain local extensions of the shapes in the vicinity of specific directions. For this feature to be calculated, at least one of the vertices should be within the predefined region. Otherwise, the feature is zero. The proposed feature is formulated as follows:

$$\begin{aligned} \rho_{+x} &= \begin{cases} \frac{1}{P} \sum P(I_1, \{V_i\}, I_2), & -\theta_{max} < \theta_i < \theta_{max} \text{ AND } \alpha_i < \alpha_{max} \\ 0, & \text{otherwise} \end{cases} \\ \rho_{+y} &= \begin{cases} \frac{1}{P} \sum P(I_1, \{V_i\}, I_2), & \pi/2 - \theta_{max} < \theta_i < \pi/2 + \theta_{max} \\ 0, & \text{otherwise} \end{cases} \\ \rho_{-x} &= \begin{cases} \frac{1}{P} \sum P(I_1, \{V_i\}, I_2), & \pi - \theta_{max} < \theta_i < \pi + \theta_{max} \\ 0, & \text{otherwise} \end{cases} \\ \rho_{-y} &= \begin{cases} \frac{1}{P} \sum P(I_1, \{V_i\}, I_2), & 3\pi/2 - \theta_{max} < \theta_i < 3\pi/2 + \theta_{max} \\ 0, & \text{otherwise} \end{cases} \end{aligned} \quad (8.18)$$

where $P(I_1, \{V_i\}, I_2)$ is the perimeter of the segment connecting the points I_1 and I_2 where at least one vertex is located in between. θ_{max} designates the allowable half angle between

points I_1 and I_2 and the principal axes. α_{max} is the maximum interior angle that a vertex can have to be considered *elongated*.

8.3.5. Sharpness Related features

Similar to the directional perimeter, directional sharpness measures the local properties of the shape. Sharp edges are identified by vertices with an interior angle smaller than a specific value. If a sharp edge is near the four main axes, the vertex's radial position divided by the perimeter is calculated as the directional sharpness along that axis.

The proposed feature can be formulated as follows:

$$\begin{aligned}
 s_{+x} &= \begin{cases} \frac{1}{P} \sum r_i, & -\theta_{max} < \theta_i < \theta_{max} \text{ AND } \alpha_i < \alpha_{max} \\ 0, & \text{otherwise} \end{cases} \\
 s_{+y} &= \begin{cases} \frac{1}{P} \sum r_i, & \pi/2 - \theta_{max} < \theta_i < \pi/2 + \theta_{max} \text{ AND } \alpha_i < \alpha_{max} \\ 0, & \text{otherwise} \end{cases} \\
 s_{-x} &= \begin{cases} \frac{1}{P} \sum r_i, & \pi - \theta_{max} < \theta_i < \pi + \theta_{max} \text{ AND } \alpha_i < \alpha_{max} \\ 0, & \text{otherwise} \end{cases} \\
 s_{-y} &= \begin{cases} \frac{1}{P} \sum r_i, & 3\pi/2 - \theta_{max} < \theta_i < 3\pi/2 + \theta_{max} \text{ AND } \alpha_i < \alpha_{max} \\ 0, & \text{otherwise} \end{cases}
 \end{aligned} \tag{8.19}$$

where α_i is the interior angle of the i th vertex.

8.3.6. Convexity Related Features

Convexity is a measure of the curvature of the shape. If none of the interior angles of the shape is smaller than π , then the shape is convex; otherwise, it is nonconvex. The convexity of a closed shape is measurable using bounding rectangles [248]. In this approach, the perimeter of the bounding rectangle is compared to the *projected perimeter*

of a polygon, or *city block* perimeter. For any shape, equality holds only for convex shapes in the following expression:

$$P_1(\mathcal{S}, \delta) \geq 2(L_{\delta,x} + L_{\delta,y}), \quad (8.20)$$

where $P_1(\mathcal{S}, \delta)$ denotes projected perimeter of a shape, \mathcal{S} tilted with an angle δ . This quantity is equivalent to the expression below:

$$P_1(\mathcal{S}, \delta) = \sum_{i=1}^{N_v-1} (x_{i+1} - x_i) + (y_{i+1} - y_i), \quad (8.21)$$

where (x_i, y_i) is the coordinates of the i th vertex. Using equation (8.20), a convexity metric can be formulated as follows:

$$c = \min_{\alpha \in [0, 2\pi)} \frac{2(L_{\delta,x} + L_{\delta,y})}{P_1(\mathcal{S}, \delta)}. \quad (8.22)$$

$c < 1$ for concave and $c = 1$ for convex shapes. Directional convexity is calculated by dividing the radial position of the shape boundary along an axis to the mean radial position near the same axis using Jensen's inequality. According to this inequality, in an interval, \mathcal{J} , for a set x_1, x_2, \dots, x_N :

$$f\left(\sum_{n=1}^N x_n\right) - \sum_{n=1}^N f(x_n) \begin{cases} < 0, & \text{if convex} \\ = 0, & \text{if collinear} \\ > 0, & \text{if concave} \end{cases} \quad (8.23)$$

The relationship above can be translated into a directional convexity feature by focusing on the vertex coordinates. Along x direction, the comparison can be made by y coordinates and vice versa. An additional change is made to the first term by using the coordinate value when the other coordinate (x when y is used) is zero. Selecting an angular region $\pm\pi/4$ around each axis, the following expressions are formulated:

$$\begin{aligned}
c_{+x} &= \frac{x_0}{x} - 1 & \{-\pi/4 < \theta_j \leq \pi/4 \mid j = 1, \dots, n_d\} \\
c_{+y} &= \frac{y_0}{y} - 1 & \{\pi/4 < \theta_j \leq 3\pi/4 \mid j = 1, \dots, n_d\} \\
c_{-x} &= \frac{x_0}{x} - 1 & \{3\pi/4 < \theta_j \leq 5\pi/4 \mid j = 1, \dots, n_d\} \\
c_{-y} &= \frac{y_0}{y} - 1 & \{5\pi/4 < \theta_j \leq 7\pi/4 \mid j = 1, \dots, n_d\}
\end{aligned} \tag{8.24}$$

where $x_0 = x(y = 0)$ and $y_0 = y(x = 0)$. θ_j is the angular position of the boundary point (x_j, y_j) (Figure 8.2).

8.3.7. Symmetry Related Features

Symmetry is calculated by comparing the intersected area of the original and mirrored (around the desired direction) shapes with the original area. A perfectly symmetric shape will have a score of 1; otherwise, it will be 0. Once the vertex coordinates of the intersected shape are found, the following expressions:

$$\begin{aligned}
\sigma_x &= \frac{A_{int,y}}{A} \\
\sigma_y &= \frac{A_{int,x}}{A}
\end{aligned} \tag{8.25}$$

where $A_{int,x}$ and $A_{int,y}$ are the areas of the intersected shape found by mirroring the shape along x and y directions, respectively.

In Table 8.1, the features explained above are summarized with their group and a brief description is provided for each feature.

Table 8.1. Summary of the features with their description.

	Feature	Description
Simple	N_v	Number of vertices
	p_n	Normalized perimeter
	A	Area
	ξ_e	Eccentricity
	ξ_c	Compactness
	ξ_r	Rectangularity
	ξ_α	Coverage angle from an observer far from the shape
Mom¹	ξ_v	The ratio of the visible vertices from an observer to N_v
	ϕ_1	1 st moment invariant
	ϕ_2	2 nd moment invariant
	ϕ_3	3 rd moment invariant
	$\phi_{e,1}$	1 st order elongation
Elongation	$\phi_{e,4}$	4 th order elongation
	l_y	The ratio of the perimeter of the bounding rectangle along x axis to P
	$\tau_{x,max}$	The ratio of the shape extends on the y axis to the maximum shape extend along any direction
	$\tau_{y,max}$	The ratio of the shape extends on the x axis to the maximum shape extend along any direction
	$\tau_{x,avg}$	The ratio of the shape extends on the y axis to the average shape extend along any direction
Orientation	$\tau_{y,avg}$	The ratio of the shape extends on the x axis to the average shape extend along any direction
	γ	Orientation angle
	ρ_{+x}	Directional perimeter in the vicinity of +x direction
	ρ_{+y}	Directional perimeter in the vicinity of +y direction
	ρ_{-x}	Directional perimeter in the vicinity of -x direction
Sharpness	ρ_{-y}	Directional perimeter in the vicinity of -y direction
	s_{+x}	Directional sharpness in the vicinity of +x direction
	s_{+y}	Directional sharpness in the vicinity of +y direction
	s_{-x}	Directional sharpness in the vicinity of -x direction
	s_{-y}	Directional sharpness in the vicinity of -y direction
Convexity	c	Convexity of the overall shape
	c_{+x}	Directional sharpness in the vicinity of +x direction
	c_{+y}	Directional sharpness in the vicinity of +y direction
	c_{-x}	Directional sharpness in the vicinity of -x direction
	c_{-y}	Directional sharpness in the vicinity of -y direction
Sym²	σ_x	Symmetry around x direction
	σ_y	Symmetry around y direction

¹Momentum, ² Symmetry

8.4. Dataset

A dataset of 8,230 data points is generated, each representing a random polygon nanoparticle and computed independent variables (features), as explained previously. The dependent variable (i.e., target) is obtained from the computational simulations. We decided to use the following normalized transformed quantity as the regression target:

$$\text{Target} \equiv \log(C_{scat}/A) \quad (8.26)$$

where C_{scat} is the scattering cross section and A is the physical area. C_{scat}/A is also known as the scattering coefficient. Using the logarithm of the scattering coefficient provides a normalized target distribution. The distributions of different target options are provided in Figure 8.5. The scatter plots of individual features with respect to the target are presented in Figure 8.6. Each feature correlates with the target differently, where in some cases, the correlation is very weak. Nevertheless, the cumulative effect of features should not be discarded. A summary of the data is provided in Table 8.2. The intercorrelation of the features is presented using the absolute values of the Pearson formulation. Additionally, a hierarchical clustering approach is used to investigate the relationship between the features and presented together with the correlation plot in Figure 8.7.

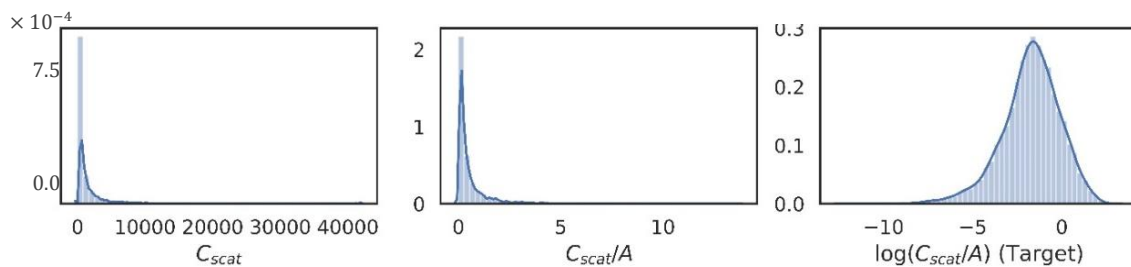


Figure 8.5. Histograms of different options for the target.

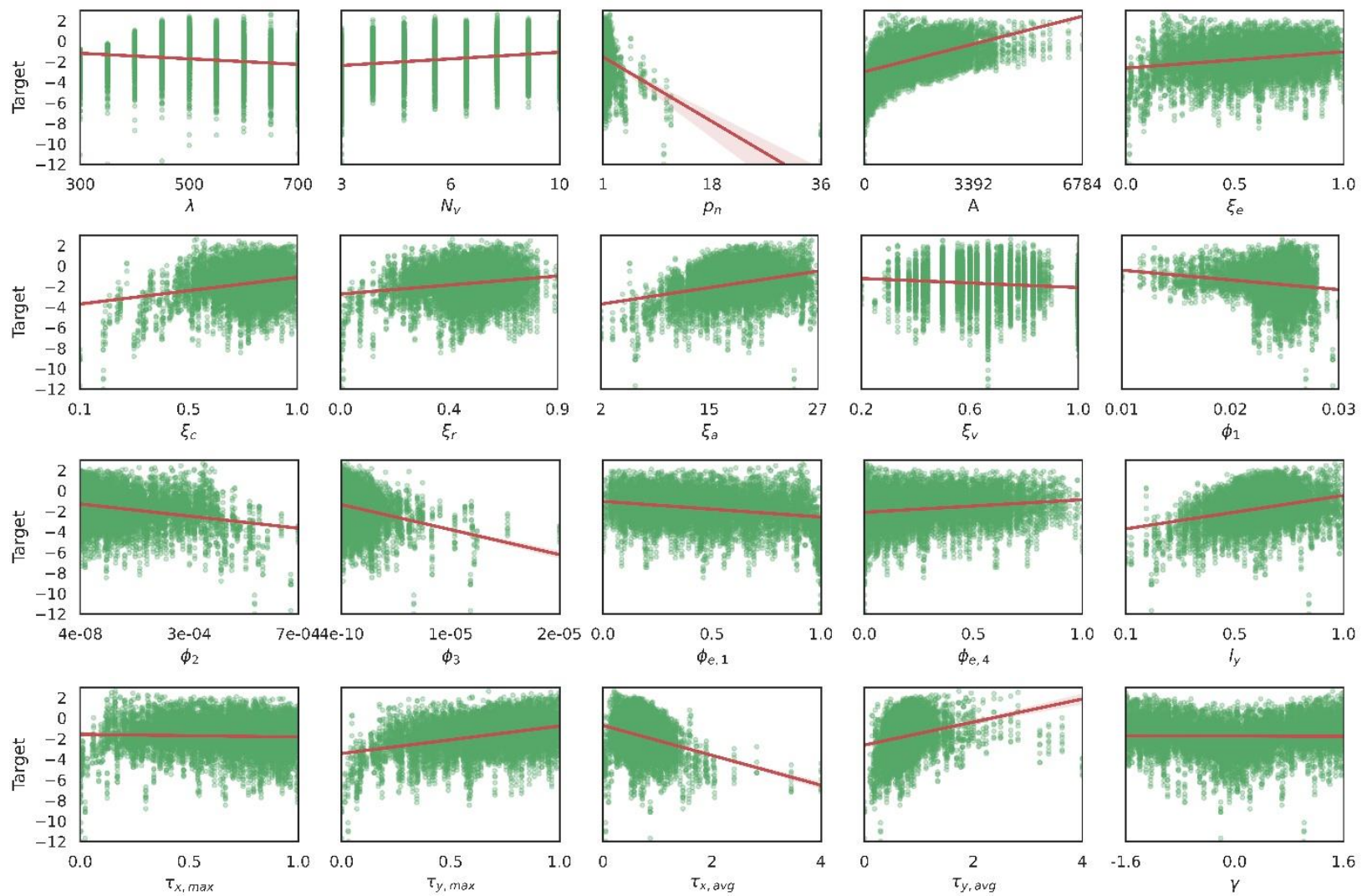


Figure 8.6. Scatter plots of target with each feature.

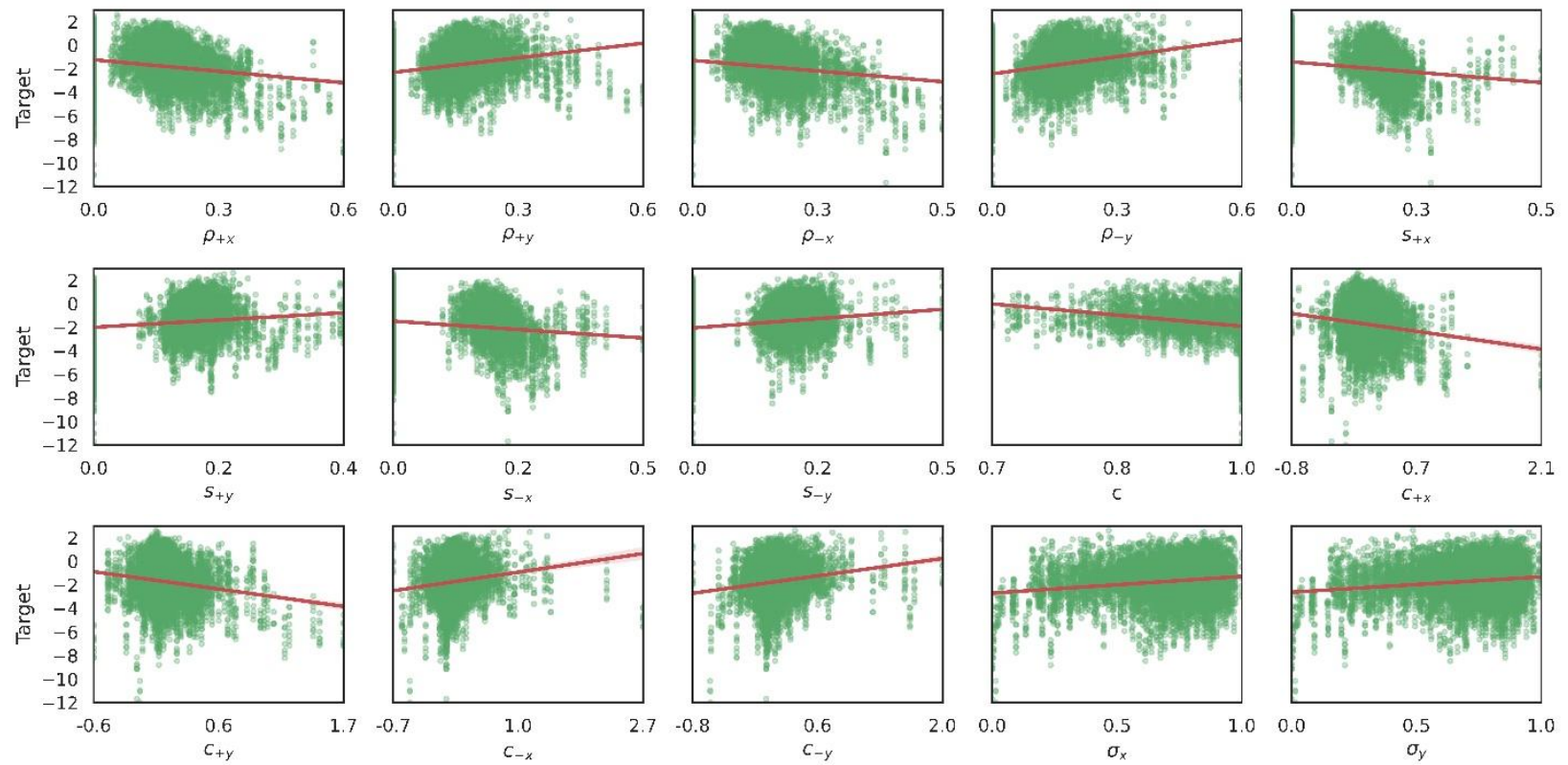


Figure 8.6 Continued.

Table 8.2. Summary of the dataset. Mean, standard deviation, minimum and maximum values of the features and the target.

	Feature	mean	std	min	max
Simple	λ	503.1	127.9	300.0	700.0
	N_v	6.48	2.25	3.00	10.00
	p_n	1.551	1.314	1.034	36.226
	A	1569.1	1044.2	0.1	6784.3
	ξ_e	0.559	0.224	0.007	0.985
	ξ_c	0.758	0.133	0.093	0.968
	ξ_r	0.505	0.141	0.014	0.870
	ξ_a	18.2	4.2	2.6	27.9
	ξ_v	0.666	0.166	0.200	1.000
Mom.¹	ϕ_1	0.020	0.002	0.008	0.026
	ϕ_2	1.25×10^{-4}	1.30×10^{-4}	4.45×10^{-8}	6.62×10^{-4}
	ϕ_3	1.83×10^{-6}	2.20×10^{-6}	3.53×10^{-10}	2.35×10^{-5}
Elongation	$\phi_{e,1}$	0.465	0.261	0.009	0.999
	$\phi_{e,4}$	0.284	0.227	1.07×10^{-6}	0.954
	l_y	0.637	0.148	0.096	0.986
	$\tau_{x,max}$	0.639	0.234	0.026	1.000
	$\tau_{y,max}$	0.642	0.226	0.010	1.000
	$\tau_{x,avg}$	0.995	0.331	0.324	4.137
	$\tau_{y,avg}$	1.010	0.362	0.251	4.122
Orientation	γ	-0.014	0.923	-1.566	1.571
	ρ_{+x}	0.146	0.097	0.000	0.572
	ρ_{+y}	0.144	0.103	0.000	0.625
	ρ_{-x}	0.134	0.102	0.000	0.541
	ρ_{-y}	0.146	0.100	0.000	0.610
Sharpness	s_{+x}	0.094	0.103	0.000	0.517
	s_{+y}	0.096	0.104	0.000	0.447
	s_{-x}	0.084	0.101	0.000	0.461
	s_{-y}	0.093	0.102	0.000	0.459
Convexity	c	0.968	0.061	0.655	1.000
	c_{+x}	0.106	0.224	-0.764	2.136
	c_{+y}	0.092	0.243	-0.735	2.669
	c_{-x}	0.082	0.215	-0.585	1.725
	c_{-y}	0.091	0.239	-0.839	1.968
Sym.²	σ_x	0.678	0.193	0.018	0.984
	σ_y	0.683	0.195	0.018	0.991
	Target	-1.739	1.640	-11.986	2.618

¹Momentum, ²Symmetry

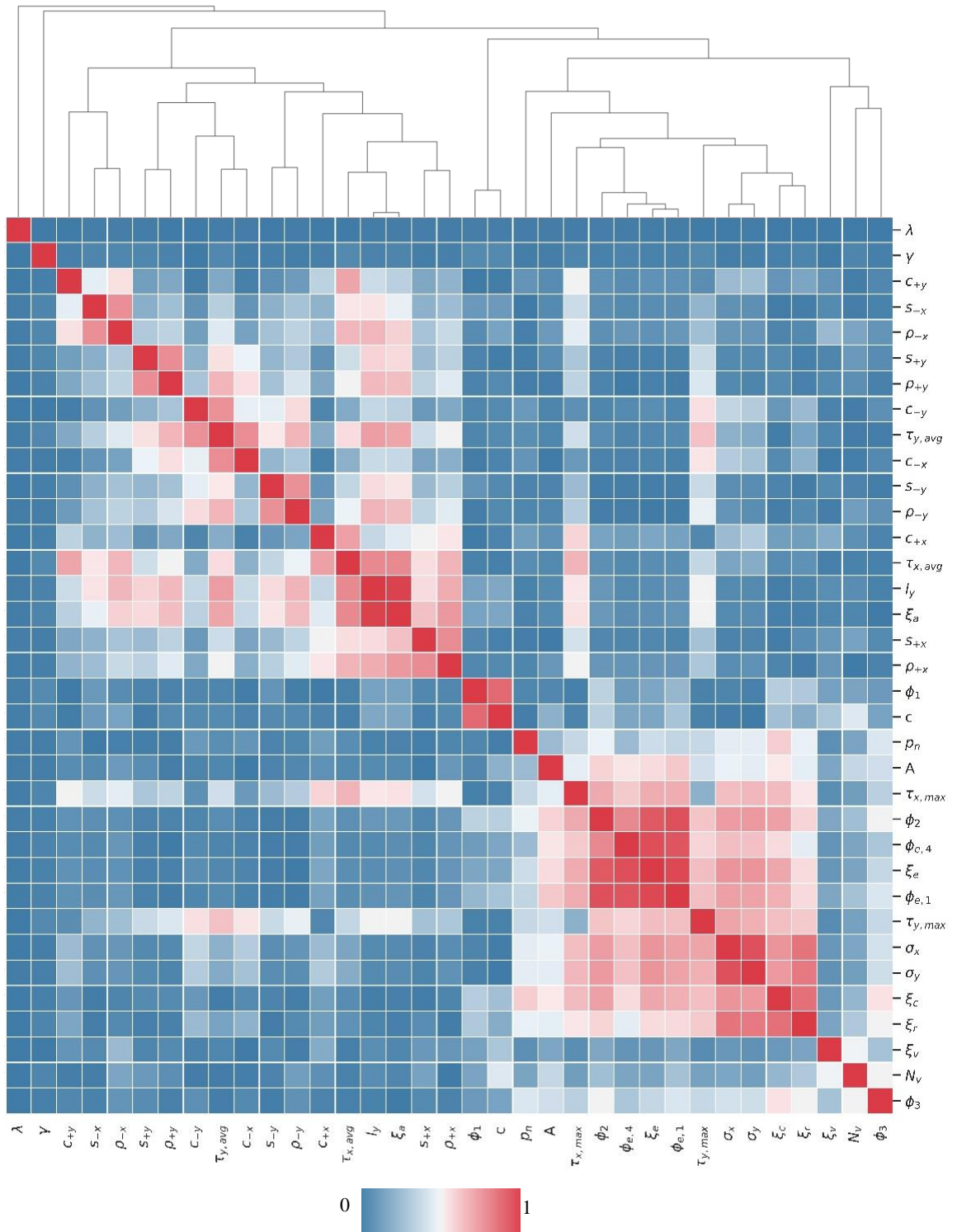


Figure 8.7. Analysis of the dataset using hierarchical clustering and absolute correlation matrix.

From Figure 8.7, wavelength λ is the least correlated feature with the others, as expected. The reason wavelength is also included as a feature is to reduce the computational cost of prediction. Although a multi-output regression could also be considered with scattering at each selected wavelength as one output, this would require more data points, thus increasing the cost (discussed in Chapter 6). Using wavelength as input increases input size by 1 but decreases the number of outputs from the number of wavelengths in consideration to 1.

The other feature at the outermost leaves of the hierarchy is the orientation angle, γ . As seen in Figure 8.6, the relationship between γ and the target has a V-shape, contrary to the other features. Although the number of vertices, N_v is also expected to have a small correlation with the rest of the features, it is connected with 3rd moment invariant, ϕ_3 , in the cluster and has a nonzero, yet small, correlation with a few more features, such as convexity, c , and the ratio of the visible vertices from an observer to the total number of vertices, ξ_v . The convexity, c and 1st moment invariant, ϕ_1 are one of the highly correlated feature pairs.

The features belong to one of two main clusters. The first cluster involves the orientation, sharpness and convexity related directional features and the ratio of the shape extent in x and y directions to the average. The second cluster involves the simple features, moment based features and sharpness related features. In other words, the first cluster describes the specific regions of the shapes. In contrast, the second cluster explains the general characteristics of a shape.

8.5. Results and Discussion

8.5.1. Training Results

The summary of the training results is presented in Table 8.3. The training and validation set errors are shown with the coefficients of determination, or *R-squared* (R^2). Figure 8.8 shows the scatter plots of the target and predicted outputs for each predictor. The linear regression algorithm has the highest error and lowest R^2 , as expected since the input-output relationship is highly nonlinear. Regression trees show an R^2 larger than 0.85, yet it is significantly smaller than those of XGBoost and neural networks. One of the possible reasons for the poorer performance of regression trees is overfitting. As the tree structure gets complex, the generalization capability of the regression trees reduces. XGBoost and neural networks perform the best for predicting the output according to the validation error. Although the smaller training error of XGBoost compared to neural networks suggests overfitting, the inherent regularization of XGBoost results in a small validation error. On the other hand, neural networks also perform similarly on the validation set and the larger training error is due to the Bayesian regularization scheme employed during neural network training. As a result of the training, XGBoost and neural networks can be considered the best predictors.

Table 8.3. Summary of the performances of fitting methods

Method	Training		Validation	
	MSE	R^2	MSE	R^2
Regression Trees	0.00558	0.997	0.355855	0.866
XGBoost Regression	4.07×10^{-7}	1.000	0.127011	0.952
Neural Networks	0.075895	0.972	0.12748	0.952
Linear Regression	1.247262	0.539	1.312303	0.506

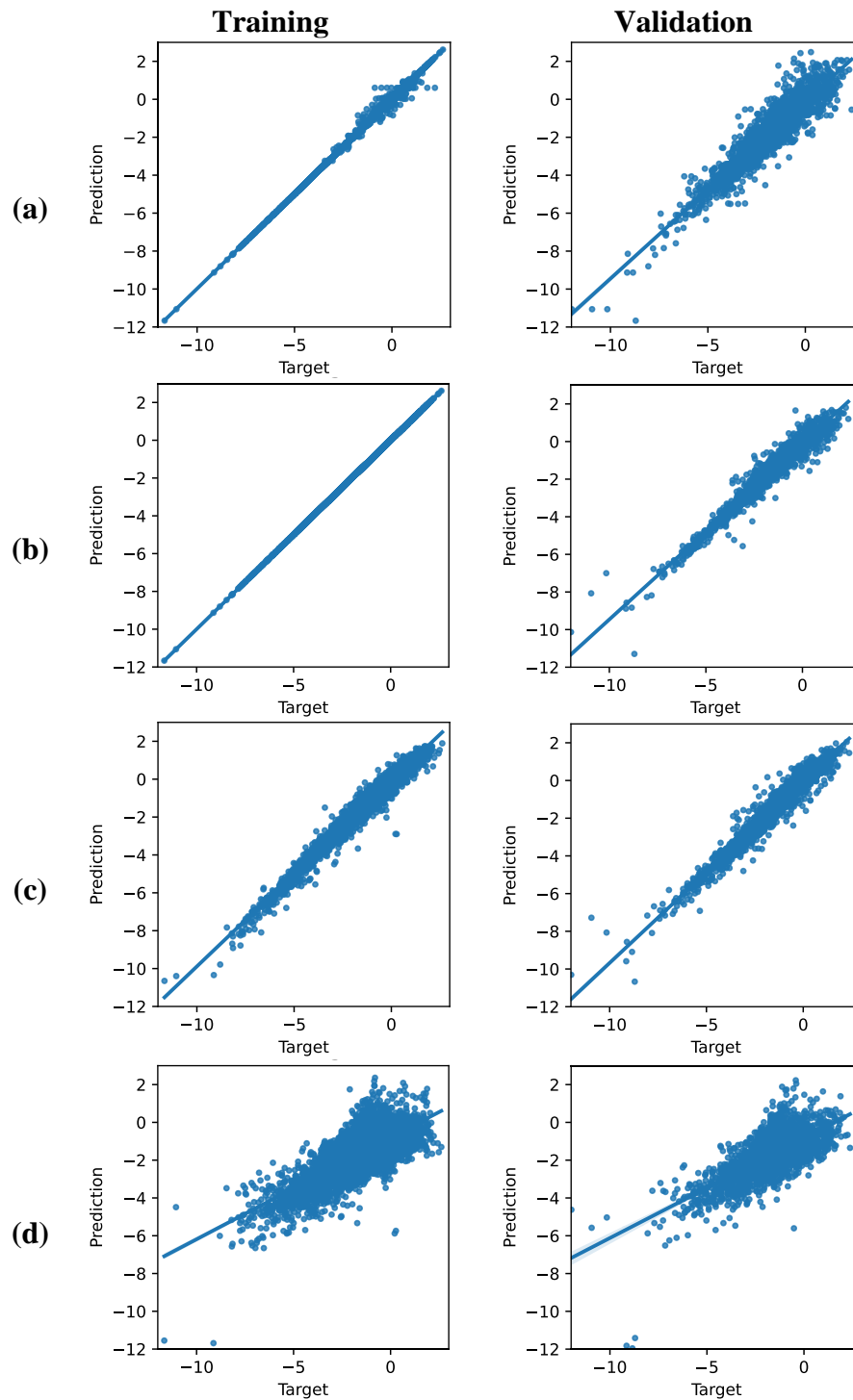


Figure 8.8. Comparison of the target and predicted outputs by (a) Regression Trees, (b) XGBoost Regression, (c) Neural Networks, (d) Linear Regression. Left: Training set, Right: Validation set.

8.5.2. Test Results

The instances in the test dataset are entirely new to the predictors; thus, the test results show the real-world performance of the predictors. The previous section demonstrates that XGBoost and neural networks are the best performing predictors and used for the test cases in this section. Figure 8.9 shows the comparison of the target and the predictions obtained by XGBoost (Figure 8.9a) and neural networks (Figure 8.9b). The error rates and R^2 values of these predictors are very close, which is in agreement with the training and validation results.

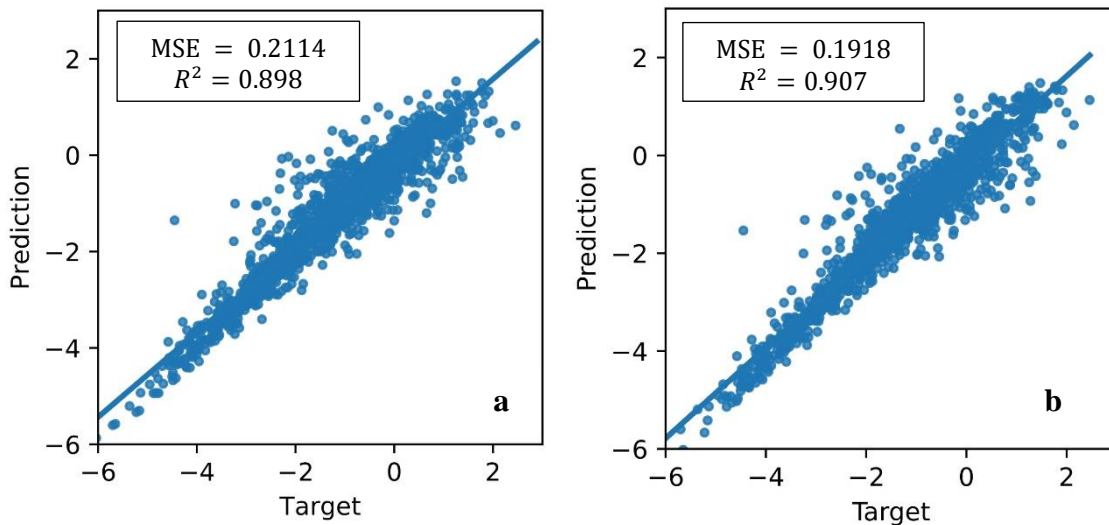


Figure 8.9. Comparison of target and predicted data for the test set. (a) XGBoost, (b) neural networks regression.

In Figure 8.9, comparison of the scattering cross section, C_s over the wavelength range in consideration is shown for three different cases. These examples are kept at a limited

number for the sake of brevity. Note that in these plots, the target, log scattering efficiency ($\log C_s/A$), is converted to the scattering cross section, C_s , for visualization purpose.

The discrepancy between the target and the predictions is more visible at the peak locations of the scattering. It is expected to see discrepancy at large scattering values because data with large output is slightly less than the rest of the data. One possible approach to improve the fit at the peak locations is to create a supplementary predictor for predicting peak locations and peak values of each case. This approach can work as a refinement step of the prediction.

8.6. Conclusion

In this study, the optical characteristics of nanoparticles with arbitrary shapes are modeled using data driven techniques. The arbitrary shapes, randomly drawn polygons, are characterized by the predictive shape descriptors, describing unique features of each shape. These features include area, eccentricity, as well as sharpness and convexity related features, and more. These predictive shape features are used to estimate the optical scattering, log scattering efficiency. Among different techniques, XGBoost and neural networks regression perform best in terms of the validation error. The test set also shows that the predictors perform well with the completely new (test) cases.

Although there are discrepancies between the target and the predictions, the general trend of the scattering is predicted closely. The peak locations are estimated even though the value is not always matched. The fit of the predictive models can be further improved by employing an adaptive sampling, where new training points are added from the high-error regions.

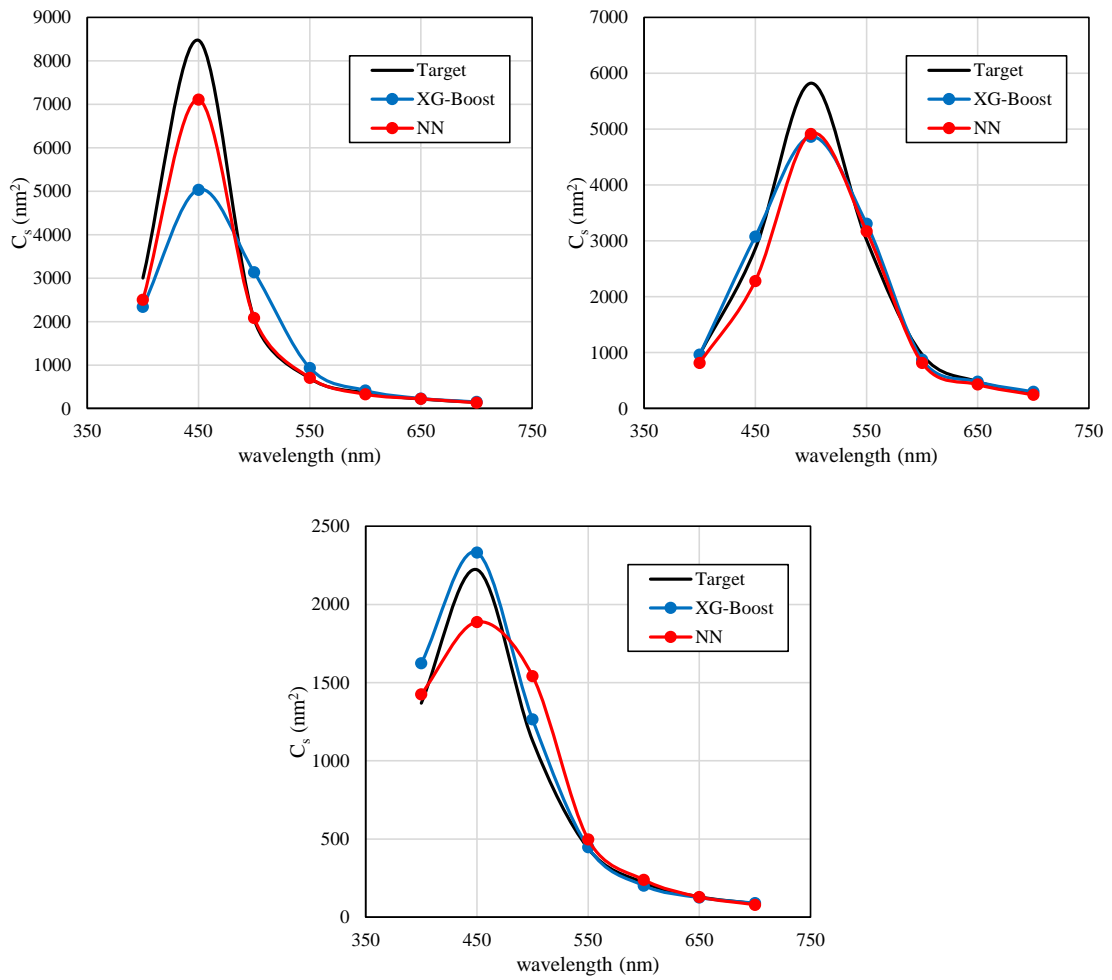


Figure 8.9. Examples of the comparison of the target and predictions from XGBoost and neural networks over the wavelength spectrum.

9. SUMMARY AND CONCLUSIONS

9.1. Summary of the Dissertations

In this dissertation, a numerical characterization and optimization framework is proposed for thin film solar cell design based on learning based techniques and evolutionary nonparametric shape optimization. The design of various solar cell configurations with different objective functions is investigated.

In Chapter 4, a learning based optimization process is conducted for maximum optical enhancement. Optical enhancement is defined as the ratio of the number of absorbed photons by plasmonic and bare solar cells, respectively. The summary of the key findings is listed below.

- Despite significant electric field enhancement near the band edge, the absorption is not significantly high due to of small values of the imaginary part of the refractive index. Yet, near edge absorption by plasmonic cells is still much larger than the bare.
- Although not stated explicitly, the enhancement factor favors shorter thicknesses for absorber; therefore, efficient electrical transport is expected even though electrical simulations are not performed.
- The comparison of plasmonic and random (initial) design results justifies the necessity of numerical optimization.
- The electric field intensifies around the sharper edges of nanoparticles.

In Chapter 5, a similar optimization procedure to one in Chapter 4 is employed to find the maximum external quantum efficiency. The key results of this study are summarized below.

- The approximate external quantum efficiency, developed by the material properties (i.e., diffusion length) and the absorptivity, is validated with an experimental result from the literature. The proposed method matches the experiments closely for p-n junction semiconductors.
- The optimized design resulted in a better optical and electrical performance compared to the randomly selected initial design.

Chapter 6 improves the optimization methodology in Chapter 5 by introducing the knowledge transfer concept to design optimization. The knowledge is transferred among similar tasks (i.e., different material combinations). Two different approaches are proposed: neural network based transfer optimization and Gaussian process based Bayesian transfer optimization. The summary of key findings is listed below.

- The knowledge transfer is utilized via shared layers in neural networks, and a similarity weighted common surface in Gaussian process.
- The knowledge transfer improves the accuracy of the surrogate neural network.
- The effect of the negative transfer is discussed using neural networks.
- The similarity metric provides an easy-to-use way to quantify similarity among the tasks.
- Overall, neural network based transfer optimization is found to be more accurate and faster because of using wavelength as an input.

In Chapter 7, a free form nanoparticle is designed for the maximum scattering cross section. The nonparametric design is performed by a density based topology optimization and filtering techniques, such as image morphology methods. The key results of this study are listed below:

- The optimization objectives are 2-35 times higher compared to known shapes, such as cube, hexagon, hexagram, and sphere.
- Spectral cross sections are 1-10 times higher compared to the known shapes.
- A checkerboard control scheme is proposed in addition to the filtering techniques, providing realistic and efficient designs.

In Chapter 8, the scattering by arbitrarily shaped nanoparticles is modeled using predictive methods. The arbitrary shapes, randomly drawn polygons, are characterized by the predictive shape features, describing unique features of each shape. These predictive shape features are used to estimate the optical scattering using machine learning methods, such as neural networks, XGBoost regression and regression trees. The key results of this study are listed below:

- The correlation between the features is illustrated and discussed using hierarchical clustering.
- XGBoost and neural networks regression perform best with a 95% validation error.
- Testing error is 90%, which shows that the predictive methods generalize well with the new data points.
- The comparison between the predictions and simulations are illustrated for several test cases. Although there are discrepancies between the target and the predictions,

the general trend of the scattering, i.e., the peak locations and bandwidth, is predicted closely.

9.2. Suggestions for Future Work

This section details suggestions for possible research directions related to the content of this work.

9.2.1. Experimental Verification of the Numerical Results

Experimental validation is an integral part of the material design. The optimized solar cell structure in this study is suggested to be fabricated for uncertainty analysis. In a fabricated sample, various sources of uncertainty exist. For instance, variations in the geometry can occur as a result of fabrication uncertainties. Roughness measurements via atomic force microscopy (AFM) can be convenient to minimize uncertainty; yet, the roughness values should be incorporated in the optimization procedure. Another source of uncertainty can be the nanoparticle nucleation and growth since the geometry control of a particle remains to be a challenge. This study and other researchers in the literature demonstrated the importance of the nanoparticle shape. Therefore, the uncertainties in the fabricated nanoparticles should also be considered in the design. Using numerical optimization, coupled with fabrication, can yield a robust framework of solar cell design.

9.2.2. Optoelectrical Modeling and Optimization of Plasmonic Solar Cells

The proposed EQE model in this study is analytical and based on simplifications, such as negligible surface recombination. Additionally, the bulk recombination is not distinguished but presented as a single expression. On the other hand, several factors have

possible effects on the electrical performance of solar cells, such as doping profile in the solar cell and electrical properties of the materials, i.e., mobility. The proposed EQE model will be verified using computational methods, i.e., drift-diffusion equations.

A detailed recombination modeling for nanostructured and plasmonic solar cells can yield a comprehensive analysis, and PCE can be targeted directly. Developing an approximate model that can capture the effects of nanostructures can also increase the computation speed, which remains to be a challenge.

9.2.3. Scattering Prediction Using Geometric Features Based on Adaptive Sampling

In Chapters 4 and 7, the importance of nanoparticle shape in radiative applications is demonstrated. Chapter 8 is devoted to the prediction of nanoparticle scattering using predictive geometric features. This study can be extended to improve the fit using adaptive sampling strategies and consider different scenarios in optical problems. The suggestions are elaborated below:

- i. *Adaptive sampling*: A more informed dataset construction procedure can improve fit performance with a smaller number of data. One of the possible approaches is using the validation error for picking a new training instance. If certain regions are not represented compared to the others, the validation error in these regions is expected to be large. Adding new data near high error regions can improve the predictor's performance. Once the instances in the validation set with a large error are identified, the new data can be added near the larger-validation-error regions based on error based probability or above the desired threshold.

ii. *Different scenarios*: The studies in Chapters 7 and Chapter 8 focus on shape-dependent scattering by considering isolated particles in the vacuum. However, in most applications, the effect of nearby nanoparticles is not negligible and periodically located particles demonstrate different radiative responses than isolated particles. Additionally, the surrounding media affect the optical response of particles, such as shifting peak point(s), altering the scattering strength. Considering these scenarios can enable more reliable predictions for real world applications, such as thin film solar cells.

REFERENCES

- [1] Howell JR, Siegel R, Menguc MP. Thermal Radiation Heat Transfer. 5th ed. Taylor & Francis; 2010. doi:10.1017/CBO9781107415324.004.
- [2] Energy and CO₂ emissions in the OECD n.d. <http://www.iea.org/classicstats/> (accessed July 30, 2018).
- [3] Sources of Greenhouse Gas Emissions n.d. <https://www.epa.gov/ghgemissions/sources-greenhouse-gas-emissions> (accessed July 30, 2018).
- [4] Power Costs 2018 n.d. <https://www.irena.org/>.
- [5] National Renewable Energy Laboratory. Renewable Electricity Generation and Storage Technologies Futures Study. NREL 2012;2. doi:NREL/TP-6A20-52409-2.
- [6] Fu R, Chung D, Lowder T, Feldman D, Ardani K, Fu R, et al. U . S . Solar Photovoltaic System Cost Benchmark : Q1 2016 U . S . Solar Photovoltaic System Cost Benchmark : Q1 2016. NREL 2016. <https://www.nrel.gov/docs/fy17osti/68925.pdf> (accessed October 20, 2017).
- [7] Chopra KL, Paulson PD, Dutta V. Thin-film solar cells: an overview. *Prog Photovoltaics Res Appl* 2004;12:69–92. doi:10.1002/pip.541.
- [8] Sugawara E, Nikaido H. Annual Energy Outlook 2020 with Projections to 2050. 2019. doi:10.1128/AAC.03728-14.
- [9] Green MA. The Path to 25% Silicon Solar Cell Efficiency: History of Silicon Cell Evolution. *Prog Photovolt Res Appl* 2009;17:183–9.
- [10] Best Research-Cell Efficiencies n.d. <https://www.nrel.gov/pv/cell-efficiency.html> (accessed July 26, 2020).
- [11] Ferry VE, Verschuuren MA, Li HBT, Verhagen E, Walters RJ, Schropp REI, et al. Light trapping in ultrathin plasmonic solar cells. *Opt Express* 2010;18:A237. doi:10.1364/OE.18.00A237.
- [12] Ibn-Mohammed T, Koh SCL, Reaney IM, Acquaye A, Schileo G, Mustapha KB, et al. Perovskite solar cells: An integrated hybrid lifecycle assessment and review in comparison with other photovoltaic technologies. *Renew Sustain Energy Rev* 2017;80:1321–44. doi:10.1016/j.rser.2017.05.095.
- [13] Grätzel M. Dye-sensitized solar cells. *J Photochem Photobiol C Photochem Rev* 2003;4:145–53. doi:10.1016/S1389-5567(03)00026-1.
- [14] Nazeeruddin MK, Baranoff E, Grätzel M. Dye-sensitized solar cells: A brief overview. *Sol Energy* 2011;85:1172–8. doi:10.1016/j.solener.2011.01.018.
- [15] Heo JH, Im SH, Noh JH, Mandal TN, Lim CS, Chang JA, et al. Efficient inorganic-organic hybrid heterojunction solar cells containing perovskite compound and

- polymeric hole conductors. *Nat Photonics* 2013;7:486–91. doi:10.1038/nphoton.2013.80.
- [16] Kojima A, Teshima K, Shirai Y, Miyasaka T. Organometal Halide Perovskites as Visible- Light Sensitizers for Photovoltaic Cells. *J Am Chem Soc* 2009;131:6050–1. doi:10.1021/ja809598r.
- [17] Zhang W, Saliba M, Stranks SD, Sun Y, Shi X, Wiesner U, et al. Enhancement of perovskite-based solar cells employing core-shell metal nanoparticles. *Nano Lett* 2013;13:4505–10. doi:10.1021/nl4024287.
- [18] Marinova N, Valero S, Delgado JL. Organic and perovskite solar cells: Working principles, materials and interfaces. *J Colloid Interface Sci* 2017;488:373–89. doi:10.1016/j.jcis.2016.11.021.
- [19] Fan R, Wang L, Chen Y, Zheng G, Li L, Li Z, et al. Tailored Au@TiO₂ nanostructures for the plasmonic effect in planar perovskite solar cells. *J Mater Chem A* 2017;5:12034–42. doi:10.1039/C7TA02937C.
- [20] Service RF. Perovskite Solar Cells Keep On Surging. *Science* (80-) 2014;344:458. doi:10.1126/science.344.6183.458.
- [21] Saliba M, Zhang W, Burlakov VM, Stranks SD, Sun Y, Ball JM, et al. Plasmonic-Induced Photon Recycling in Metal Halide Perovskite Solar Cells. *Adv Funct Mater* 2015;25:5038–46. doi:10.1002/adfm.201500669.
- [22] Sariciftci NS, Braun D, Zhang C, Srdanov VI, Heeger AJ, Stucky G, et al. Semiconducting polymer-buckminsterfullerene heterojunctions: Diodes, photodiodes, and photovoltaic cells. *Appl Phys Lett* 1993;62:585–7. doi:10.1063/1.108863.
- [23] Sariciftci NS, Smilowitz L, Heeger AJ, Wudl F. Photoinduced electron transfer from a conducting polymer to buckminsterfullerene. *Science* (80-) 1992;258:1474–6. doi:10.1126/science.258.5087.1474.
- [24] Krebs FC. Fabrication and processing of polymer solar cells: A review of printing and coating techniques. *Sol Energy Mater Sol Cells* 2009;93:394–412. doi:10.1016/j.solmat.2008.10.004.
- [25] Ameri T, Dennler G, Lungenschmied C, Brabec CJ. Organic tandem solar cells: A review. *Energy Environ Sci* 2009;2:347–63. doi:10.1039/b817952b.
- [26] Gunes S, Neugebauer H, Sariciftci NS. Conjugated Polymer-Based Organic Solar Cells 2007:1324–38. doi:10.1021/cr050149z.
- [27] Notarianni M, Vernon K, Chou A, Aljada M, Liu J, Motta N. Plasmonic effect of gold nanoparticles in organic solar cells. *Sol Energy* 2014;106:23–37. doi:10.1016/j.solener.2013.09.026.
- [28] Zhou H, Zhang Y, Mai CK, Collins SD, Nguyen TQ, Bazan GC, et al. Conductive conjugated polyelectrolyte as hole-transporting layer for organic bulk heterojunction solar cells. *Adv Mater* 2014;26:780–5.

doi:10.1002/adma.201302845.

- [29] Lattante S. Electron and Hole Transport Layers: Their Use in Inverted Bulk Heterojunction Polymer Solar Cells. *Electronics* 2014;3:132–64. doi:10.3390/electronics3010132.
- [30] Taflove A. *Computational Electrodynamics*. Artech House, Norwood, MA 1998. doi:10.1515/9783110809824.v.
- [31] Belghachi A. Detailed analysis of surface recombination in crystalline silicon solar cells. 2013 Int. Renew. Sustain. Energy Conf., 2013, p. 161–6. doi:10.1109/IRSEC.2013.6529729.
- [32] Tress W, Leo K, Riede M. Optimum mobility, contact properties, and open-circuit voltage of organic solar cells: A drift-diffusion simulation study. *Phys Rev B - Condens Matter Mater Phys* 2012;85:1–11. doi:10.1103/PhysRevB.85.155201.
- [33] Koster LJ a, Smits ECP, Mihailetschi VD, Blom PWM. Device model for the operation of polymer/fullerene bulk heterojunction solar cells. *Phys Rev B - Condens Matter Mater Phys* 2005;72:1–9. doi:10.1103/PhysRevB.72.085205.
- [34] Selberherr S. *Analysis and Simulation of Semiconductor Devices*. Springer-Verlag Wien; 1984. doi:10.1007/978-3-7091-8752-4.
- [35] Berginski M, Hüpkes J, Schulte M, Schöpe G, Stiebig H, Rech B, et al. The effect of front ZnO:Al surface texture and optical transparency on efficient light trapping in silicon thin-film solar cells. *J Appl Phys* 2007;101. doi:10.1063/1.2715554.
- [36] Thouti E, Sharma AK, Sardana SK, Komarala VK. Internal quantum efficiency analysis of plasmonic textured silicon solar cells: surface plasmon resonance and off-resonance effects. *J Phys D Appl Phys* 2014;47:425101. doi:10.1088/0022-3727/47/42/425101.
- [37] Ferrero A, Campos J, Pons A, Corrons A. New model for the internal quantum efficiency of photodiodes based on photocurrent analysis. *Appl Opt* 2005;44:208. doi:10.1364/AO.44.000208.
- [38] Dibb GFA, Muth M-A, Kirchartz T, Engmann S, Hoppe H, Gobsch G, et al. Influence of doping on charge carrier collection in normal and inverted geometry polymer:fullerene solar cells. *Sci Rep* 2013;3:3335. doi:10.1038/srep03335.
- [39] Xue J, Rand BP, Uchida S, Forrest SR. A hybrid planar-mixed molecular heterojunction photovoltaic cell. *Adv Mater* 2005;17:66–71. doi:10.1002/adma.200400617.
- [40] Xue J, Uchida S, Rand BP, Forrest SR. Asymmetric tandem organic photovoltaic cells with hybrid planar-mixed molecular heterojunctions. *Appl Phys Lett* 2004;85:5757–9. doi:10.1063/1.1829776.
- [41] Garcia-Belmonte G, Bisquert J. Open-circuit voltage limit caused by recombination through tail states in bulk heterojunction polymer-fullerene solar cells. *Appl Phys Lett* 2010;96:113301. doi:10.1063/1.3358121.

- [42] Repins I, Contreras MA, Egaas B, Dehart C, Scharf J, Perkins CL. 19.9 %-efficient ZnO/CdS/CuInGaSe₂ Solar Cell with 81.2% Fill Factor. *Prog Photovoltaics Res Appl* 2008;16:235–9. doi:10.1002/pip.
- [43] Zaban A, Greenshtein M, Bisquert J. Determination of the Electron Lifetime in Nanocrystalline Dye Solar Cells by Open-Circuit Voltage Decay Measurements. *ChemPhysChem* 2003;4:859–64. doi:10.1002/cphc.200200615.
- [44] Kniepert J, Roland S, Turbiez M, Bartesaghi D, Pe C, Neher D, et al. Competition between recombination and extraction of free charges determines the fill factor of organic solar cells. *Nat Commun* 2015;6:7083. doi:10.1038/ncomms8083.
- [45] Zhang Y, Dang X, Kim C, Nguyen T. Effect of Charge Recombination on the Fill Factor of Small Molecule Bulk Heterojunction Solar Cells. *Adv Energy Mater* 2011;1:610–7. doi:10.1002/aenm.201100040.
- [46] Mauer R, Howard IA. Effect of Nongeminate Recombination on Fill Factor. *Phys Chem Lett* 2010;1:3500–5. doi:10.1021/jz101458y.
- [47] Khenkin M V., Katz EA, Abate A, Bardizza G, Berry JJ, Brabec C, et al. Consensus statement for stability assessment and reporting for perovskite photovoltaics based on ISOS procedures. *Nat Energy* 2020;5:35–49. doi:10.1038/s41560-019-0529-5.
- [48] Ferry VE, Verschuur MA, Li HBT, Verhagen E, Walters RJ, Schropp REI, et al. Light trapping in ultrathin plasmonic solar cells. *Opt Express* 2010;18:A237. doi:10.1364/OE.18.00A237.
- [49] Campbell P, Green MA. Light trapping properties of pyramidally textured surfaces. *J Appl Phys* 1987;62:243–9. doi:10.1063/1.339189.
- [50] Wehrspohn RB, Sprafke AN. 3D photonic crystals for photon management in solar cells. *J Opt* 2012;14:024003. doi:10.1109/IPCon.2012.6358519.
- [51] Tang Z, Tress W, Inganäs O. Light trapping in thin film organic solar cells. *Mater Today* 2014;17:389–96. doi:10.1016/j.mattod.2014.05.008.
- [52] Wellenzohn M, Hainberger R. Light trapping by backside diffraction gratings in silicon solar cells revisited. *Opt Express* 2012;20:A20. doi:10.1364/OE.20.000A20.
- [53] Atwater HA, Polman A. Plasmonics for improved photovoltaic devices. *Nat Mater* 2010;9:865–865. doi:10.1038/nmat2866.
- [54] Tomchuk PM, Butenko D V. The nanoparticle shape's effect on the light scattering cross-section. *Surf Sci* 2012;606:1892–8. doi:10.1016/j.susc.2012.07.035.
- [55] Hulst HC. *Light Scattering by Small Particles*. Dover Publications Inc.; 1957.
- [56] Fan X, Zheng W, Singh DJ. Light scattering and surface plasmons on small spherical particles. *Light Sci Appl* 2014;3:1–14. doi:10.1038/lsa.2014.60.
- [57] Fabrizio E Di, Xie W, Zabala N, Aizpurua J, Maioli P, Huang Y. Surface plasmon resonance in gold nanoparticles : a review. *J Phys Condens Matter* 2017;29:203002.
- [58] Abadeer NS, Murphy CJ. Recent Progress in Cancer Thermal Therapy Using Gold

- Nanoparticles. *J Phys Chem C* 2016;120:4691–716. doi:10.1021/acs.jpcc.5b11232.
- [59] Shin JW, Cho DH, Moon J, Joo CW, Park SK, Lee J, et al. Random nano-structures as light extraction functionals for organic light-emitting diode applications. *Org Electron* 2014;15:196–202. doi:10.1016/j.orgel.2013.11.007.
- [60] Ferry VE, Polman A, Atwater HA. Modeling Light Trapping in Nanostructured Solar Cells. *ACS Nano* 2011;5:10055–64. doi:10.1021/nn203906t.
- [61] John S. Why trap light? *Nat Mater* 2012;11:997–9. doi:10.1038/nmat3503.
- [62] Hajimirza S, El Hitti G, Heltzel A, Howell J. Specification of micro-nanoscale radiative patterns using inverse analysis for increasing solar panel efficiency. *J Heat Transfer* 2012;134:1–8. doi:10.1115/1.4006209.
- [63] Wang Y, Wang P, Zhou X, Li C, Li H, Hu X, et al. Diffraction-Grated Perovskite Induced Highly Efficient Solar Cells through Nanophotonic Light Trapping. *Adv Energy Mater* 2018;8:1–8. doi:10.1002/aenm.201702960.
- [64] Van Lare MC, Polman A. Optimized Scattering Power Spectral Density of Photovoltaic Light-Trapping Patterns. *ACS Photonics* 2015;2:822–31. doi:10.1021/ph500449v.
- [65] Gramotnev DK, Bozhevolnyi SI. Plasmonics beyond the diffraction limit. *Nat Photonics* 2010;4:83–91. doi:10.1038/nphoton.2009.282.
- [66] Riso M, Cuevas M, Depine RA. Tunable plasmonic enhancement of light scattering and absorption in graphene-coated subwavelength wires. *J Opt* 2015;17:075001. doi:10.1088/2040-8978/17/7/075001.
- [67] Montgomery JM, Lee TW, Gray SK. Theory and modeling of light interactions with metallic nanostructures. *J Phys Condens Matter* 2008;20:323201. doi:10.1088/0953-8984/20/32/323201.
- [68] Kelly KL, Coronado E, Zhao LL, Schatz GC. The optical properties of metal nanoparticles: The influence of size, shape, and dielectric environment. *J Phys Chem B* 2003;107:668–77. doi:10.1021/jp026731y.
- [69] Nehl CL, Hafner JH. Shape-dependent plasmon resonances of gold nanoparticles. *J Mater Chem* 2008;18:2415–9. doi:10.1039/b714950f.
- [70] Jain PK, El-Sayed MA. Plasmonic coupling in noble metal nanostructures. *Chem Phys Lett* 2010;487:153–64. doi:10.1016/j.cplett.2010.01.062.
- [71] Barnes WL. Particle plasmons: Why shape matters. *Am J Phys* 2016;84:593–601. doi:10.1119/1.4948402.
- [72] Sheng X, Johnson SG, Michel J, Kimerling LC. Optimization-based design of surface textures for thin-film Si solar cells. *Opt Express* 2011;19:A841. doi:10.1063/1.94432.4.
- [73] Jovanov V, Palanchoke U, Magnus P, Stiebig H, Hüpkes J, Sichenugrist P, et al. Light trapping in periodically textured amorphous silicon thin film solar cells using

- realistic interface morphologies. *Opt Express* 2013;21:A595-606. doi:10.1364/OE.21.00A595.
- [74] Wang Z, Zhang ZM, Quan X, Cheng P. A numerical study on effects of surrounding medium, material, and geometry of nanoparticles on solar absorption efficiencies. *Int J Heat Mass Transf* 2018;116:825–32. doi:10.1016/j.ijheatmasstransfer.2017.09.014.
- [75] Ren Y, Qi H, Chen Q, Wang S, Ruan L. Localized surface plasmon resonance of nanotriangle dimers at different relative positions. *J Quant Spectrosc Radiat Transf* 2017;199:45–51. doi:10.1016/j.jqsrt.2017.05.003.
- [76] Roopak S, Ji A, Parashar PK, Sharma RP. Light incoupling tolerance of resonant and nonresonant metal nanostructures embedded in perovskite medium: Effect of various geometries on broad spectral resonance. *J Phys D Appl Phys* 2017;50:335105. doi:10.1088/1361-6463/aa783e.
- [77] Jain PK, Lee KS, El-Sayed IH, El-Sayed MA. Calculated absorption and scattering properties of gold nanoparticles of different size, shape, and composition: Applications in biological imaging and biomedicine. *J Phys Chem B* 2006;110:7238–48. doi:10.1021/jp057170o.
- [78] Agrawal A, Kriegel I, Milliron DJ. Shape-dependent field enhancement and plasmon resonance of oxide nanocrystals. *J Phys Chem C* 2015;119:6227–38. doi:10.1021/acs.jpcc.5b01648.
- [79] Raziman T V., Martin OJF. Polarisation charges and scattering behaviour of realistically rounded plasmonic nanostructures. *Opt Express* 2013;21:21500. doi:10.1364/oe.21.021500.
- [80] Sosa IO, Noguez C, Barrera RG. Optical properties of metal nanoparticles with arbitrary shapes. *J Phys Chem B* 2003;107:6269–75. doi:10.1021/jp0274076.
- [81] Lombardi A, Loumaigne M, Crut A, Maioli P, Del Fatti N, Vallée F, et al. Surface plasmon resonance properties of single elongated nano-objects: Gold nanobipyramids and nanorods. *Langmuir* 2012;28:9027–33. doi:10.1021/la300210h.
- [82] Giannini V, Rodríguez-Oliveros R, Sánchez-Gil JA. Surface plasmon resonances of metallic nanostars/nanoflowers for surface-enhanced Raman scattering. *Plasmonics* 2010;5:99–104. doi:10.1007/s11468-009-9121-3.
- [83] Kwaadgras BW, Verdult M, Dijkstra M, Van Roij R. Polarizability and alignment of dielectric nanoparticles in an external electric field: Bowls, dumbbells, and cuboids. *J Chem Phys* 2011;135:1–15. doi:10.1063/1.3637046.
- [84] Chung HY, Leung PT, Tsai DP. Modified Long Wavelength Approximation for the Optical Response of a Graded-Index Plasmonic Nanoparticle. *Plasmonics* 2012;7:13–8. doi:10.1007/s11468-011-9269-5.
- [85] Wang W, Chi X, Feng Y, Zhao Y. Parallel FDTD Simulation of Photonic Crystals

- and Thin-Film Solar Cells. 2012 13th Int. Conf. Parallel Distrib. Comput. Appl. Technol., IEEE; 2012, p. 773–6. doi:10.1109/PDCAT.2012.106.
- [86] Schneider J. Understanding the Finite-Difference Time-Domain Method. Artech House Antennas Propag Libr 2005;2010:1006.
- [87] Masouleh FF, Das N, Rozati SM. Nano-structured gratings for improved light absorption efficiency in solar cells. *Energies* 2016;9:756. doi:10.3390/en9090756.
- [88] Chung H, Jung K-Y, Tee XT, Bermel P. Time domain simulation of tandem silicon solar cells with optimal textured light trapping enabled by the quadratic complex rational function. *Opt Express* 2014;22:A818. doi:10.1364/OE.22.00A818.
- [89] Cai B, Peng Y, Cheng Y-B, Gu M. 4-Fold Photocurrent Enhancement in Ultrathin Nanoplasmonic Perovskite Solar Cells. *Opt Express* 2015;23:A1700. doi:10.1364/OE.23.0A1700.
- [90] Agarwal S, Nair PR. Performance loss analysis and design space optimization of perovskite solar cells. *J Appl Phys* 2018;124. doi:10.1063/1.5047841.
- [91] Deparis O, Vigneron JP, Agustsson O, Decroupet D. Optimization of photonics for corrugated thin-film solar cells. *J Appl Phys* 2009;106. doi:10.1063/1.3253755.
- [92] Dewan R, Knipp D. Light trapping in thin-film silicon solar cells with integrated diffraction grating. *J Appl Phys* 2009;106:074901. doi:10.1063/1.3232236.
- [93] Ferry VE, Verschuuren MA, Lare MC Van, Schropp REI, Atwater HA, Polman A. Optimized spatial correlations for broadband light trapping nanopatterns in high efficiency ultrathin film a-Si:H solar cells. *Nano Lett* 2011;11:4239–45. doi:10.1021/nl202226r.
- [94] Wiesendanger S, Zilk M, Pertsch T, Lederer F, Rockstuhl C. A path to implement optimized randomly textured surfaces for solar cells. *Appl Phys Lett* 2013;103:13115. doi:10.1063/1.4823554.
- [95] Wiesendanger S, Zilk M, Pertsch T, Rockstuhl C, Lederer F. Combining randomly textured surfaces and photonic crystals for the photon management in thin film microcrystalline silicon solar cells. *Opt Express* 2013;21:A450. doi:10.1364/OE.21.00A450.
- [96] Tsai CC, Grote RR, Beck JH, Kyymissis I, Osgood RM, Englund D. General method for simultaneous optimization of light trapping and carrier collection in an ultrathin film organic photovoltaic cell. *J Appl Phys* 2014;116:023110. doi:10.1063/1.4890275.
- [97] Mendes MJ, Araújo A, Vicente A, Águas H, Ferreira I, Fortunato E, et al. Design of optimized wave-optical spheroidal nanostructures for photonic-enhanced solar cells. *Nano Energy* 2016;26:286–96. doi:10.1016/j.nanoen.2016.05.038.
- [98] Hou J, Hong W, Li X, Yang C, Chen S. Biomimetic spiral grating for stable and highly efficient absorption in crystalline silicon thin-film solar cells: erratum. *Opt Express* 2017;25:A1053. doi:10.1364/oe.25.0a1053.

- [99] Shen H, Bienstman P, Maes B. Plasmonic absorption enhancement in organic solar cells with thin active layers. *J Appl Phys* 2009;106:073109. doi:10.1063/1.3243163.
- [100] Vedraïne S, Torchio P, Duche D, Flory F, Simon J-J, Rouzo J Le, et al. Intrinsic absorption of plasmonic structures for organic solar cells. *Sol Energy Mater Sol Cells* 2011;95:S57–64.
- [101] Fallahpour AH, Ulisse G, Auf Der Maur M, Di Carlo A, Brunetti F. 3-D simulation and optimization of organic solar cell with periodic back contact grating electrode. *IEEE J Photovoltaics* 2015;5:591–6. doi:10.1109/JPHOTOV.2014.2373813.
- [102] Spitzer F. *Principles of Random Walk*. New York: Springer-Verlag; 1964. doi:10.1007/978-1-4757-4229-9.
- [103] Lin C, Povinelli ML. Optimal design of aperiodic, vertical silicon nanowire structures for photovoltaics. *Opt InfoBase Conf Pap* 2011;19:34310–6. doi:10.1364/oe.19.0a1148.
- [104] Sheng X, Johnson SG, Michel J, Kimerling LC. Optimization-based design of surface textures for thin-film Si solar cells - Are conventional Lambertian models relevant? *Opt Express* 2011;19:A841. doi:10.1109/PVSC.2011.6185834.
- [105] Sheng X, Broderick LZ, Kimerling LC. Photonic crystal structures for light trapping in thin-film Si solar cells: Modeling, process and optimizations. *Opt Commun* 2014;314:41–7. doi:10.1016/j.optcom.2013.07.085.
- [106] Bertsekas DP. *Nonlinear Programming*. Athena Scientific; 1999.
- [107] Fletcher R. *Practical Methods of Optimization*. 2nd ed. John Wiley and Sons; 2000.
- [108] Yu S, Wang C, Sun C, Chen W. Topology optimization for highly-efficient light-trapping structure in solar cells. *Struct Multidiscip Optim* 2014;50:367–82. doi:10.1007/s00158-014-1077-z.
- [109] Baloch AAB, Aly SP, Hossain MI, El-Mellouhi F, Tabet N, Alharbi FH. Full space device optimization for solar cells. *Sci Rep* 2017;7:1–14. doi:10.1038/s41598-017-12158-0.
- [110] Rezaei N, Isabella O, Vroon Z, Zeman M. Optical optimization of a multi-layer wideband anti-reflection coating using porous MgF₂ for sub-micron-thick CIGS solar cells. *Sol Energy* 2019;177:59–67. doi:10.1016/j.solener.2018.11.015.
- [111] Hajimirza S, El Hitti G, Heltzel A, Howell J. Using inverse analysis to find optimum nano-scale radiative surface patterns to enhance solar cell performance. *Int J Therm Sci* 2012;62:93–102. doi:10.1016/j.ijthermalsci.2011.12.011.
- [112] Hajimirza S, El Hitti G, Heltzel A, Howell J. Specification of Micro-Nanoscale Radiative Patterns Using Inverse Analysis for Increasing Solar Panel Efficiency. *J Heat Transfer* 2012;134:102702. doi:10.1115/1.4006209.
- [113] Hajimirza S, Howell JR. Design and analysis of spectrally selective patterned thin-film cells. *Int J Thermophys* 2013;34:1930–52. doi:10.1007/s10765-013-1495-y.

- [114] Mitchell M. *An Introduction to Genetic Algorithms*. Cambridge: MIT Press; 1998.
- [115] Schwefel H-P. *Numerische Optimierung von Computer-Modellen mittels der Evolutionsstrategie*. Basel: Springer; 1977.
- [116] Schwefel H-P. *Numerical Optimization of Computer Models*. New York: John Wiley & Sons, Inc.; 1981.
- [117] Kirkpatrick S, Gelatt CD, Vecchi MP. Optimization by Simulated Annealing. *Science* (80-) 1983;220:671–80. doi:10.1126/science.220.4598.671.
- [118] Kennedy J. Particle swarm: Social adaptation of knowledge. *Proc IEEE Conf Evol Comput ICEC 1997*:303–8. doi:10.1109/icec.1997.592326.
- [119] Lin A, Phillips J. Optimization of random diffraction gratings in thin-film solar cells using genetic algorithms. *Sol Energy Mater Sol Cells* 2008;92:1689–96. doi:10.1016/j.solmat.2008.07.021.
- [120] Lin A, Fu S-M, Chung Y-K, Lai S, Tseng C-W. An optimized surface plasmon photovoltaic structure using energy transfer between discrete nano-particles. *Opt Express* 2013;21:A131. doi:10.1364/oe.21.00a131.
- [121] Lin AS, Fu S-M, Zhong Y-K, Tseng C-W, Lai S, Kwok Lau TC. Optimization of plasmonic cavity-resonant multijunction cells. *Opt Eng* 2013;52:064002. doi:10.1117/1.oe.52.6.064002.
- [122] Lin A, Zhong Y-K, Fu S-M, Tseng CW, Yan SL. Aperiodic and randomized dielectric mirrors: alternatives to metallic back reflectors for solar cells. *Opt Express* 2014;22:A880. doi:10.1364/oe.22.00a880.
- [123] Lin AS, Zhong YK, Fu SM, Tseng CW, Lai SY, Lai WM. Lithographically fabricable, optimized three-dimensional solar cell random structure. *J Opt (United Kingdom)* 2013;15. doi:10.1088/2040-8978/15/10/105007.
- [124] Wang C, Yu S, Chen W, Sun C. Highly efficient light-trapping structure design inspired by natural evolution. *Sci Rep* 2013;3:1025. doi:10.1038/srep01025.
- [125] Gouvêa RA, Moreira ML, Souza JA. Evolutionary design algorithm for optimal light trapping in solar cells. *J Appl Phys* 2019;125. doi:10.1063/1.5078745.
- [126] Bittkau K, Kirchartz T, Rau U. Optical design of spectrally selective interlayers for perovskite/silicon heterojunction tandem solar cells. *Opt Express* 2018;26:A750. doi:10.1364/oe.26.00a750.
- [127] Muller J, Herman A, Mayer A, Deparis O. A fair comparison between ultrathin crystalline-silicon solar cells with either periodic or correlated disorder inverted pyramid textures. *Opt Express* 2015;23:A657. doi:10.1364/oe.23.00a657.
- [128] Rajbhandari PP, Emrani A, Dhakal TP, Westgate CR, Klotzkin D. Antireflection coatings designed by the average uniform algorithm for thin film solar cells. *Appl Opt* 2014;53:8006. doi:10.1364/ao.53.008006.
- [129] Zhao Y, Chen F, Shen Q, Zhang L. Light-trapping design of graphene transparent

- electrodes for efficient thin-film silicon solar cells. *Appl Opt* 2012;51:6245–51. doi:10.1364/AO.51.006245.
- [130] Zhao Y, Chen F, Shen Q, Zhang L. Optimal design of light trapping in thin-film solar cells enhanced with graded SiN_x and SiO_xN_y structure. *Opt Express* 2012;20:11121. doi:10.1364/oe.20.011121.
- [131] Zhao Y, Chen F, Shen Q, Zhang L. Optimal structure of light trapping in thin-film solar cells: dielectric nanoparticles or multilayer antireflection coatings? *Appl Opt* 2014;53:5222. doi:10.1364/ao.53.005222.
- [132] Solano M, Faryad M, Hall AS, Mallouk TE, Monk PB, Lakhtakia A. Optimization of the absorption efficiency of an amorphous-silicon thin-film tandem solar cell backed by a metallic surface-relief grating. *Appl Opt* 2013;52:966–79. doi:10.1364/AO.52.000966.
- [133] Zhou S, Hunang X, Li Q, Xie YM. Optimizing two-level hierarchical particles for thin-film solar cells. *Opt Express* 2013;21:A285. doi:10.1364/OE.21.00A285.
- [134] Aiello G, Alfonzetti S, Rizzo SA, Salerno N. Optimization of plasmon-enhanced thin-film heterojunction solar cells. *IEEE Trans Magn* 2015;51:1–4. doi:10.1109/TMAG.2014.2361272.
- [135] Aiello G, Alfonzetti S, Rizzo SA, Salerno N. Multi-objective optimization of thin-film silicon solar cells with metallic and dielectric nanoparticles. *Energies* 2017;10. doi:10.3390/en10010053.
- [136] Kirsch C, Mitran S. Simulated annealing electro-photonic optimization of organic solar cells. *J Appl Phys* 2012;112:054502. doi:10.1063/1.4748314.
- [137] Jäger K, Fischer M, van Swaaij RACMM, Zeman M. Designing optimized nano textures for thin-film silicon solar cells. *Opt Express* 2013;21:A656. doi:10.1364/OE.21.00A656.
- [138] Hajimirza S, Howell JR. Computational and experimental study of a multi-layer absorptivity enhanced thin film silicon solar cell. *J Quant Spectrosc Radiat Transf* 2014;143:56–62. doi:10.1016/j.jqsrt.2013.09.025.
- [139] Hajimirza S, Howell JR. Statistical Analysis of Surface Nanopatterned Thin Film Solar Cells Obtained by Inverse Optimization. *J Heat Transfer* 2013;135:091501. doi:10.1115/1.4024464.
- [140] Hajimirza S, Howell JR. Flexible Nanotexture Structures for Thin Film PV Cells Using Wavelet Functions. *IEEE Trans Nanotechnol* 2015;14:904–10. doi:10.1109/TNANO.2015.2462078.
- [141] Arinze ES, Qiu B, Palmquist N, Cheng Y, Lin Y, Nyirjesy G, et al. Color-tuned and transparent colloidal quantum dot solar cells via optimized multilayer interference. *Opt Express* 2017;25:A101. doi:10.1364/oe.25.00a101.
- [142] Ferhati H, Djefal F, Kacha K. Optimizing the optical performance of ZnO/Si-based solar cell using metallic nanoparticles and interface texturization. *Optik (Stuttg)*

- 2018;153:43–9. doi:10.1016/j.ijleo.2017.09.127.
- [143] Ferhati H, Djefal F, Srairi F. Enhancement of the absorbance figure of merit in amorphous-silicon p-i-n solar cell by using optimized intermediate metallic layers. *Optik (Stuttg)* 2017;130:473–80. doi:10.1016/j.ijleo.2016.10.073.
- [144] Forrester AIJ, Keane AJ. Recent advances in surrogate-based optimization. *Prog Aerosp Sci* 2009;45:50–79. doi:10.1016/j.paerosci.2008.11.001.
- [145] Bhosekar A, Ierapetritou M. Advances in surrogate based modeling, feasibility analysis, and optimization: A review. *Comput Chem Eng* 2018;108:250–67. doi:10.1016/j.compchemeng.2017.09.017.
- [146] Chatterjee T, Chakraborty S, Chowdhury R. A Critical Review of Surrogate Assisted Robust Design Optimization. *Arch Comput Methods Eng* 2019;26:245–74. doi:10.1007/s11831-017-9240-5.
- [147] Queipo N V., Haftka RT, Shyy W, Goel T, Vaidyanathan R, Kevin Tucker P. Surrogate-based analysis and optimization. *Prog Aerosp Sci* 2005;41:1–28. doi:10.1016/j.paerosci.2005.02.001.
- [148] Jin R, Chen W, Sudjianto A. On sequential sampling for global metamodeling in engineering design. *Proc. DETC'02 ASME 2002 Des. Eng. Tech. Conf. Comput. Inf. Eng. Conf.*, Montreal: 2002, p. 1–10.
- [149] Boukouvala F, Ierapetritou MG. Surrogate-Based Optimization of Expensive Flowsheet Modeling for Continuous Pharmaceutical Manufacturing. *J Pharm Innov* 2013;8:131–45. doi:10.1007/s12247-013-9154-1.
- [150] Crombecq K, Gorissen D, Deschrijver D, Dhaene T. A Novel Hybrid Sequential Design Strategy for Global Surrogate Modeling of Computer Experiments. *SIAM J Sci Comput* 2011;33:1948–74. doi:10.1137/090761811.
- [151] Garud SS, Karimi IA, Kraft M. Smart Sampling Algorithm for Surrogate Model Development. *Comput Chem Eng* 2017;96:103–14. doi:10.1016/j.compchemeng.2016.10.006.
- [152] Eason J, Cremaschi S. Adaptive sequential sampling for surrogate model generation with artificial neural networks. *Comput Chem Eng* 2014;68:220–32. doi:10.1016/j.compchemeng.2014.05.021.
- [153] Garud SS, Karimi IA, Kraft M. Design of computer experiments : A review. *Comput Chem Eng* 2017;106:71–95. doi:10.1016/j.compchemeng.2017.05.010.
- [154] Rasmussen CE, Williams CKI. *Gaussian Processes for Machine Learning*. London: MIT Press; 2006. doi:10.1142/S0129065704001899.
- [155] Basheer IA, Hajmeer M. Artificial neural networks: Fundamentals, computing, design, and application. *J Microbiol Methods* 2000;43:3–31. doi:10.1016/S0167-7012(00)00201-3.
- [156] Foresee FD, Hagan MT. Gauss-Newton approximation to Bayesian regularization. *Proc. 1997 Int. Jt. Conf. Neural Networks*, 1997, p. 1930–5.

doi:10.1109/ICNN.1997.614194.

- [157] Smola AJ, Schölkopf B. A tutorial on support vector regression. *Stat Comput* 2004;14:199–222. doi:10.1023/B:STCO.0000035301.49549.88.
- [158] Chen T, Guestrin C. XGBoost: A scalable tree boosting system. *Proc. ACM SIGKDD Int. Conf. Knowl. Discov. Data Min.*, 2016, p. 785–94. doi:10.1145/2939672.2939785.
- [159] Demuth HB, Beale MH, Hagan MT. *Neural Network Design*. 1995. doi:10.1007/1-84628-303-5.
- [160] Were K, Bui DT, Dick ØB, Singh BR. A comparative assessment of support vector regression, artificial neural networks, and random forests for predicting and mapping soil organic carbon stocks across an Afromontane landscape. *Ecol Indic* 2015;52:394–403. doi:10.1016/j.ecolind.2014.12.028.
- [161] Iwata T, Ghahramani Z. *Improving Output Uncertainty Estimation and Generalization in Deep Learning via Neural Network Gaussian Processes* 2017.
- [162] Hagan MT, Demuth HB, Beale MH, De Jesus O. *Neural Network Design*. Boston, MA: PWS Publishing Company; 2014. doi:10.1007/1-84628-303-5.
- [163] Breiman L, Friedman JH, Olshen RA, Stone CJ. *Classification and Regression Trees*. Monterey, CA: Wadsworth & Brooks/Cole Advanced Books & Software; 1984.
- [164] Friedman JH. Greedy function approximation: A gradient boosting machine. *Ann Stat* 2001;29:1189–232. doi:10.1214/aos/1013203451.
- [165] Mlinar V. Engineered nanomaterials for solar energy conversion. *Nanotechnology* 2013;24:042001. doi:10.1088/0957-4484/24/4/042001.
- [166] Yosipof A, Nahum OE, Anderson AY, Barad HN, Zaban A, Senderowitz H. Data Mining and Machine Learning Tools for Combinatorial Material Science of All-Oxide Photovoltaic Cells. *Mol Inform* 2015;34:367–79. doi:10.1002/minf.201400174.
- [167] Hajimirza S. A novel machine-learning aided optimization technique for material design: application in thin film solar cells. *Proc. ASME 2016 HT/FEDSM/ICNMM Summer Heat Transf. Conf.*, Capitol Hill, Washington DC, USA: 2016.
- [168] Kaya M, Hajimirza S. Extremely Efficient Design of Organic Thin Film Solar Cells via Learning-Based Optimization. *Energies* 2017;10:1981.
- [169] Kaya M, Hajimirza S. Surrogate based modeling and optimization of plasmonic thin film organic solar cells. *Int J Heat Mass Transf* 2018;118:1128–42. doi:10.1016/j.ijheatmasstransfer.2017.11.044.
- [170] Kaya M, Hajimirza S. Application of artificial neural network for accelerated optimization of ultra thin organic solar cells. *Sol Energy* 2018;165:159–66. doi:10.1016/j.solener.2018.02.062.

- [171] Kaya M, Hajimirza S. Rapid Optimization of External Quantum Efficiency of Thin Film Solar Cells Using Surrogate Modeling of Absorptivity. *Sci Rep* 2018;8:8170. doi:10.1038/s41598-018-26469-3.
- [172] Hamed S, Kordrostami Z, Yadollahi A. Artificial neural network approaches for modeling absorption spectrum of nanowire solar cells. *Neural Comput Appl* 2019;31:8985–95. doi:10.1007/s00521-019-04406-3.
- [173] Zhang Y, Apley D, Chen W. Bayesian Optimization for Materials Design with Mixed Quantitative and Qualitative Variables. *Sci Rep* 2020;10:4924.
- [174] Liu D, Tan Y, Khoram E, Yu Z. Training Deep Neural Networks for the Inverse Design of Nanophotonic Structures. *ACS Photonics* 2018;5:1365–9. doi:10.1021/acsp Photonics.7b01377.
- [175] Yu S, Wang J, Zhang T, Zhou R, Dai J, Zhou Y, et al. Performance optimization for plasmonic refractive index sensor based on machine learning. *Proc. SPIE 11048, 17th Int. Conf. Opt. Commun. Networks, 2019.* doi:10.1117/12.2519699.
- [176] Zhang T, Wang J, Liu Q, Zhou J, Dai J, Han X, et al. Efficient spectrum prediction and inverse design for plasmonic waveguide systems based on artificial neural networks. *Photonics Res* 2019;7:368. doi:10.1364/prj.7.000368.
- [177] Chen Y, Zhu J, Xie Y, Feng N, Liu QH. Smart inverse design of graphene-based photonic metamaterials by an adaptive artificial neural network. *Nanoscale* 2019;11:9749–55. doi:10.1039/c9nr01315f.
- [178] Inampudi S, Mosallaei H. Neural network based design of metagratings. *Appl Phys Lett* 2018;112:241102. doi:10.1063/1.5033327.
- [179] Asano T, Noda S. Optimization of photonic crystal nanocavities based on deep learning. *Opt Express* 2018;26:32704. doi:10.1364/oe.26.032704.
- [180] Peurifoy J, Shen Y, Jing L, Yang Y, Cano-Renteria F, DeLacy BG, et al. Nanophotonic particle simulation and inverse design using artificial neural networks. *Sci Adv* 2018;4:1–8. doi:10.1126/sciadv.aar4206.
- [181] Hegde RS. Accelerating optics design optimizations with deep learning. *Opt Eng* 2019;58:1. doi:10.1117/1.oe.58.6.065103.
- [182] Jiang J, Sell D, Hoyer S, Hickey J, Yang J, Fan JA. Free-Form Diffractive Metagrating Design Based on Generative Adversarial Networks. *ACS Nano* 2019;13:8872–8. doi:10.1021/acsnano.9b02371.
- [183] Sajedian I, Badloe T, Rho J. Optimisation of colour generation from dielectric nanostructures using reinforcement learning. *Opt Express* 2019;27:5874. doi:10.1364/oe.27.005874.
- [184] Gupta A, Ong Y, Feng L. Insights on Transfer Optimization: Because Experience is the Best Teacher. *IEEE Trans Emerg Top Comput Intell* 2017;2:1–14. doi:10.1109/TETCI.2017.2769104.
- [185] Quattoni A, Collins M, Darrell T, Csail MIT, Eecs UCB. Transfer Learning for

- Image Classification with Sparse Prototype Representations. Proc. Comput. Vis. Pattern Recognition, 2008. CVPR 2008. IEEE Conf., 2008, p. 1-8. doi:10.1109/CVPR.2008.4587637.
- [186] Raina R, Battle A, Lee H, Packer B, Ng AY. Self-taught Learning: Transfer Learning from Unlabeled Data. Proc. 24th Int. Conf. Mach. Learn., Corvallis, OR: 2007, p. 759.
- [187] Fung GPC, Yu JX, Lu H, Yu PS. Text classification without negative examples revisited. IEEE Trans Knowl Data Eng 2006;18:6–20. doi:10.1109/TKDE.2006.16.
- [188] Dai W, Yang Q, Xue G-R, Yu Y. Boosting for transfer learning. Proc 24th Int Conf Mach Learn - ICML '07 2007:193–200. doi:10.1145/1273496.1273521.
- [189] Zanini P, Congedo M, Jutten C, Said S, Berthoumieu Y. Transfer Learning: a Riemannian geometry framework with applications to Brain-Computer Interfaces. IEEE Trans Biomed Eng 2017;65:1–1. doi:10.1109/TBME.2017.2742541.
- [190] Waytowich NR, Lawhern VJ, Bohannon AW, Ball KR, Lance BJ. Spectral transfer learning using information geometry for a user-independent brain-computer interface. Front Neurosci 2016;10. doi:10.3389/fnins.2016.00430.
- [191] Choi K, Fazekas G, Sandler M, Cho K. Transfer learning for music classification and regression tasks. [Preprint] 2017. Available from: <https://arxiv.org/abs/1703.09179>
- [192] Lin Y-P, Jung T-P. Improving EEG-Based Emotion Classification Using Conditional Transfer Learning. Front Hum Neurosci 2017;11:1–11. doi:10.3389/fnhum.2017.00334.
- [193] Pardoe D, Stone P. Boosting for Regression Transfer. Proc. 27th Int. Conf. Mach. Learn., Haifa, Israel: 2010.
- [194] Jamshidi P, Velez M, Kästner C, Siegmund N, Kawthekar P. Transfer Learning for Improving Model Predictions in Highly Configurable Software. Proc - 2017 IEEE/ACM 12th Int Symp Softw Eng Adapt Self-Managing Syst SEAMS 2017 2017:31–41. doi:10.1109/SEAMS.2017.11.
- [195] Lindner C, Waring D, Thiruvenkatachari B, O'Brien K, Cootes TF. Adaptable landmark localisation: Applying model transfer learning to a shape model matching system. Lect Notes Comput Sci (Including Subser Lect Notes Artif Intell Lect Notes Bioinformatics) 2017;10433 LNCS:144–51. doi:10.1007/978-3-319-66182-7_17.
- [196] Gao J, Ling H, Hu W, Xing J. Transfer Learning Based Visual Tracking with Gaussian Processes Regression. Eur. Conf. Comput. Vis., Zurich, Switzerland: 2014, p. 188–203. doi:10.1007/978-3-319-10578-9_13.
- [197] Yogatama D, Mann G. Efficient Transfer Learning Method for Automatic Hyperparameter Tuning. Proc Seventeenth Int Conf Artif Intell Stat 2014;33:1077–85.

- [198] Joy TT, Rana S, Gupta S, Venkatesh S. Hyperparameter tuning for big data using Bayesian optimisation. *Proc. - Int. Conf. Pattern Recognit.*, 2017, p. 2574–9. doi:10.1109/ICPR.2016.7900023.
- [199] Feurer M, Springenberg JT, Hutter F. Initializing Bayesian Hyperparameter Optimization via Meta-Learning. *Aaai*, 2015, p. 1128–35.
- [200] Wistuba M, Schilling N, Schmidt-Thieme L. Learning hyperparameter optimization initializations. *Proc 2015 IEEE Int Conf Data Sci Adv Anal DSAA 2015 2015*. doi:10.1109/DSAA.2015.7344817.
- [201] Li D, Wang S, Yao S, Liu Y, Cheng Y, Sun X. Efficient Design Space Exploration by Knowledge Transfer. *Codes/Isss '16*, vol. 1, 2016.
- [202] Min ATW, Sagarna R, Gupta A, Ong Y-S. Knowledge Transfer Through Machine Learning in Aircraft Design. *IEEE Comput Intell Mag* 2017;12:48–60.
- [203] Kaya M, Hajimirza S. Using a Novel Transfer Learning Method for Designing Thin Film Solar Cells with Enhanced Quantum Efficiencies. *Sci Rep* 2019;9:5034. doi:10.1038/s41598-019-41316-9.
- [204] Kaya M, Hajimirza S. Using Bayesian Optimization with Knowledge Transfer for High Computational Cost Design: A Case Study in Photovoltaics. *Proc. ASME 2019 Int. Des. Eng. Tech. Conf. Comput. Inf. Eng. Conf. IDETC/CIE2019*, Anaheim, CA, USA: 2019, p. 1–9.
- [205] Atwater HA, Polman A. Plasmonics for improved photovoltaic devices. *Nat Mater* 2010;9:865–865. doi:10.1038/nmat2866.
- [206] N’Konou K, Peres L, Torchio P. Optical Absorption Modeling of Plasmonic Organic Solar Cells Embedding Silica-Coated Silver Nanospheres. *Plasmonics* 2017;1–7. doi:10.1007/s11468-017-0514-4.
- [207] Zhu S-Q, Zhang T, Guo X-L, Shan F, Zhang X-Y. Light absorption enhancement in organic solar cell by embedding Ag nanoparticles and nanochains within the active layer. *J Nanomater* 2014;2014:8. doi:10.1155/2014/736165.
- [208] American Society for Testing and Materials, 2003, “ASTM Standard Tables for Reference Solar Spectral Irradiances” n.d. <http://www.astm.org> (accessed September 20, 2017).
- [209] Moreno F, García-Cámara B, Saiz JM, González F. Interaction of nanoparticles with substrates: effects on the dipolar behaviour of the particles. *Opt Express* 2008;16:12487–504. doi:10.1364/OE.16.012487.
- [210] Ou K, Ehamparam R, Macdonald G, Stubhan T, Wu X, Shallcross RC, et al. Characterization of ZnO Interlayers for Organic Solar Cells: Correlation of Electrochemical Properties with Thin-Film Morphology and Device Performance 2016. doi:10.1021/acsami.6b02792.
- [211] Ullah I, Shah SK, Wali S, Hayat K, Khattak SA, Khan A. Enhanced efficiency of organic solar cells by using ZnO as an electron-transport layer Enhanced efficiency

- of organic solar cells by using ZnO as an electron-transport layer. *Mater Res Express* 2017;4:125505.
- [212] Shah A V, Schade H, Vanecek M, Meier J, Vallat-Sauvain E, Wyrsh N, et al. Thin-film Silicon Solar Cell Technology. *Photovolt Res Appl* 2004;12:113–42. doi:10.1002/pip.533.
- [213] Petoukhoff CE, Vijapurapu DK, Carroll DMO. Computational comparison of conventional and inverted organic photovoltaic performance parameters with varying metal electrode surface workfunction. *Sol Energy Mater Sol Cells* 2014;120:572–83. doi:10.1016/j.solmat.2013.09.041.
- [214] Nazerdeylami S, Dizaji HR. A theoretical study of influence of charge carrier mobility in PTB7:PC71BM bulk heterojunction organic solar cells. *Opt Quantum Electron* 2016;48:506. doi:10.1007/s11082-016-0780-y.
- [215] Wen L, Chen Q, Song S, Yu Y, Jin L, Hu X. Photon harvesting , coloring and polarizing in photovoltaic cell integrated color filters : efficient energy routing strategies for power-saving displays. *Nanotechnology* 2015;26:265203. doi:10.1088/0957-4484/26/26/265203.
- [216] Jo BJ, Na S, Kim S, Lee T, Chung Y, Kang S, et al. Three-Dimensional Bulk Heterojunction Morphology for Achieving High Internal Quantum Efficiency in Polymer Solar Cells 2009:2398–406. doi:10.1002/adfm.200900183.
- [217] Fuzhi W, Bing Z, Qiuxiang L, Zhenzhen S, Lu Y, Liu H, et al. Management of the light distribution within the photoactive layer for high performance conventional and inverted polymer solar cells. *J Mater Chem A* 2016;4:1915–22. doi:10.1039/c5ta10192a.
- [218] Cho S, Coates N, Moon JS, Park SH, Roy A, Beaupre S, et al. Bulk heterojunction solar cells with internal quantum efficiency approaching 100 %. *Nat Photonics* 2009;3:297–303. doi:10.1038/NPHOTON.2009.69.
- [219] Pan SJ, Yang Q. A Survey on Transfer Learning. *IEEE Trans Knowl Data Eng* 2009;22:1345–1359.
- [220] Hu Q, Zhang R, Zhou Y. Transfer learning for short-term wind speed prediction with deep neural networks. *Renew Energy* 2016;85:83–95. doi:10.1016/j.renene.2015.06.034.
- [221] MacKay DJC. A Practical Bayesian Framework for Backpropagation Networks. *Neural Comput* 1992;4:448–72. doi:10.1162/neco.1992.4.3.448.
- [222] Bonilla E, Chai KM, Williams C. Multi-task Gaussian Process Prediction. *Proc Adv Neural Inf Process Syst 20 (NIPS 2007)* 2008;20:153–60.
- [223] Karvonen T, Sarkka S. Classical quadrature rules via Gaussian processes. *Proc. IEEE Int. Work. Mach. Learn. Signal Process. MLSP, Tokyo, Japan: 2017.* doi:10.1109/MLSP.2017.8168195.
- [224] Mockus J. Application of Bayesian approach to numerical methods of global and

- stochastic optimization. *J Glob Optim* 1994;4:347–65. doi:10.1007/BF01099263.
- [225] Kawaguchi K, Kaelbling LP, Lozano-Pérez T. Bayesian optimization with exponential convergence. *Proc. Adv. Neural Inf. Process. Syst.* 28 (NIPS 2015), 2015, p. 2809–17.
- [226] Allaire G, Dapogny C, Frey P. Shape optimization with a level set based mesh evolution method. *Comput Methods Appl Mech Eng* 2014;282:22–53. doi:10.1016/j.cma.2014.08.028.
- [227] Papalambros PY. The optimization paradigm in engineering design: Promises and challenges. *CAD Comput Aided Des* 2002;34:939–51. doi:10.1016/S0010-4485(01)00148-8.
- [228] Andkjær J, Nishiwaki S, Nomura T, Sigmund O. Topology optimization of grating couplers for the efficient excitation of surface plasmons. *J Opt Soc Am B* 2010;27:1828. doi:10.1364/JOSAB.27.001828.
- [229] Soh H, Yoo J. Texturing Design for a Light Trapping System Using Topology Optimization. *IEEE Trans Mag* 2012;48:227–30.
- [230] Yu S, Wang C, Sun C, Chen W. Topology optimization for light-trapping structure in solar cells. *Struct Multidiscip Optim* 2014;50:367–82. doi:10.1007/s00158-014-1077-z.
- [231] Yang P, Liou KN. Finite-difference time domain method for light scattering by small ice crystals in three-dimensional space. *J Opt Soc Am A* 1996;13:2072. doi:10.1364/josaa.13.002072.
- [232] Sun W, Fu Q, Chen Z. Finite-difference time-domain solution of light scattering by dielectric particles with a perfectly matched layer absorbing boundary condition. *Appl Opt* 1999;38:3141. doi:10.1364/ao.38.003141.
- [233] Sun W, Videen G, Fu Q, Hu Y. Scattered-field FDTD and PSTD algorithms with CPML absorbing boundary conditions for light scattering by aerosols. *J Quant Spectrosc Radiat Transf* 2013;131:166–74. doi:10.1016/j.jqsrt.2013.07.015.
- [234] Sigmund O. Morphology-based black and white filters for topology optimization. *Struct Multidiscip Optim* 2007;33:401–24. doi:10.1007/s00158-006-0087-x.
- [235] Li Q, Steven GP, Xie YM. A simple checkerboard suppression algorithm for evolutionary structural optimization. *Struct Multidiscip Optim* 2001;22:230–9. doi:10.1007/s001580100140.
- [236] Loncaric S. A survey of shape analysis techniques. *Pattern Recognit* 1998;31:983–1001. doi:10.1016/S0031-2023(97)00122-2.
- [237] Karczmarek P, Kiersztyn A, Pedrycz W, Dolecki M. An application of chain code-based local descriptor and its extension to face recognition. *Pattern Recognit* 2017;65:26–34. doi:10.1016/j.patcog.2016.12.008.
- [238] Arica N, Yarman Vural FT. BAS: A perceptual shape descriptor based on the beam angle statistics. *Pattern Recognit Lett* 2003;24:1627–39. doi:10.1016/S0167-

8655(03)00002-3.

- [239] Belongie S, Malik J, Puzicha J. Shape context: A new descriptor for shape matching and object recognition. *Adv Neural Inf Process Syst* 2001:831–7.
- [240] Smith SP, Jain AK. Chord Distributions for Shape Matching. *Comput Graph Image Process* 1982;20:259–71. doi:10.1016/0146-664x(82)90163-0.
- [241] Andrews M, Kakarala R. Shape simplification through polygonal approximation in the Fourier domain. *Intell. Robot. Comput. Vis. XXXII Algorithms Tech.*, San Francisco, CA, USA: 2015, p. 94060D. doi:10.1117/12.2078148.
- [242] Yuan Z, Li F, Zhang P, Chen B. Description of shape characteristics through Fourier and wavelet analysis. *Chinese J Aeronaut* 2014;27:160–8. doi:10.1016/j.cja.2013.07.011.
- [243] Yang M, Kpalma K, Ronsin J. A Survey of Shape Feature Extraction Techniques. *Pattern Recognit* 2008:43–90.
- [244] Taubin G, Cooper DB. Recognition and positioning of rigid objects using algebraic moment invariants. *Geom Methods Comput Vis* 1991;1570:175. doi:10.1117/12.48423.
- [245] Dai X, Khorram S. A feature-based image registration algorithm using improved chain-code representation combined with invariant moments. *IEEE Trans Geosci Remote Sens* 1999;37:2351–62. doi:10.1109/36.789634.
- [246] Zhao Y, Wang S, Zhang X, Yao H. Robust hashing for image authentication using zernike moments and local features. *IEEE Trans Inf Forensics Secur* 2013;8:55–63. doi:10.1109/TIFS.2012.2223680.
- [247] Zunic J, Rosin PL, Kopanja L. On the Orientability of Shapes. *IEEE Trans Image Process* 2006;15:3478–87. doi:10.4310/HHA.2011.v13.n2.a17.
- [248] Rosin PL, Žunić J. 2D Shape Measures for Computer Vision. *Handb Appl Algorithms Solving Sci Eng Pract Probl* 2007:347–71. doi:10.1002/9780470175668.ch12.
- [249] Peura M, Iivarinen J. Efficiency of simple shape descriptors. *Proc. Third Int. Work. Vis. Form*, 1997, p. 443–451.
- [250] Zhang D, Lu G. Review of shape representation and description techniques. *Pattern Recognit* 2004;37:1–19. doi:10.1016/j.patcog.2003.07.008.
- [251] Patel MN, Purvi Tandel. A Survey on Feature Extraction Techniques for Shape based Object Recognition. *Int J Comput Appl* 2016;137:16–20.
- [252] Kurnianggoro L, Wahyono, Jo KH. A survey of 2D shape representation: Methods, evaluations, and future research directions. *Neurocomputing* 2018;300:1–16. doi:10.1016/j.neucom.2018.02.093.
- [253] Hu M-K. Visual Pattern Recognition by Moment Invariants. *IRE Trans Inf Theory* 1962;8:179–87.

- [254] Chen CC. Improved moment invariants for shape discrimination. *Pattern Recognit* 1993;26:683–6. doi:10.1016/0031-3203(93)90121-C.
- [255] Tsai WH, Chou SL. Detection of generalized principal axes in rotationally symmetric shapes. *Pattern Recognit* 1991;24:95–104. doi:10.1016/0031-3203(91)90080-O.
- [256] Olden JD, Joy MK, Death RG. An accurate comparison of methods for quantifying variable importance in artificial neural networks using simulated data. *Ecol Modell* 2004;178:389–97. doi:10.1016/j.ecolmodel.2004.03.013.
- [257] Gevrey M, Dimopoulos I, Lek S. Review and comparison of methods to study the contribution of variables in artificial neural network models. *Ecol Modell* 2003;160:249–64. doi:10.1016/S0304-3800(02)00257-0.
- [258] Palik ED. *Handbook of optical constants of solids*. vol. 3. New York: Academic Press; 1998.
- [259] Rockstuhl C, Fahr S, Lederer F. Absorption enhancement in solar cells by localized plasmon polaritons. *J Appl Phys* 2008;104. doi:10.1063/1.3037239.
- [260] Vos MFJ, Macco B, Thissen NFW, Bol AA, Kessels WMME. Atomic layer deposition of molybdenum oxide from (NtBu)₂(NMe)₂Mo and O₂ plasma. *J Vac Sci Technol A* 2016;34:01A103.
- [261] Dennler G, Forberich K, Ameri T, Waldauf C, Denk P, Brabec CJ, et al. Design of efficient organic tandem cells: On the interplay between molecular absorption and layer sequence. *J Appl Phys* 2007;102. doi:10.1063/1.2825651.

APPENDIX A

SENSITIVITY ANALYSIS USING NEURAL NETWORKS

One of the useful by-products of a surrogate model is that it provides a way of analyzing sensitivity of objective function to different input variables, without having to run extensive first order computations. If a surrogate model exists that approximates the input-output map function of a system, the sensitivity of an output to each design parameter at a particular configuration can be more efficiently computed either through explicit derivatives of the surrogate function, or numerical gradient calculations of the approximate function. This approach has in particular been studied for NNs. Olden et al. [256] and Gevrey et al. [257] reviewed methods of input contribution to the output independently in ecological sciences. In [256], several sensitivity analysis methods are proposed such as Neural Interpretation Diagram (NID), Garson's algorithm and Sensitivity Analysis, and the authors proposed a randomization test for input-hidden-output connection weight selection. In [257], Partial Derivatives (PaD) method, Perturb method, Weights (Garson's Algorithm) method, Profile method (Sensitivity Analysis), Classic and Improved Stepwise methods were discussed. PaD and Profile methods provide information on the order of contribution and mode of action, while the other methods classify only the order of contribution. In the present study, we use these two methods and Garson's algorithm for comparison in order to investigate the effects of solar cell geometry and source properties on absorbed power by the active layer. These three methods are

explained below in detail. For other methods, we refer the interested reader to [256] and [257].

A.1. Partial Derivative (PaD) Method

In PaD, partial derivative of output with respect to each input for a set of data is calculated. This method provides information on the change in response based on minor changes in inputs. Partial derivative of n^{th} output in the data set q_n with respect to the input vector \mathbf{p}_n for an L -layer NN based on re-normalized (original) values is:

$$d_n = \frac{\partial \mathbf{q}_n}{\partial \mathbf{p}_n} = [\mathbf{W}_1]^T \mathbf{S}_1, \quad (\text{A.1})$$

$$S_i = \left(\frac{\mathbf{q}_{\max} - \mathbf{q}_{\min}}{2} \right)^{L-i+1} s_i.$$

where \mathbf{S}_i and \mathbf{s}_i are the Marquardt sensitivity values based on original and normalized output values evaluated in Equation (5), respectively. \mathbf{d}_n is calculated for a set of N_d points, which is not necessarily the complete training or validation sets.

The results of PaD method could be interpreted by calculating the mean sum of squared derivatives for each input and determination of the relative importance accordingly [257]. Mean sum of squared derivatives and percentage MSSD for j^{th} input are calculated as:

$$\text{MSSD}_j = \frac{1}{N_D} \sum_{n=1}^{N_D} d_n^2(j). \quad (\text{A.2})$$

$$\% \text{ PMSSD}_j = \frac{\text{MSSD}_j}{\sum_j^{R_0} \text{MSSD}_j} \times 100. \quad (\text{A.3})$$

A.2. Profile Method

The profile method is a straightforward yet effective method to determine input contribution to the output. The logic behind this method is to change the value of one input at a specified step in a specified range successively, while keeping the other inputs constant and record the response of NN. In the present study, the entire range of values is considered for each parameter, and the value of each parameter is changed with %10 increments from min to max value. The other parameters are kept at average of their min and max values. This method reduces to PaD if the step size is infinitesimal. The relationship between input and output is studied by Olden *et al.* [256] and classified into different categories such as Gaussian response curve, Bimodal response curve, flat response curve, etc.

A.3. Garson's Method

Garson's algorithm compares the relative contributions of inputs by calculating the weight values connecting each input to the output. The absolute values of the weights are considered, therefore the true effect of the input on the output cannot be determined.

Importance of the j^{th} input (I_j) and percent importance (PI) is calculated by:

$$I_j = \frac{\sum_{i=1}^{R_1} |W_1^{i,j} W_2^{1,j}|}{\sum_j^{R_0} |W_1^{i,j} W_2^{1,j}|} \quad (A.4)$$

$$\% PI_j = \frac{I_j}{\sum_j^{R_0} I_j} \times 100.$$

A.4. Sensitivity Analysis Results

The relative contribution of each input obtained by PaD method and Garson's algorithm can be seen in Both methods results are mostly agreeing. We can conclude that the least effective input is t_2 , and the most sensitivity is with respect to λ, θ, t_1, r .

Table A.1. Percentage relative contribution of inputs using PaD and Garson's Methods.

Input	% PMSSD (PaD)	Importance Row (PaD)	% PI (Garson)	Importance Row (Garson)
t_1	13.3	4	16.4	3
r	16.0	3	14.4	4
s	3.2	6	12.2	5
P	5.2	5	12.1	6
t_2	0.7	7	8.3	7
θ	29.2	2	20.7	2
λ	32.4	1	16.0	1

Figure A.1 shows input contributions obtained by the Profile method. The inverse relation of output to θ and the direct proportional relation to t_1 is evident there. The maximum output is observed around $\lambda \sim 480\text{nm}$ which is very close to the peak point of the extinction coefficient of P3HT:PCBM at 500 nm. Similar to the findings from the other methods, t_2 and s do not have a considerable contribution to the output. However, at certain r and P values with other parameters fixed, absorptivity is maximized.

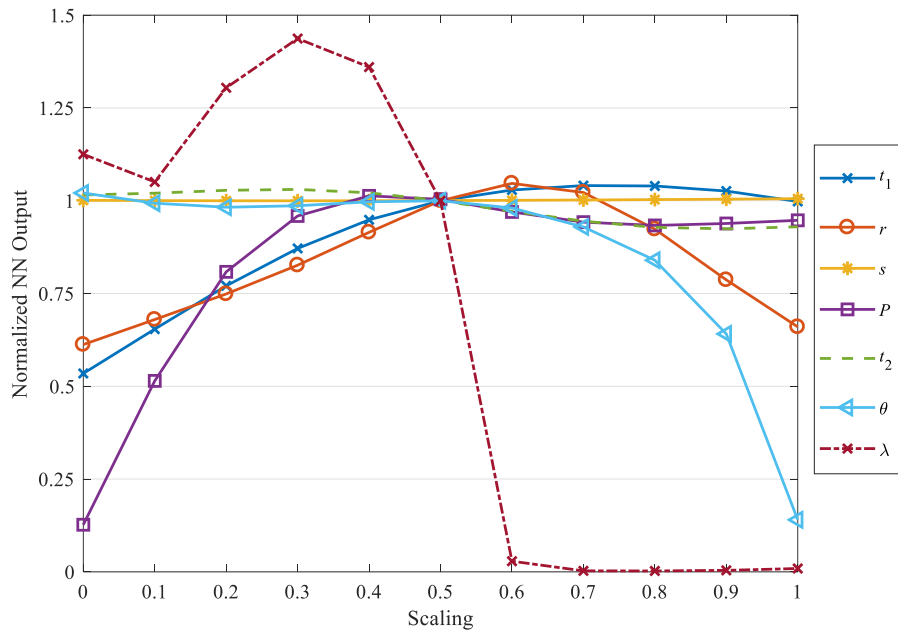
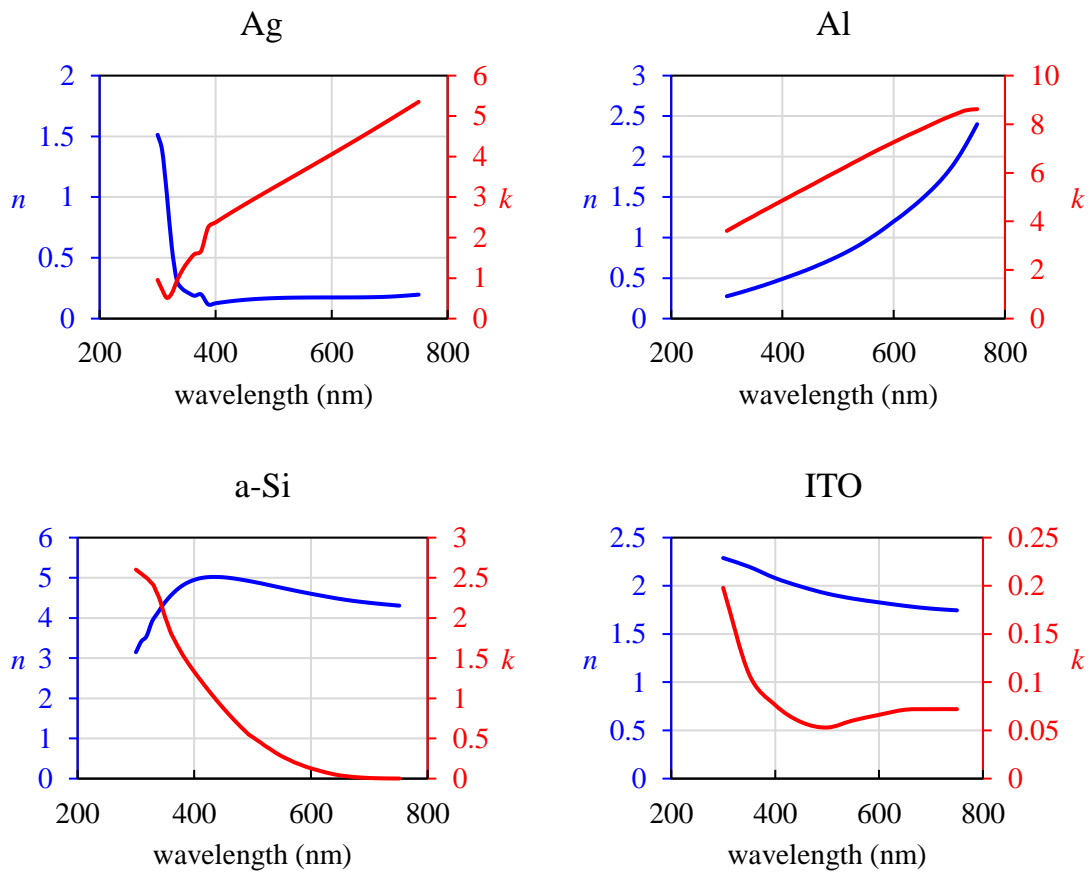


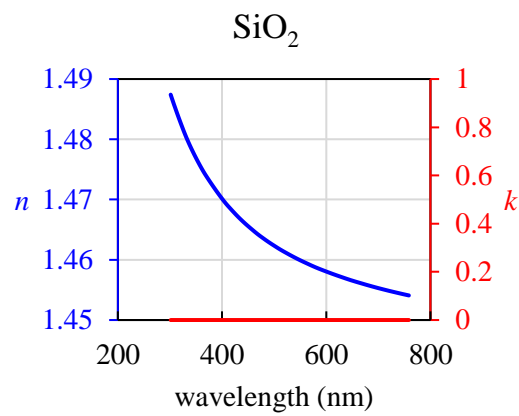
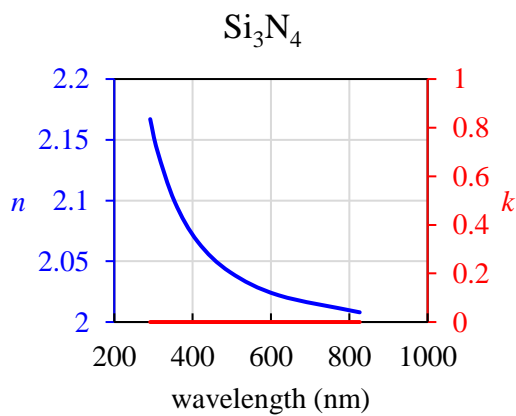
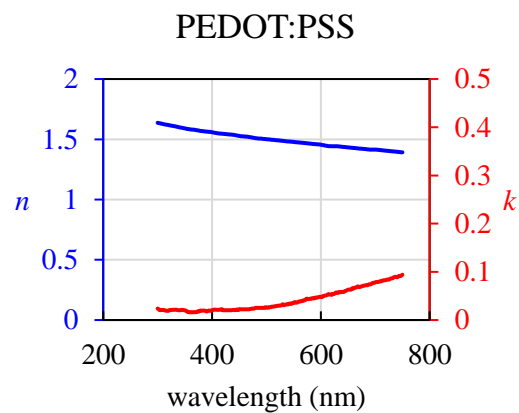
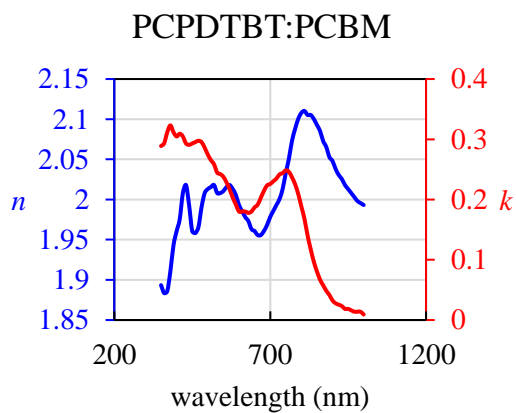
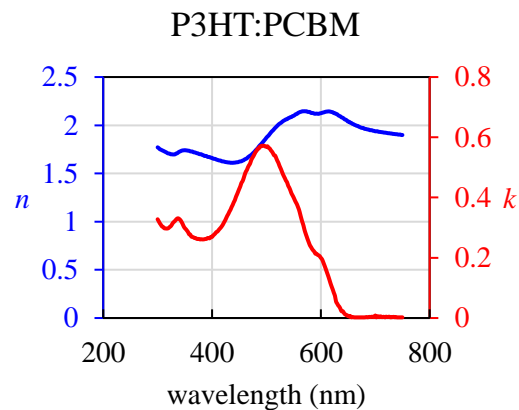
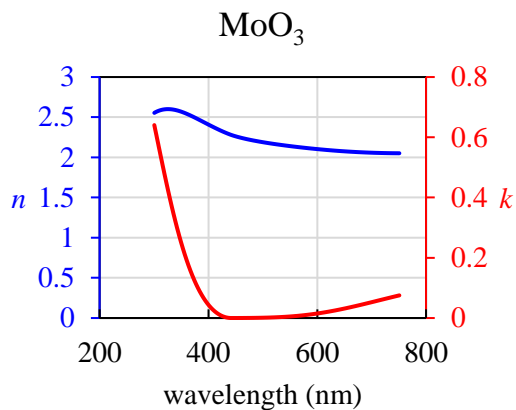
Figure A.1. Variation of NN Output with respect to inputs using Profile Method

APPENDIX B

OPTICAL PROPERTIES OF THE MATERIALS

The optical properties, i.e. refractive indices of the materials used in this dissertation are presented in this section. These properties are taken from literature [99,258–261].





ZnO

